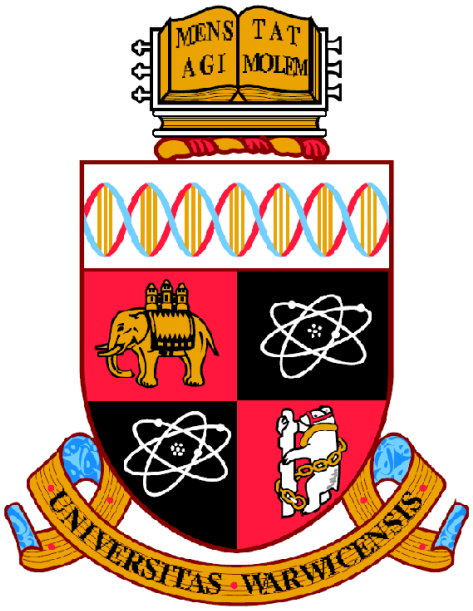

Quantitative electrochemical EPR

By

Mika Tamski

Thesis

Submitted to the University of Warwick

for the degree of

Doctor of Philosophy

Department of Physics

October 2015

THE UNIVERSITY OF WARWICK

Contents

List of figures

Acknowledgements

Always coming home…

Declaration and published work

I declare that the work presented in this thesis is my own except where stated otherwise, and was carried out at the University of Warwick, during the period of October 2011 and October 2015 under the supervision of Professor M. E. Newton. The research reported here has not been submitted, either wholly or in part, in this or any other academic institution for admission to a higher degree.

Some parts of the work reported and other work not reported in this thesis have been published, as listed below:

Published papers

M. A. Tamski, J. V. Macpherson, P. R. Unwin and M. E. Newton, *Physical chemistry chemical physics : PCCP*, 2015, **17**, 23438-23447.

Conference presentations

I. M. A. Tamski, J. V. Macpherson, P. R. Unwin and M. E. Newton, *Loop gap resonators in electrochemical electron paramagnetic resonance*, The 6th EFEPR Winter School on Advanced EPR Spectroscopy, Weizmann Institute of Science, Israel, poster presentation (2013)

II. M. A. Tamski, J. V. Macpherson, P. R. Unwin and M. E. Newton, *Electrochemical electron paramagnetic resonance utilising microelectrodes and loop gap resonators*, The 46th Annual International Meeting of the ESR Spectroscopy Group of the Royal Society of Chemistry, poster presentation (2013)

III. M. A. Tamski, J. V. Macpherson, P. R. Unwin and M. E. Newton, *Electrochemical electron paramagnetic resonance utilizing microelectrodes and loop gap resonators*, The 47th Annual International Meeting of the ESR Spectroscopy Group of the Royal Society of Chemistry, University of Dundee, oral presentation (2014)

Mika Tamski
October 2015

Abstract

Electron paramagnetic resonance (EPR) is a spectroscopic technique sensitive to unpaired electrons present in paramagnetic species such as free radicals and organometallic complexes.

Electrochemistry (EC) is an interfacial science, where reduction and oxidation processes are studied. A single electron reduction or oxidation generates a paramagnetic species with an unpaired electron, thus making EPR a valuable tool in the study of electrochemical systems.

In this work a novel electrochemical cell was designed and developed to be used with a specific type of EPR resonator, called loop gap resonator (LGR). After building and characterising the performance of the EC-EPR setup, it was adapted for quantitative measurements in electrochemical EPR (QEC-EPR).

Thus, for the first time, the technique of EC-EPR has been fully characterised for analytical work, opening possibilities to study electrode reactions quantitatively with accuracy and precision not obtained before, as demonstrated in Chapter 8 of this thesis.

Abbreviations and symbols

Abbreviations

AC	Alternating current
AQS	Anthraquinonesulfonate
BQ	Benzoquinone
CE	Counter electrode
CV	Cyclic voltammetry
CW	Continuous Wave
DC	Direct current
DI	Double integrated signal intensity of 1st derivative EPR spectrum
DMF	Dimethylformamide
DPPH	a,a'-diphenyl-β-picrylhydrazyl
EC	Electrochemistry
EPR	Electron paramagnetic resonance
EC-EPR	Electrochemical electron paramagnetic resonance
FcTMA	(Ferrocenylmethyl) trimethylammonium hexafluorophosphate
FWHH	Full width half height
HOMO	Highest occupied molecular orbital
HQ	Hydroquinone
LGR	Loop gap resonator
LOD	Limit of detection
LOQ	Limit of quantification
LUMO	Lowest unoccupied molecular orbital
MO	Molecular orbital
MV	Methyl viologen
MW	Microwave
NMR	Nuclear magnetic resonance
RE	Reference electrode
RMS	Root mean square
S:N	Signal to Noise ratio

SQ	Semiquinone
WE	Working electrode
TBAP	tetra-*N*-butylammonium perchlorate
TEMPAMINE	4-Amino-2,2,6,6-tetramethylpiperidino-1-oxyl
TEMPOL	4-hydroxy-2,2,6,6-tetramethylpiperidin-1-oxyl
TMPD	N,N,N', N'-tetramethyl-*para*-phenylenediamine
UMEA	Ultramicroelectrode array
VT	Variable temperature dewar

Symbols

a	Hyperfine splitting factor
A	Electrode surface area
A_p	Capacitor plate area
b	Band width of the entire detecting and amplifying system
C	Concentration
C_j	Concentration of species *j*
c	Resonator conversion factor
C_d	Capacitance of the double layer
c_r	constant from “one time” measurement of a reference standard
c_t	Filter time constant
C^*	Bulk concentration
d	Distance between capacitor plates
D	Diffusion coefficient
D_j	Diffusion coefficient of species *j*
D_O	Diffusion coefficient of oxidised form
ϵ	Dielectric constant
ε_r	Relative permittivity of material
E	Energy of an electron in an applied field
E_1	Electric field of MW irradiation
E	Electric potential applied to the electrode
E_{Appl}	Applied potential
E_{eff}	Effective potential
E_{Ohm}	Ohmic drop
E_λ	Switching potential
eV	Electron volt
ΔE	Energy difference of two spin states
ΔE	Magnitude of potential perturbation to WE
ΔE_p	Peak to peak separation
F_n	Noise factor for sources other than thermal
F	Faraday constant
g	*g*-factor of a free electron
g_{eff}	Effective g-factor of a given radical
G_R	a normalised receiver gain

h	Planck's constant
h	Width of an external magnetic field
ΔH_{pp}	peak to peak line width of a 1st derivative EPR line
H_0	External magnetic field
H_r	Effective magnetic field at resonance
H_{mod}	Modulation amplitude of H_0
H_1	magnetic field component of the microwave irradiation
H_I	Magnetic field introduced by a nucleus
i	Current
i_C	Capacitive current
i_F	Faradaic current
i_p	Peak current
i_p^{ox}	Anodic peak current
i_p^{red}	Cathodic peak current
iR	Ohmic drop
I	Nuclear quantum number
I_s	Steady state current at ultramicroelectrode
J_j	Flux of species *j*
j_p	Peak current density
k_B	Boltzmann constant
L	Orbital angular momentum
L	Inductance
m_e	Electron mass
m_s	Spin state of an electron, projection of μ_e in z-direction
n	population of an energy state
n	Number of electrons transferred in electrode reaction
n_B	Boltzmann factor for temperature dependence
n_S	number of scans
N_{min}	Minimum no. of spins detectable
N	Number of spins
N_V	Sample's spin volume density
$[O]_{bulk}$	Bulk concentration of oxidised form
$P_\uparrow$	Probability of upward transition
$P_\downarrow$	Probability of downward transition

P_0	Incident microwave power
q	Charge (in Coulombs)
Q	Quality factor of the resonator
Q_L	Loaded Quality factor of the resonator
Q_U	Effective unloaded Quality factor of the resonator
R	Universal gas constant
R_c	Compensated resistance
R_s	Solution resistance
R_u	Uncompensated resistance
R	Resonator radius
r_0	Radius of cylinder or disc electrode
S	Electron spin quantum number
S	Width of an experimental scan
ΔS_{pp}	peak to peak signal amplitude of a 1st derivative EPR line
t	scan time of an EPR spectrum
t	Time (in seconds)
$t_{1/2}$	Half-life of a radical
t_{mean}	Mean lifetime of radical
T	Temperature
T_1	Spin-lattice relaxation time
T_2	Spin-spin relaxation time
T_d	Detector temperature
T_s	Temperature of the sample
v	Frequency of the electromagnetic radiation in Hertz
v_{mod}	Modulation frequency
v_s	Potential Sweep Rate
v_{res}	Resonator frequency
v_{sol}	Velocity of volume element
Δv	Width of the resonator dip at half height
V	Signal voltage at the end of the transmission line
V_c	Volume of the cavity
V_r	Volume of the resonator
V_s	Volume of the sample
x	Direction of flux in Cartesian system in x-direction

Z	Resonator length
Z_0	Characteristic impedance of the transmission line
ς_j	Electric charge of the species *j*
$\boldsymbol{\Lambda}$	Resonator efficiency parameter
λ	Wavelength of electromagnetic radiation
η	Resonator filling factor
τ	spin lifetime
τ	Cell time constant
Γ	line width of the absorption line (half-width half-height)
μ_B	Bohr Magneton
μ_e	Magnetic moment of a free electron
μ_N	Nuclear Magnetic Moment
μ_0	Magnetic constant (permeability of vacuum)
γ_e	Gyromagnetic ratio of an isolated electron
δ	Diffusion layer thickness
χ^0	*Static magnetic susceptibility*
χ'	*In-phase* component of a dynamic magnetic susceptibility
χ''	*Out-of-Phase* component of the magnetic susceptibility
$\emptyset$	Electric potential
ω	Angular frequency
ε'	Real part of sample's dielectric constant
ε''	Imaginary part of the sample's dielectric constant

Chapter 1 – Electrochemistry

Electrochemistry is an old science originating from the work of scientists like Volta and Galvani, although the utilization of electrochemical phenomena has been traced back to Parthans (250 B.C.). Modern electrochemistry has develop into a science of interfaces and has recently been defined as: "*Electrochemistry is the study of structures and processes at the interface between an electronic conductor (the electrode) and the ionic conductor (the electrolyte) or at the interface between two electrolytes"*.[1]

1.1. The electrochemical interface

At the heart of an electrochemical (EC) experiment is the interface between the electrode and the sample solution, also called the electric double layer. Several reviews of the electric double layer have been published in recent years[2-4] despite the apparent maturity of the field. Below the structure and properties of the electrochemical interface are summarised, before moving on to issues related to mass transport and electrode properties, the main topics of this chapter.

1.1.1. Structure and dimensions

Although various types electrochemical interfaces exist, the most typical - and relevant to this thesis - is that between a metallic conductor (electrode) and a solution, the conductivity of which has been enhanced by addition of suitable supporting electrolyte

such as salt, acid or base (KCl, HCl, KOH etc.). The interface between the electrode and a solution acts as a capacitor (Figure 1.1a), where the charge at the metal surface is counter balanced by ions in the solution. In electrochemical experiments the potential of a working electrode (WE) and thus the energy of electrons at the metal surface is adjusted with respect to a reference electrode (RE). When a negative enough potential with respect to the species of interest (an analyte) is applied to the WE, an electro-reduction of the species occurs, and an electron is transferred to the lowest unoccupied molecular orbital (LUMO) (Figure 1.1b). On the other hand, for electro-oxidation, the potential of the WE can be adjusted to a value positive enough so that an electron is removed from the highest occupied molecular orbital (HOMO) of the analyte.[5]

The region across which the charge separation occurs is called *the electric double layer*, the structure, dimensions and thus the EC behaviour of which are strongly dependent on the system under study.[6] A schematic representation of the double layer is presented in Figure 1.2, where the net positive charge due to electron deficiency at the metal surface is confined to an extremely thin layer with a typical thickness of ca. 0.1 Å. At the solution side

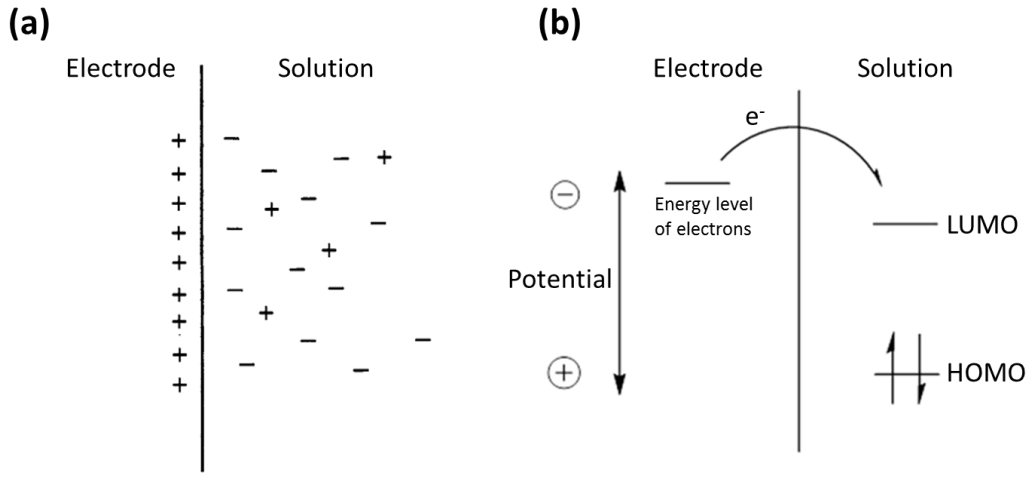

Figure 1.1. (a) the electrode-solution interface acting as a capacitor where the net positive charge at the electrode is matched by an equal negative charge in the solution. (b) In an electrochemical experiment the potential of the working electrode (WE), and thus the energy of the electrons at the electrode is manipulated with respect to a reference electrode (RE) to introduce reduction and oxidation reactions of species of interest. (Modified from ref. [7] pp. 4 and 12)

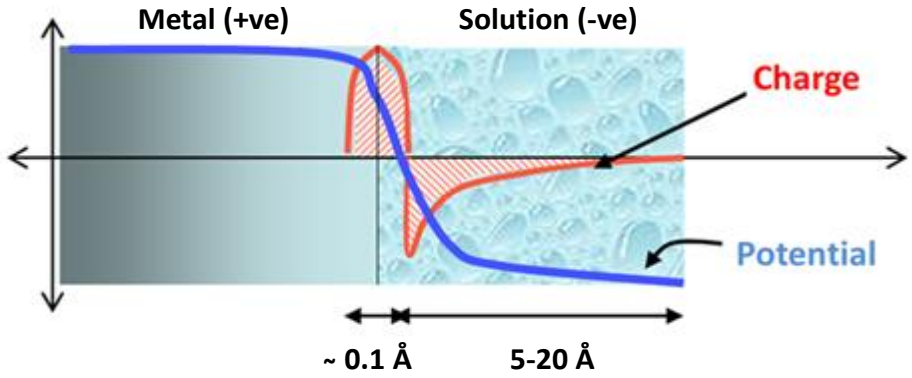

Figure 1.2. A schematic representation of the electric double layer. The net positive charge at the electrode surface is confined to a thin layer, whereas at the solution side the charge is smeared out to the solution, making the potential gradient across the double layer to be gradual. (Modified from ref. [1] pp. 5)

the equal negative charge is "smeared out" into the solution and thus the potential gradient across the double layer is more gradual than would be the case with a capacitor consisting of two parallel metal plates.

The effective dimensions of the double layer are extremely dependent on the system. For example the concentration and type of the supporting electrolyte affect the distance on the solution side across which the charge is balanced, ranging from tens of ångstroms in the case of 0.1 to 1.0 M solutions of strong electrolytes to ca. 100 Å in the case of diluted systems. None the less, as the voltage applied across the double layer is typically measured around 1 V, and the separation of the capacitor "plates" is extremely narrow, electric fields up to 10^9 V m^{-1} are realised making the capacitance of the double layer significant.[1, 7]

1.1.2. Properties

As mentioned above the electric double layer at WE/solution interface, to a good approximation, acts as a parallel plate capacitor, for which the capacitance can be defined as:[8]

$$C_d = \frac{\varepsilon_r A_p}{d}, \qquad (1.1)$$

where ε_r is the relative permittivity of the material between the plates (F m^{-1}) , A_p is the plate area (m^2) and d is the distance between the two plates. The behaviour of the capacitor can be expressed as:

$$\frac{q}{E} = C_d , \qquad (1.2)$$

where q is the charge stored in the capacitor in Coulombs (C), E is the potential applied across the capacitor plates in Volts (V) and C_d is the capacitance of the double layer in Farads (F). When a potential perturbation is applied to the electrode, a current must flow until the double layer has adjusted to match the new condition of q determined by C_d. It should be noted that the potential perturbation applied to the electrode introduces re-distribution of charged particles and solvent dipoles on the solution side, thus effectively changing the composition and geometry of the other "plate" of the capacitor, and therefore the capacitance of the electric double layer can be proportional to the applied potential, unlike in the case of normal capacitors.[7] As the potential of the WE is manipulated during an electrochemical experiment, the charging and discharging of the capacitor affects the observed signal in the following ways:

- The *RC* time constant

The magnitude of the charging current is dependent on the resistance of the system, and has a time component associated with it:

$$\tau = R_s C_d \,, \tag{1.3}$$

where τ is the time constant (in seconds) determining the time taken to charge the capacitor through the solution resistance R_s in Ohms (Ω). For a potential step the behaviour of the capacitive current (i_C) measured in amperes (A), can be expressed as:[9]

$$i_c = \frac{\Delta E}{R_s} exp\left(-\frac{t}{R_s C_d}\right) , \tag{1.4}$$

where ΔE is the magnitude of the potential perturbation and t is time (sec). As can be seen, the i_C decays exponentially over time and will distort the analytical Faradaic current (i_F), the recording of which is the aim of EC measurements based on manipulation of the potential. Therefore a minimum time interval of at least 5τ must be waited for a full establishment of the potential step, after which the electrochemical interface is charged to a point at which the desired potential gradient exists at the interface and analytical measurements can be performed.

Therefore to perform measurements on the shortest timescales possible, the τ should be minimised. This can be achieved by making the double layer capacitance as small as possible by minimising the surface area of the WE, and in the case of electrochemical cell design making sure that the cell geometry does not introduce unnecessary resistance to the measurements. Because of these requirements it turns out that each individual EC cell design has a characteristic time constant associated to it, which determines the shortest time scale at which analytical measurements can be performed accurately.[7]

- The Ohmic Drop (iR-drop)

When current (*i*) flows during an electrochemical experiment, the measured potential between WE and RE is distorted due to the Ohmic resistance (E_{Ohm}) of the solution:

$$E_{Ohm} = iR_s \,, \tag{1.5}$$

The E_{Ohm} term represents the difference between the applied potential (E_{appl}) and the effective one (E_{eff}) established across the electric double layer:[9]

$$E_{eff} = E_{appl} - E_{Ohm} \,, \tag{1.6}$$

Where all of the terms can have a time dependency, whether the potential is stepped to a constant value or swept linearly.

Large currents and solution resistance makes the E_{Ohm} more pronounced, and thus non-polar organic solvents tend to be prone to distorted potential control. Ways to minimise the effect are to minimise the current by making the WE as small as possible and decreasing the solution resistance by adding an excess of supporting electrolyte to the sample solution, which for organic solvents is often not possible due to lack of suitably soluble supporting electrolytes.[7] None the less, the significance of the R_s should not be ignored, as it contributes to both τ and E_{Ohm}.

Decreasing the size of the WE will not only lead to smaller Ohmic drop effect and better potential control as smaller currents are generated, but also reduce τ due to the smaller C_d. Therefore the electrochemical performance will improve through the miniaturization of the WE, a topic discussed further in Section 1.5.[10]

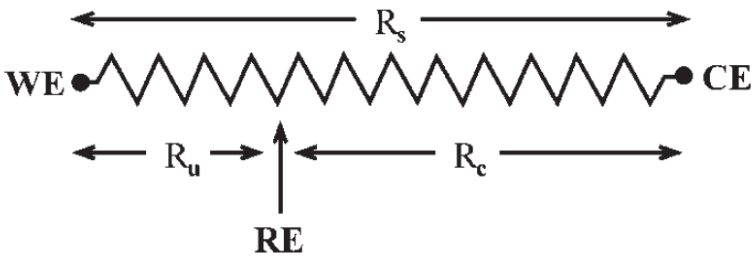

Figure 1.3. Three electrode arrangement for resistance compensation. (Modified from ref. [11] pp. 24)

1.2. The electrochemical setup

So far only a two electrode setup with WE and RE has been considered, which can be utilised as long as E_{Ohm} < 1-2 mV, for example in the case of R_s = 2 kΩ and i = 1 µA (E_{Ohm} = 2 mV). In systems where the E_{Ohm} due to i, R_s or the cell geometry become significant, a three electrode configuration can be employed by adding a counter electrode (CE) to the setup. In this case the current flows between the WE and CE, and the potential of the WE is controlled relative to the RE. By placing the RE as close to the WE as possible, the overall R_s can be divided into compensated resistance (R_c) and uncompensated resistance (R_u), thus minimising most of the potential drop (Figure 1.3).[11]

The extent to which a three electrode setup can minimise Ohmic drop depends completely on the application. For electrochemical EPR, several restrictions in terms of electrochemical cell geometry, placement of the electrodes and the choice of solvent exist, which affect the EC performance. For example, in the case of flat cell geometry the current path is limited to a small cross sectional area making the resistance significant. Furthermore, in a real EC-EPR cell (Figure 1.4a) the RE is often situated above the WE and the CE below it, making the Ohmic drop compensation insignificant.

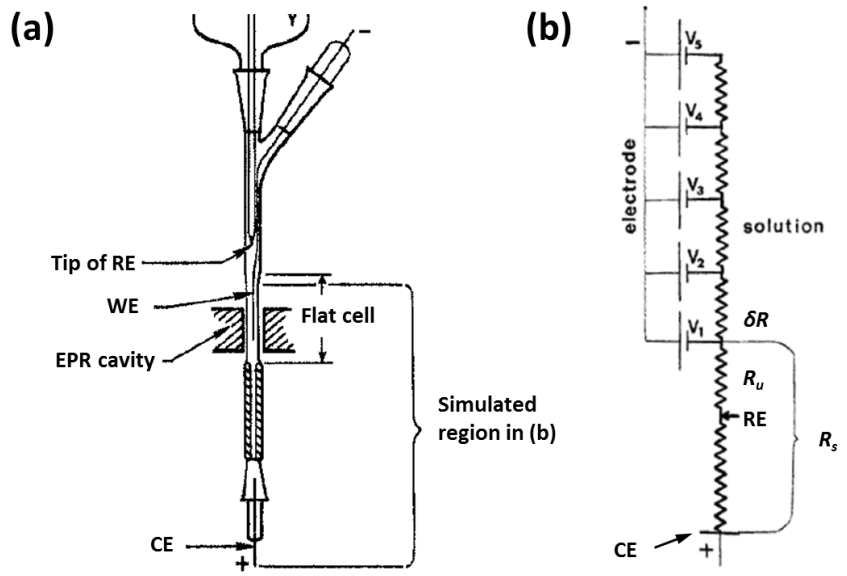

Figure 1.4. (a) EC-EPR cell based on flat cell design. (b) Simulation of the Ohmic drop effect along the WE surface Relative to CE. (Modified from ref. [12] pp. 2551)

Furthermore a second source for the Ohmic drop exists, as the potential across the WE surface varies depending on the distance from the CE (V_1 to V_5, Figure 1.4b) especially with organic solvents, and thus the current density along the WE is not uniform, as it drops in magnitude moving from segment to segment away from the CE by the amount determined by δR. Therefore, for large surface area electrodes inside a cell with a small cross section the placement of the RE close to the WE cannot remove all of the R_u, even if situated between the WE and CE as shown in Figure 1.4b.[12]

1.3. Electrochemical experiments

The most common EC techniques utilised with EPR are cyclic voltammetry (CV), potential steps and current steps, although square wave voltammetry[13] and other potential modulation techniques[14] also have been employed.[15]

1.3.1. Step methods

In potential step method (chronoamperometry) the potential of the WE is stepped from an initial value (E_1) where Faradaic processes do not occur to a final potential (E_2), where reduction (or oxidation) of the species of interest does take place (Figure 1.5a). The corresponding current response is shown in Figure 1.5b for stationary solution, where diffusion is the only active method of mass transport. After applying the potential E_2, the electrolysis current decays rapidly from the initial high value, as the electroactive species is depleted from the electrode surface and a relatively slow process of diffusion starts to transport analyte to the electrode from the bulk solution.[5, 16]

The Cottrell equation predicts the current behaviour as a function of time in stationary solutions, where the only mechanism of mass transport is diffusion:

$$i = \frac{nFAD_O{}^{1/2}[O]_{bulk}}{\pi^{1/2}t^{1/2}}, \qquad (1.7)$$

where n is the number of electrons transferred, F is Faraday's constant, A is the surface area of the electrode (cm^2) , D_O is the diffusion coefficient of the electroactive species ($cm^2\ s^{-1}$) , $[O]_{bulk}$ is the bulk concentration of the electroactive species (mol cm^{-3}) and t is time (sec).

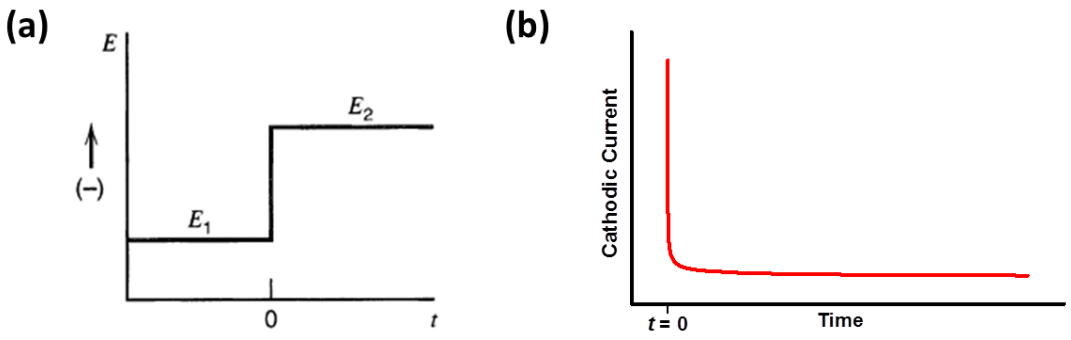

Figure 1.5. A potential step experiment for a reduction of electroactive species. (a) The potential of the WE is stepped instantaneously from E_1 where no Faradaic current is generated to a value E_2 where the analyte is reduced. (b) A current behaviour for a potential step experiment in stationary solution. (Modified from ref. [7] pp. 157)

In EC-EPR, potential steps have been used mainly in electrolysis to generate the desired amount of paramagnetic species for EPR investigation, either to study the EPR spectrum of the species, or to monitor the EPR signal amplitude as a function of potential and time.[17-19]

Instead of a potential step, a constant current pulse can be applied, where the WE is set to deliver a desired current for a specific period of time. In comparison to potential step, this method allows a better control over the amount of radical species generated for EPR detection, although decomposition of the solvent can occur if the current pulse is too long, especially in systems where the Ohmic drop effect is significant.[20-23]

1.3.2. Cyclic voltammetry

In a cyclic voltammetry (CV) experiment, the potential of the WE is swept linearly from an initial value to a switching potential (E_λ), where the direction of the sweep is reversed and scanned back to the original value, as shown in Figure 1.6a. In Figure 1.6b a cathodic current starts to flow as the potential at the WE reaches a negative enough value for the reduction to occur. The current increases initially as the electron transfer rate gets faster with more negative potentials, until a peak value is obtained (i_p^{red}), as the diffusion is

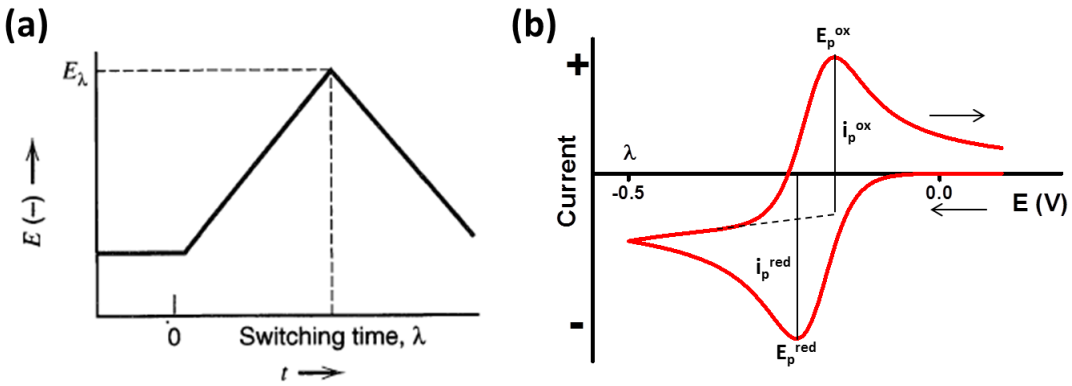

Figure 1.6. A cyclic voltammetry (CV) experiment for reduction of electroactive species. (a) The potential of the WE is swept from an initial value where no Faradaic current is generated to a value E_λ, where the sweep direction is reversed and potential then scanned back to the original value. (b) A current behaviour for a CV experiment in stationary solution Modified ref. [7] pp. 227)

unable to supply the WE with fresh analyte at a fast enough rate. During the return sweep an oxidative peak (i_p^{ox}) is observed, as the analyte reduced during the first scan is oxidized back to its original form.[5] A voltammetric experiments can also be conducted as a linear sweep, where only the first potential sweep is applied to the electrode, and thus only the first current peak recorded.

For large planar electrodes the peak current of the forward scan can be predicted:

$$i_p = 0.4663^{3/2} A F {D_O}^{1/2} {v_s}^{1/2} [O]_{bulk} \left(\frac{F}{RT}\right)^{1/2}, \qquad (1.8)$$

where v_s is the potential sweep rate (V s^{-1}), *R* is the universal gas constant (J mol^{-1} K^{-1}) and *T* is temperature in Kelvins (K).

In EC the shape and location of the voltammogram on the X-axis can be used to obtain kinetic and thermodynamic data of the system under study, which in the case of EC-EPR can then be related to radical generation efficiencies and kinetics of the radical decay.[21, 24, 25]

1.4. Mass transport

Central to evaluating an EC-EPR cell design and relating the EPR signal behaviour against processes taking place at the WE surface is the understanding of mass transport phenomena occurring in electrochemical systems. The electrochemical interface is dynamic by its very nature, distinguishing it from solid state EPR experiments where the EPR signal intensity does not change over time due to redistribution of the paramagnetic centres within the resonator. Below the modes of mass transport are considered, allowing a better understanding of the EC-EPR technique and challenges towards absolute quantification in Chapters 3 and 4.

1.4.1. Modes of mass transport

Mass transport mechanisms in EC can be divided into diffusion, migration and convection according to the Nernst-Planck equation, which for a flux in one direction (x) can be described as:[11]

$$J_j(x) = -D_j \frac{\partial C_j(x)}{\partial x} - \frac{z_j F}{RT} D_j C_j \frac{\partial \phi(x)}{\partial x} + C_j v_{sol}(x) \,, \qquad (1.9)$$

where J_j is flux of species j (mol cm^{-2} sec^{-1}) at distance x from the electrode surface, D_j (cm^2 sec^{-1}), z_j and C_j (mol cm^{-3}) are the diffusion coefficient, charge and concentration of species *j*, respectively; $v_{sol}(x)$ (cm sec^{-1}) is the rate at which a volume element moves in a solution; $\partial C_j(x)/\partial x$ is the concentration gradient and $\partial \phi(x)/\partial x$ is the electric field gradient along the x-axis.

- Convection

The third term on the right hand side of Equation 1.9 represents the effects of convection. In EC two types of convection are usually considered. The first type is called *natural convection* due to thermal and density gradients that exist within the sample solution. Natural convection is more typical for macro sized electrodes (mm or more) for experiments lasting 10-20 sec and more, where the diffusion field starts to collapse introducing local convective fluxes that are hard to predict or simulate, making analytical work impossible.

The natural convection can be avoided by introducing a deliberate *forced convection* to the EC system, for example by pumping the solution through a channel containing the WE, or utilising a rotating disc electrode. The effect of forced convection swamps any contribution

through natural convection, allowing the extension of time-scales beyond 10-20 sec. As long as the hydrodynamic conditions are well defined, it is possible to predict the mass transport pattern to the electrode surface quantitatively, thus facilitating analytical work.[5] As will be discussed in Chapter 3, many EC-EPR cell designs are based on flat cell design, where natural convection manifests, and thus setups based on forced convection have been successfully utilised in the study of paramagnetic reaction products.

- Migration

The second term on the right hand side of Equation 1.9 represents the effects of migration. The $\partial\phi/\partial x$ existing at the WE/solution interface will have an electrostatic effect, repulsive or attractive, to charged species present at the interfacial region, thus introducing a migratory flux to electrochemical systems. For example, during electrolysis, the concentration of charged species will change at the electrode surface, affecting the ionic strength at the interface, and thus the strength of $\partial\phi/\partial x$. Therefore, as the electrolysis proceeds, the migrational flux and hence the overall mass transport conditions will change over time, making the system difficult to interpret and quantify.

To avoid migration effects is another reason to add a chemically inert background electrolyte to the solution. When in large enough excess (typically 100 times relative to the reactants), the complications due to migration can be avoided, as charge neutrality at the electrode surface can be assumed and $\partial\phi/\partial x$ will not change as the electrolysis proceeds. As discussed above, the addition of background electrolyte also makes the solution electrically more conducting diminishing the Ohmic drop effect, ensuring that the current flowing through the cell during electrolysis is not limited by the conductivity of the bulk solution, but by the nature of the processes at the interfacial region.[5]

- Diffusion

The first term in Equation 1.9 represents Fick's first law of diffusion, relating flux of species *j* to its concentration gradient (how concentration varies over distance x) at a specific time *t*. The second law relates the change in the concentration of species *j* over time at a given point:[11]

$$\frac{\partial C_j}{\partial t} = D_j \left(\frac{\partial^2 C_j}{\partial x^2} \right), \tag{1.10}$$

Often the aim of the EC experiment is to make the diffusion the only means of mass transport. This can be achieved by setting the experiment such that the effects from convection and migration are negligible by using quiescent solutions, where stirring of the solution does not occur and adding supporting electrolyte to avoid the migration as explained above. This greatly simplifies the equation for mass transport (Eq. 1.9), making the analysis and interpretation of the EC data more feasible.

For simple electrode reactions involving only an electron transfer between the WE and the species of interest, the Nernst-Planck equation can be used to relate the E_{appl} to the relative concentrations of oxidized [*Ox*] and reduced [*Red*] species, assuming a reversible system with fast kinetics so that [*Ox*] and [*Red*] are at equilibrium at the electrode surface:[11]

$$E_{appl} = E^0 + \frac{RT}{nF} ln \frac{[Ox]}{[Red]}, \tag{1.11}$$

where E^0 is the standard potential. It is assumed that the concentrations of species in Equation 1.11 equal their activities.

Figure 1.7a shows the concentration profile of oxidized species as a function of applied potential at the WE surface for elementary reduction process according to the Nernst-Planck equation:

$$O + e^- \rightleftharpoons R\,, \tag{1.12}$$

where the standard potential for the reduction is -0.2 V. Applying a potential of -0.4 V, for example, will take the concentration of oxidized species [*Ox*] to zero at the WE surface, introducing a concentration gradient between the surface and the bulk of the solution, a mechanism that establishes the diffusion of more oxidized species towards the electrode. Whether the potential is swept or stepped to -0.4 V, the concentration gradient will develop over time getting shallower between the WE surface and the bulk solution $[Ox]_{bulk}$ as time proceeds and the diffusion layer grows thicker, as shown in Figure 1.7b, where x is the distance from the WE surface. The diffusion layer thickness for linear diffusion can be estimated from:[26]

$$\delta = (\pi D t)^{1/2}\,, \tag{1.13}$$

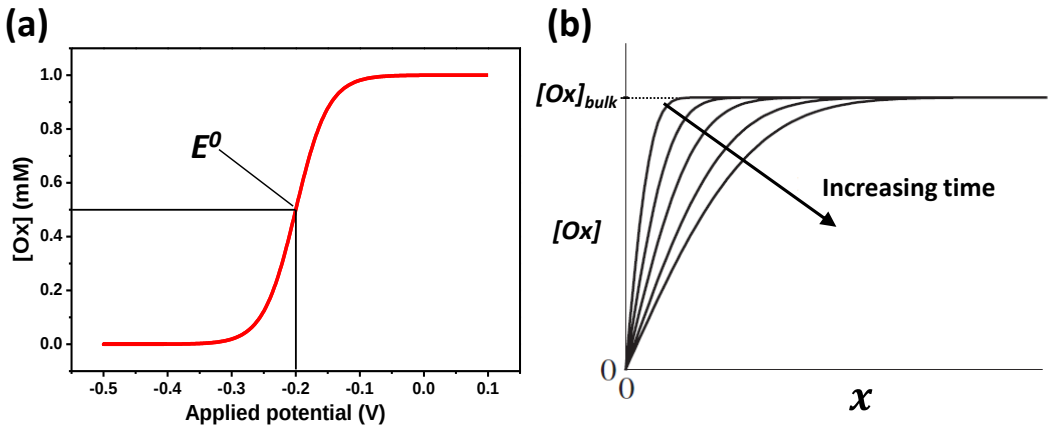

Figure 1.7. (a) a concentration profile for [Ox] of the electroanalyte at the WE surface as a function of electrode potential according to the Nernst-Planck equation. (b) The growth of the diffusion field and shallowing of the concentration gradient from the WE surface as a function of time for potential where the [Ox] goes to zero. (Modified from ref. [16] pp. 432)

showing a square root relationship of the diffusion layer thickness with *t*.

The size of the WE and its geometry will determine the shape of the diffusion field and thus the magnitude of the diffusive flux to the electrode surface. For example, for a large disk shaped electrode the diffusive flux is essentially normal or "axial" to the WE surface (Figure 1.8a), whereas for a very small disc (Figure 1.8b) there is a significant radial component to the diffusion. This results in much increased flux of analyte per unit surface area, giving small electrodes distinct advantages relative to large electrodes.

1.5. Ultramicroelectrodes (UMEs)

Depending on the geometry of the electrode, the characteristic dimension of a UME should be around 20 µm at maximum. The benefits of UMEs are:[27]

I. Small currents are produced, as the electrode is small in size, reducing the Ohmic-drop as discussed above.

II. The small size of the capacitance and application of smaller over potentials also decrease the cell time constant. This makes it possible to perform experiments on a time scale much shorter than with macro electrodes and allows fast-scan

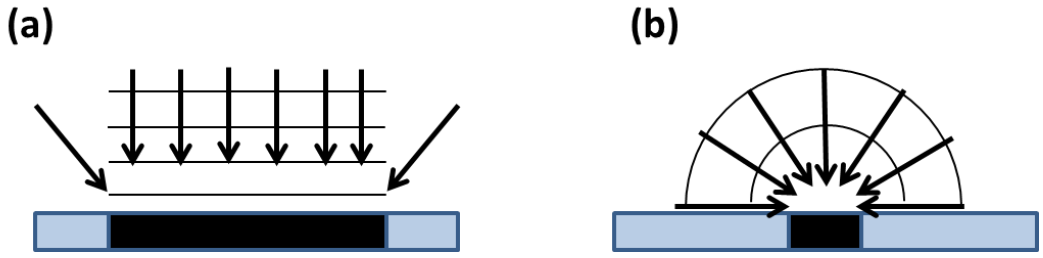

Figure 1.8. (a) A diffusion profile for a macro size disc electrode, where the diffusive flux is essentially normal or "axial" to the WE surface with negligible radial component. (b) A diffusion profile for a micro size disc, where a significant radial component to the diffusion greatly enhances the flux of analyte to the WE surface. (Modified from ref. [26] pp. 93)

voltammetry.

III. The rate of diffusive flux to the electrode increases significantly, and a steady state concentration of analyte at the electrode surface establishes quickly. The larger flux of analyte also diminishes the effect of natural convection.

The greatly enhanced mass transport results in high charge densities at the electrode, producing large Faradaic currents compared to the capacitance and thus high S/N. The benefits above have enabled electrochemistry to be applied in solid[28] and gas phase[29], as well as with non-polar organic solvents without a supporting electrolyte.[30]

The increased rate of mass transport is caused by the change of the shape of the diffusion field in the timescale of the experiment.[31-33] If the electrode is small enough and of correct shape, a radial component of the diffusion starts to have a significant effect and the flux of analyte to the electrode surface is increased. In steady state the rate of reaction is dependent on electrode kinetics rather than diffusion of the analyte to the electrode surface, enabling the study of electrode kinetics independently from mass transport. The exact current response during an experiment is dependent on the geometry of the electrode via the shape of the diffusion field.[34]

1.5.1. Geometry

Probably the most common shape of a UME is a disc surrounded by an insulating material such as glass. A similar geometry is that of a ring, which can be combined with a disc or rings with different diameter for various applications (Figure 1.9a). Other typical geometries include those of a cylindrical and a hemispherical, as shown in Figure 1.9b top and bottom, respectively, and that of a band (Figure 1.9c left). Each of the geometries have their benefits in terms of easiness of manufacture, the shape of the diffusion field,

homogeneity of the current density across the electrode surface etc. For true steady state to develop, the electrode geometry must have a convergence factor above 0.5, which is achieved when the electrode is finite in two dimensions as in the case of a sphere. The shapes of cylinder and band will not satisfy this requirement being infinite in one dimension, whereas disc and ring shapes for example can obtain a steady state under semi-infinite diffusion conditions, as the dimensions are finite provided that the electrode is small enough.[32]

Although the very small currents are favourable for electrochemistry, the analytical signal measured can be of the order of pA or nA, depending on the actual size of the electrode. To amplify the analytical current, several UMEs can be assembled into an array (UMEA) as shown for band geometry in Figure 1.9c on the right hand side, which enables the amplification of the measured signal.[35] This increase in the signal is exploited for example in biosensors[36,37], where UMEAs can offer a cheap, fast and reliable method of pesticide and toxicity testing.[38,39]

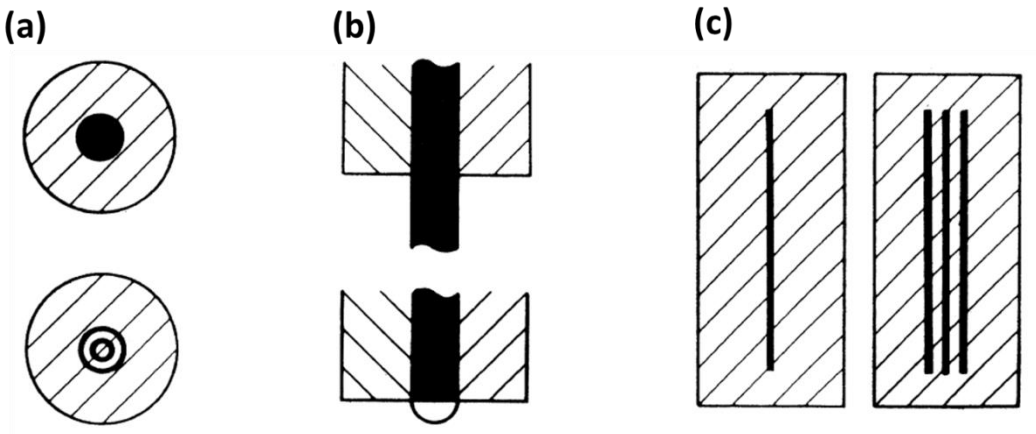

Figure 1.9. Different UME geometries. (a) disc (top) and ring (bottom). (b) cylinder (top) and hemisphere (bottom). (c) band (left) and band array (right). (Modified from ref. [34] pp. 415)

1.5.2. Wire electrodes

The electrode geometry relevant to the work in this thesis is the cylindrical one, for which the Fick's second law of diffusion, assuming no end effects, can be written as:[9]

$$\frac{\partial C}{\partial t} = D\left(\frac{\partial^2 C}{\partial r^2} + \frac{1}{r}\frac{\partial C}{\partial r}\right), \tag{1.14}$$

As seen from equation 1.14, assuming symmetry along the length of the electrode (z-direction), the diffusion is dependent only on a single dimension (*r*) in an xy-plane, and therefore simple to solve mathematically.

Of a cylindrical geometry, metal wire acting as an electrode is one of the simplest and easiest to manufacture, and the critical dimension characterising the time dependent behaviour is the radius of the cylinder. Figure 1.10 shows a schematic of a cylindrical wire electrode, where an axis of symmetry dominates the geometry along the length of the wire in z-direction, prepared by removing insulation from around a central conductor. Also shown is the development of the diffusion layer thickness as a function of time, growing concentrically around the electrode. Over time, the curvature of the diffusion layer becomes shallower when compared to the curvature at the electrode surface, giving rise to a radial component to the diffusion, and thus an enhanced flux of analyte to the electrode surface. None the less, as shown below, it is not possible to obtain true steady state behaviour at cylindrical electrodes, no matter how small the radius of the electrode is.[40, 41]

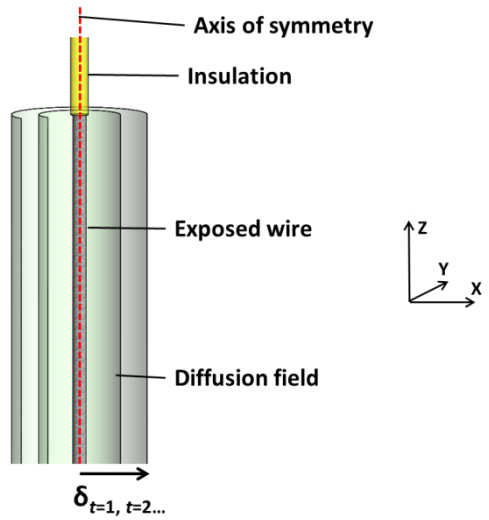

Figure 1.10. Cylindrical geometry with axial symmetry along z-direction making the diffusion dependent only on one dimension (*r*). The diffusion field grows concentrically around the electrode introducing a radial component to the diffusion and increasing the flux of analyte to the electrode surface from that expected for a planar electrode of similar surface area

The theory for the diffusion of electro active species to a thin cylindrical electrode has been developed for potential step[42, 43] and linear sweep experiments.[40] Provided that the length of the cylinder is large compared to the radius, the current during a potential step is:

$$i = \frac{nFAD_oC^*}{r_0}\left[\frac{2exp\left(-0.05\pi^{1/2}\theta^{1/2}\right)}{\pi^{1/2}\theta^{1/2}} + \frac{1}{ln\left(5.2945+0.7493\theta^{1/2}\right)}\right], \quad (1.15)$$

with $\theta = 4D_ot/r_0^2$ where r_o is the radius of the cylinder, *A* the surface area of the electrode and C^* is the bulk concentration (mol cm^3). For short timescales θ is small the current is essentially Cottrellian, as the first term in the parentheses (Equation 1.15) dominates. The diffusion remains Cottrellian within 4 % until the diffusion field has become ca. 10 % of r_o, deviating only after the diffusion length becomes large relative to the curvature of the electrode surface. At this point the radial component of the diffusion causes the current to increase from that expected for planar macro electrode, as the second term in the parentheses becomes dominant. Because the current is dependent of time (through θ), no

true steady state is ever reached. None the less, as the time manifests only as an inverse logarithmic function for long time scales, a *quasi-steady state* is achievable.[7]

For a linear sweep the empirically obtained peak current density is:

$$j_p = \frac{n^2F^2C^*r_0v_s}{RT}\left(\frac{0.446}{p} + \frac{0.335}{p^{1.85}}\right), \qquad (1.16)$$

Where v_s is the scan rate. The value of *p* characterises the voltammogram, representing the ratio of the potential scan rate (*nF/RT*)av to the diffusion rate *D/a*, defined as:

$$p = \sqrt{nFr_0{}^2v_s/TRD}\,, \qquad (1.17)$$

For high scan rates or large electrode diameters the values of *p* are also large, and the behaviour is similar with linear sweep voltammograms at a large planar electrode, whereas for very slow scan rates and small electrode diameters the *p* is small and the behaviour approaches the steady state solution given by equation $I_s = 4nFC^*Dr_0$ for a UME disc.[44]

None the less, the possibility of adjusting the length of the cylinder allows the utilisation of currents typical to macro electrodes with some of the benefits of UMEs through radial diffusion, which will be beneficial in electrochemical EPR, as discussed later.

References

1. E. S. Wolfgang Schmickler, *Interfacial Electrochemistry* Springer, Heidelberg, London, Germany, 2010.
2. E. Gileadi, *J. Solid State Electrochem.*, 2011, **15**, 1359-1371.
3. B. B. Damaskin and O. A. Petrii, *J. Solid State Electrochem.*, 2011, **15**, 1317-1334.
4. W. R. Fawcett, *J. Solid State Electrochem.*, 2011, **15**, 1347-1358.
5. A. C. Fisher, *Electrode Dynamics*, Oxford University Press, Oxford, 1996.
6. R. Greef, R. Peat, L. M. Peter, D. Pletcher and J. Robinson, *Instrumental Methods in Electrochemistry* Ellis Horwood, Chichester, 1985.
7. A. J. Bard and L. R. Faulkner, *Electrochemical Methods: Fundamentals and Applications*, 2nd edn., JOHN WILEY & SONS, INC., 2001.
8. B. I. Bleaney and B. Bleaney, *Electricity and Magnetism*, 3rd edn., Oxford University Press, London, 1976.
9. J. Heinze, *Angew. Chem. Int. Edit. Engl.*, 1993, **32**, 1268-1288.
10. J. O. Howell and R. M. Wightman, *Anal. Chem.*, 1984, **56**, 524-529.
11. M. Ciobanu, J. P. Wilburn, M. L. Krim and D. E. Cliffel, in *Handbook of Electrochemistry*, ed. C. G. Zoski, Elsevier, Oxford, UK, 2007, pp. 3-29.
12. I. B. Goldberg, A. J. Bard and S. W. Feldberg, *J. Phys.Chem.*, 1972, **76**, 2550-2559.
13. R. D. Allendoerfer, G. A. Martinchek and S. Bruckenstein, *Anal.Chem.*, 1975, **47**, 890-894.
14. L. Zhuang and J. T. Lu, *J. Electroanal. Chem.*, 1997, **429**, 115-120.
15. R. N. Bagchi, A. M. Bond and F. Scholz, *Electroanal.*, 1989, **1**, 1-11.
16. G. Denuault, M. Sosna and K.-J. Williams, in *Handbook of Electrochemistry*, ed. C. G. Zoski, Elsevier, Amsterdam, Netherlands, 2007, pp. 431-469.
17. R. N. Bagchi, A. M. Bond, F. Scholz and R. Stosser, *J. Electroanal. Chem.*, 1988, **245**, 105-112.
18. D. A. Fiedler, M. Koppenol and A. M. Bond, *J. Electrochem. Soc.*, 1995, **142**, 862-867.
19. J. G. Gaudiello, P. K. Ghosh and A. J. Bard, *J. Am. Chem. Soc.*, 1985, **107**, 3027-3032.
20. R. G. Compton, P. J. Daly, P. R. Unwin and A. M. Waller, *J. Electroanal. Chem.*, 1985, **191**, 15-29.
21. I. B. Goldberg and A. J. Bard, *J. Phys. Chem.*, 1971, **75**, 3281-3290.
22. I. B. Goldberg and A. J. Bard, *J. Phys. Chem.*, 1974, **78**, 290-294.
23. I. B. Goldberg, D. Boyd, R. Hirasawa and A. J. Bard, *J. Phys. Chem.*, 1974, **78**, 295-299.
24. W. J. Albery, R. G. Compton and C. C. Jones, *J. Am. Chem. Soc.*, 1984, **106**, 469-473.
25. L. Zhuang and J. Lu, *Rev. Sci. Instrum.*, 2000, **71**, 4242-4248.
26. C. M. A. Brett and A. M. O. Brett, *Electrochemistry: Principles, Methods and Applications*, Oxford University Press, Oxford, UK, 1993.
27. S. Pons and M. Fleischmann, *Anal. Chem.*, 1987, **59**, A1391-A1399.
28. A. M. Bond, M. Fleischmann and J. Robinson, *J. Electroanal. Chem. Interfacial Electrochem.*, 1984, **180**, 257-263.

29. J. Ghoroghchian, F. Sarfarazi, T. Dibble, J. Cassidy, J. J. Smith, A. Russell, G. Dunmore, M. Fleischmann and S. Pons, *Anal. Chem.*, 1986, **58**, 2278-2282.
30. A. M. Bond and T. F. Mann, *Electrochim. Acta*, 1987, **32**, 863-870.
31. M. Fleischmann and S. Pons, *J. Electroanal. Chem.*, 1987, **222**, 107-115.
32. A. M. Bond, K. B. Oldham and C. G. Zoski, *Anal. Chim. Acta*, 1989, **216**, 177-230.
33. C. G. Zoski, *J. Electroanal. Chem.*, 1990, **296**, 317-333.
34. R. M. Wightman, *Science*, 1988, **240**, 415-420.
35. J. Orozco, C. Fernandez-Sanchez and C. Jimenez-Jorquera, *Sensors*, **10**, 475-490.
36. G. A. Evtugyn, H. C. Budnikov and E. B. Nikolskaya, *Talanta*, 1998, **46**, 465-484.
37. M. J. Dennison and A. P. F. Turner, *Biotechnol. Adv.*, 1995, **13**, 1-12.
38. D. M. Yong, C. Liu, D. B. Yu and S. J. Dong, *Talanta*, 2011, **84**, 7-12.
39. C. Liu, T. Sun, X. Xu and S. Dong, *Anal. Chim. Acta*, 2009, **641**, 59-63.
40. K. Aoki, K. Honda, K. Tokuda and H. Matsuda, *J. Electroanal. Chem.*, 1985, **182**, 267-279.
41. K. Aoki, K. Tokuda and H. Matsuda, *J. Electroanal. Chem.*, 1986, **206**, 47-56.
42. K. Aoki, K. Honda, K. Tokuda and H. Matsuda, *J. Electroanal. Chem.*, 1985, **186**, 79-86.
43. A. Szabo, D. K. Cope, D. E. Tallman, P. M. Kovach and R. M. Wightman, *J. Electroanal. Chem.*, 1987, **217**, 417-423.
44. K. Aoki, *Electroanal.*, 1993, **5**, 627-639.

Chapter 2 - Electron paramagnetic resonance

2.1. Uses of EPR

Electron paramagnetic resonance (EPR) as a technique is sensitive to paramagnetic species with unpaired electrons only (radical, bi-radical, triplet etc.), and thus provides specific information on the paramagnetic centre and its environment. Uses of EPR range from the detection and characterisation of small organic and inorganic radicals in liquids and solids to organometallic complexes and molecule-based magnetic materials.[1]

Industrially significant applications of EPR range from polymer formation and degradation studies[2-4] to the food industry, where sterilization through irradiation can be used to increase hygiene and extend shelf life,[5-8] or to measure antioxidant properties of different foodstuffs.[9-11] Other uses of EPR are found from fields such as biology and medicine[12, 13], catalysis[14-17] and semiconductor applications.[18-21]

Below the fundamental theory of continuous wave (CW) EPR is discussed in terms of phenomena that allow and facilitate the recording of the EPR spectrum.

2.2. The Zeeman effect

A quantum particle such as an electron has an intrinsic *spin angular momentum*, which is a vector property having a magnitude and direction. This angular momentum is indicated by a spin quantum number *S* and in case of an electron has a value of ½. The electron *spin angular momentum* is associated with a magnetic moment μ_e which for a free electron can be presented as:[22]

$$\boldsymbol{\mu_e} = -g\,\mu_B\,\boldsymbol{S}\,, \tag{2.1}$$

where *g* is the *g*-factor discussed in a section below with a value of 2.002319 in a vacuum, μ_B is the Bohr magneton, a natural unit of an electron's magnetic moment given by $\mu_B = -|e|h/4\pi m_e = -9.27410^{-24}$ J T^{-1}, where *e* is the electron charge, *h* is the Planck constant (6.626×10^{-34} Js) and m_e is electron mass.

When an external magnetic field (H_0 or B_0) is applied to an electron spin, the energy is given as a scalar product between μ_e and H_0:

$$E = -\boldsymbol{\mu_e}\cdot\boldsymbol{H_0} = g|\mu_B|\boldsymbol{S}\cdot\boldsymbol{H_0}\,, \tag{2.2}$$

which assuming that the H_0 field orientates along z-direction then becomes:

$$E = g|\mu_B|H_0 S_z\,, \tag{2.3}$$

The projection of μ_e in z-direction is designated with symbol m_s, and for a spin ½ particle can have only two values: m_s = + ½ or m_s = – ½, where the negative value represents the alignment of the magnetic moment along the external magnetic field, and the positive value against it.

When the external magnetic field is interacting with the electron's magnetic moment, the difference in energy (*ΔE*) between m_s = - ½ and m_s = + ½ spin states is given by equation:[23]

$$\Delta\mathrm{E} = g\,\mu_B\,H_0\,\Delta\mathrm{m}_S\,, \tag{2.4}$$

where Δm_s has values ±1. ΔE is also the energy required to achieve a transition between the two spin states. In EPR this energy comes from oscillating magnetic field (H_1 or B_1) of microwave (MW) irradiation, where H_1 is oriented perpendicular to the H_0:

$$\Delta \mathrm{E} = h\nu = g\,\mu_B H_0\,, \qquad (2.5)$$

where ν is the frequency in Hertz. In a typical EPR experiment at X-band the frequency of the exciting radiation is around 9.5 GHz. Due to using a resonant cavity coupled to a specific frequency, it is practical to fix the frequency and sweep the H_0 with a laboratory magnet, so that at resonance the absorption of MW energy occurs according to Equation 2.5 above.

The interaction of the electron magnetic moment with the external magnetic field is called *The Zeeman Effect*. When an external magnetic field is applied it introduces a net magnetization in the sample along the H_0 (z-direction), while the components perpendicular to the H_0 (x- and y-directions) are averaged out. In the absence of the external magnetic field the two m_S states are degenerate, i.e. have same energy. Figure 2.1 summarises the interaction between MW irradiation ($h\nu$) and μ_e during an EPR experiment, when the H_0 field is swept and the degeneracy lifted. A resonance condition is achieved when the energy of the irradiation matches the energy difference between the m_s = - ½ and m_s = + ½ spin states.

The population difference Δn of the states can be represented as:[24]

$$\Delta n = n_{-1/2} - n_{+1/2}\,, \qquad (2.6)$$

Where $n_{-1/2}$ = ½(N + Δn), $n_{+1/2}$ = ½(N - Δn) and $N = n_{-1/2} + n_{+1/2}$. Assuming that spins are isolated, the rate of change of Δn follows first order kinetics:

$$\frac{d\Delta n}{dt} = -2n_{-1/2}P_{\uparrow} + 2n_{1/2}P_{\downarrow}\,, \tag{2.7}$$

Where $P_{\uparrow}$ and $P_{\downarrow}$ are the probabilities of upward and downward transitions, respectively and the factor 2 appears because a single transition upwards or downwards changes Δn by 2. It has been shown that in steady state where $d\Delta n/dt = 0$:

$$\Delta n^{ss} = n_{-1/2}{}^{ss} - n_{+1/2}{}^{ss} = N\frac{P_{\downarrow} - P_{\uparrow}}{P_{\downarrow} + P_{\uparrow}}\,, \tag{2.8}$$

i.e. population difference exists due to Boltzmann distribution even if the probabilities of the upward and downward transitions are equal, which can be represented by the Boltzmann distribution:

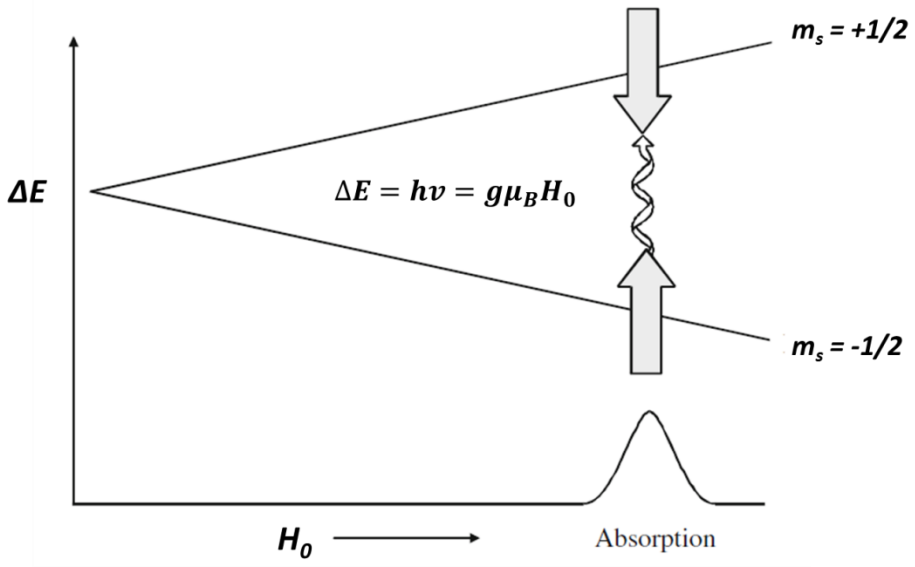

Figure 2.1. The Zeeman Effect during an EPR experiment. External magnetic field (H_0) is swept while the microwave radiation ($h\nu$) is kept constant. At resonance the energy difference between the spin states match the exciting energy, an absorption of magnetic component of the microwave radiation occurs, and an electron is promoted from parallel m_s = - ½ to a higher energy antiparallel m_s = + ½ spin state. (Modified from ref. [23] pp. 2)

$$\frac{n_{+1/2}}{n_{-1/2}} = e^{-\frac{\Delta E}{k_B T_s}}, \quad (2.9)$$

where $n_{+1/2}$ and $n_{-1/2}$ denotes the populations of anti-parallel (m_s = +1/2) and parallel (m_s = -1/2) states under thermal equilibrium, respectively, k_B is the Boltzmann constant and T_s is the sample temperature in Kelvins.

Because ΔE is very small, only about 6.2×10^{-24} J at X-band (H_0 = 334 mT, Equation 2.5) and the thermal energy available at room temperature is relatively large (4.1×10^{-21} J), the population difference is only ca. 1/1000 larger for the $m_s^{-1/2}$ state, making net absorption of energy and thus the EPR signal inherently very weak. An obvious way to increase the signal intensity is by increasing the population of the m_s = -1/2 state relative to m_s = +1/2. This can be accomplished for example by lowering the temperature (Equation 2.9) or increasing the ΔE by moving to higher frequencies and H_0 strengths.[22, 23]

2.3. The g-factor

In addition to *spin angular* momentum, an unpaired electron in a molecule also has an *orbital angular momentum* associated with it due to the electron's orbital motion. Therefore the magnetic moment of a free electron (Equation 2.1) must be modified to account for this additional source of magnetic moment:[22]

$$\boldsymbol{\mu} = \mu_B(\boldsymbol{L} + g_e\boldsymbol{S}), \quad (2.10)$$

where L is the *orbital angular momentum*, taking integer values depending on the orbital occupied by the electron. The Equation 2.10 is correct only if the *spin*- and *orbital angular*

momentum are independent from each other. In practise, although *orbital angular momentum* is often quenched and the electron's angular momentum is only due to its spin, *spin-orbit coupling* restores some of the *orbital angular momentum*, and the *g*-factor is adjusted from that of a free electron:

$$g_{eff} = \frac{hv}{\mu_B H_r}, \tag{2.11}$$

where g_{eff} is the effective *g*-factor accounting for the *orbital angular* contribution and H_r is the effective magnetic field at resonance. The g_{eff} is unique to any radical species because the *orbital angular momentum* of the electron is sensitive to the electron's surroundings depending on the molecule in question, and also varies according to which atom the electron is centred on.

As a result the resonance frequency in Equation 2.5 shifts from that of the free electron to account for the g_{eff}, and therefore the *g*-factor, in addition to hyperfine couplings discussed below, can be used as a fingerprint to identify a given molecule. For example an electron in a vicinity of carbon atom has a *g*-factor close to the free electron in a vacuum, whereas an electron close to a heteroatom can have *g*-factors around 2.004-2.006 and for metal centres can go up to 9 or 10 in some cases.[25]

Due to its relation to orbital motion, the *spin-orbit coupling* is an anisotropic (orientation dependent) interaction, meaning that the angular momentum varies depending on the direction of molecular frame relative to H_0. This orientation dependency is an important feature of EPR spectra for single crystal and powder samples in solid form, but also for large molecules in solvents with high viscosity. For small free radicals in solvents of low viscosity, such as the species represented in this thesis, the molecular tumbling is so rapid that g-

factor anisotropy is averaged out and only the isotropic g-factor needs to be accounted for.[22]

2.4. Hyperfine interaction

Certain nuclei such as hydrogen possess a nuclear magnetic moment, μ_N. The angular momentum of the unpaired electron spin couples with the magnetic moments of nuclei present in the molecule, a phenomenon which is called hyperfine interaction. The magnetic moment of the nucleus induces a small local magnetic field that is experienced by the unpaired electron and can either enhance or oppose the external magnetic field of the laboratory magnet. In the simplest case a single hydrogen nucleus with a spin number I = ½ couples with the unpaired electron. Depending on the orientation of the μ_N of the nucleus, either more or less external magnetic field is required to introduce the transition between the electron's energy state, and therefore two peaks are observed for the electron, one at lower magnetic field and the other at higher. This is depicted in Figure 2.2, where originally a single absorption peak is split into two, each centred H_I away from the original peak, where *a* is the hyperfine coupling factor describing the strength of the interaction between the electron and nucleus's magnetic moments.

Depending on the number and nature of the atomic nuclei with I≠0 in the paramagnetic species, the EPR absorption peak splits in a pattern characteristic to the molecule. This fact can be used as a fingerprint to identify the radical species and measure the localisation of the electron spin density within a molecule. As with the *g*-factor, the hyperfine interaction displays anisotropy in solids and for large molecules in viscous solvents, but for small free radicals in low viscosity solvents only the isotropic effect needs to be considered.[26]

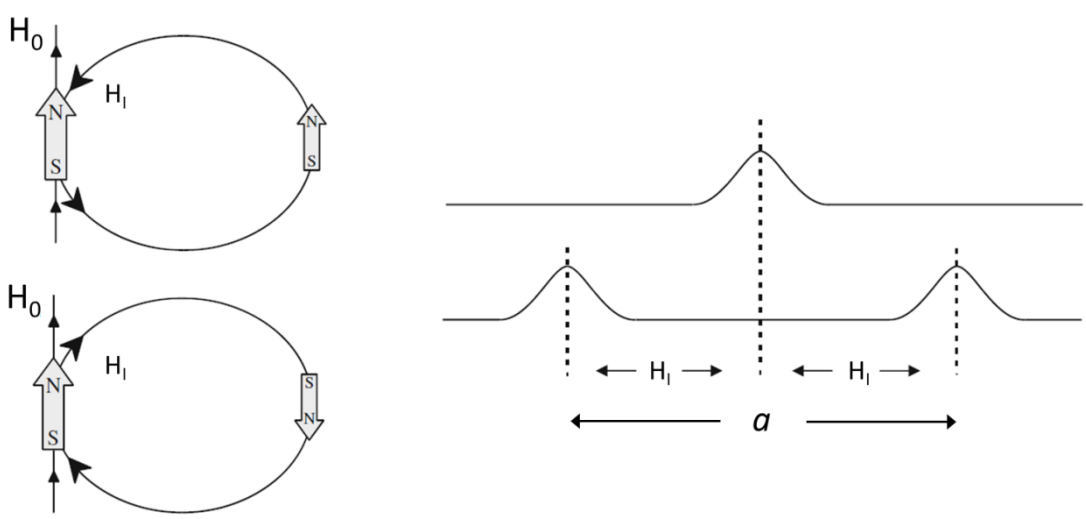

Figure 2.2. The effect of magnetic nucleus in the vicinity of the unpaired electron. Depending on the alignment of the nucleus relative to H_0, its magnetic moment either opposes or enhances the external magnetic field, causing the absorption peak to split. (Modified from ref. [23] pp. 4)

2.5. EPR spectrometer

The basic structure and function of a microwave bridge, the heart of a CW EPR spectrometer, is described below and the main components are shown in Figure 2.3. The MW source (A) of a modern CW EPR spectrometer is a Gunn diode, the power of which is hard to adjust quantitatively. Thus the microwaves are fed to an attenuator (B), which allows an accurate adjustment of the MW power. The circulator (C) guarantees that the irradiation from the Gunn diode doesn't go directly to the detector, but is guided to the cavity (an EPR resonator) (D) where the sample under investigation is situated. The cavity sits between laboratory magnet pole pieces and the DC magnetic field (H_0) can be swept by varying the current.

The cavity is coupled to the microwaves critically, meaning that the impedance of the cavity is matched with the transmission line and no MW power is reflected out to the detector. The cavity and its function is described in detail later, but as the H_1 field of the MW irradiation is absorbed during resonance when magnetic dipole transitions occur, the

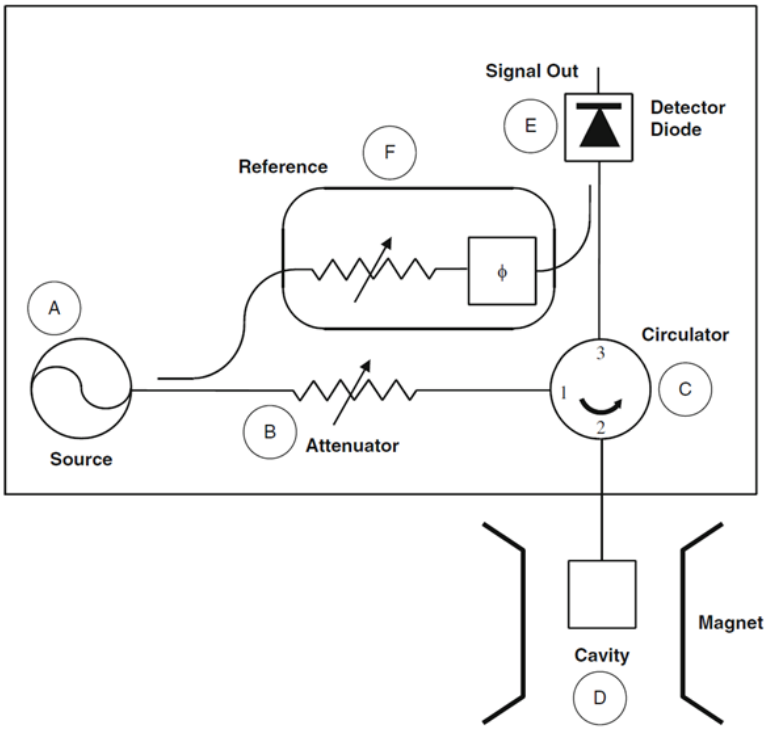

Figure 2.3. The microwave bridge of a CW EPR spectrometer and the main components. The MW irradiation follows a path A→B→C→D→C→E. The reference arm (F) allows the biasing of the detector to a "linear region" where the recorded signal is proportional a square root of the MW power incident to the resonator. (Modified from ref. [23] pp. 7)

critical coupling is lost and MW power is reflected from the cavity. The circulator now guides the MW energy to the detector (E) rather than allowing it to leak back to the source. Often a Schottky barrier diode is used as a detector, which converts the reflected MW power to an electric current. For optimal sensitivity and quantitative measurements the detector should operate in the so called "linear region", where the measured detector current and thus the EPR signal is proportional to the square root of the microwave power (P_0). This applies when the diode is biased to powers >1 mW and the detector current is approximately 200 μA. The microwave power for biasing of the detector is achieved through a reference arm (F), which has a phase shifter for matching the biasing irradiation at the detector with that originating from the resonator.[26]

2.6. Microwave power saturation

If the quantification of the spin concentration is the aim of the EPR experiment, it is crucial that the utilised microwave power level is below that at which saturation of the EPR signal starts to occur. For this it is imperative that the EPR spectroscopist is aware of how efficiently the resonator used converts the MW power to H_1 field. A good check for saturation is always to increase (or decrease) the MW power by four fold, which should increase (or decrease) the EPR signal by a factor of two, as long as the detector is operated in the "linear region". In practice this means deceasing or increasing the attenuation of the MW power by 6 dB. Some samples are defined as being "saturable", indicating that the Boltzmann distribution in Equation 2.9 is easily disturbed, and for these samples the considerations of saturation are especially valid.[23] The microwave power saturation is discussed in more detail in Chapter 4.

2.7. Magnetic field modulation

The Signal to Noise ratio (S:N) in CW-EPR is enhanced by utilising a phase sensitive detection (Figure 2.4). Helmhotz coils are placed on both sides of the sample so that their magnetic field orientates parallel to the H_0 field of the laboratory magnet. The coils are driven by an AC oscillator with a typical frequency v_{mod} of 100 kHz, and amplitude H_{mod}. Thus, as the H_0 scan crosses a resonance, at any given point the field oscillates between H_a and H_b, introducing an oscillation in detector current between i_a and i_b, which is proportional to the slope of the absorption peak. Due to the field modulation the detected EPR signal is a 1st derivative of the absorption peak.

Thus at EPR resonance the MW signal reflected from the resonator is "modulated" at v_{mod}, the signal is amplified and fed to the phase sensitive detector. At the phase sensitive

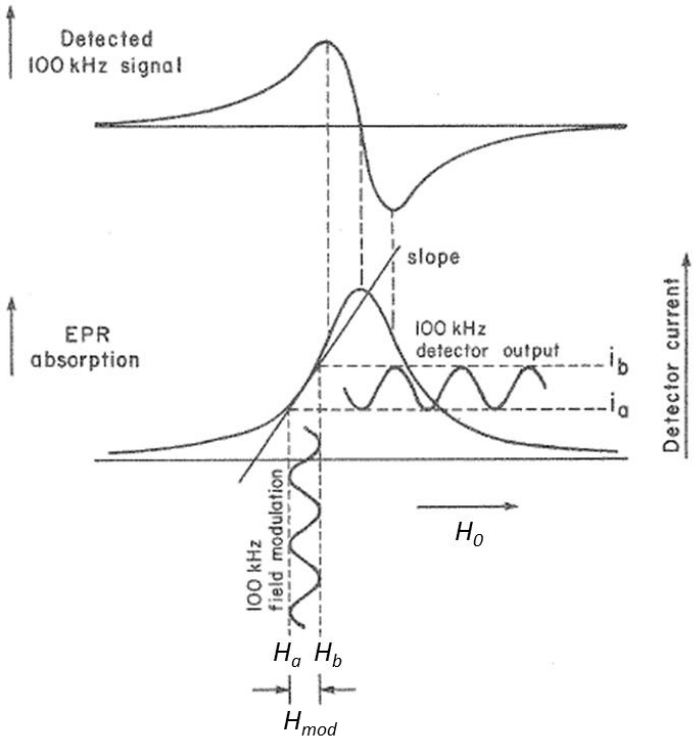

Figure 2.4. A schematic representation of the magnetic field modulation. As H_0 is swept by the laboratory magnet, a pair of Helmholtz coils introduce a sinusoidal oscillation with magnitude H_{mod} to the DC magnetic field. At any given point the modulated field oscillates between values H_a and H_b and thus the detector current also oscillates between i_a and i_b. Due to the modulating detector current the EPR spectrum is recorded as a first derivative. (Modified from ref. [27] pp. 526)

detector the EPR signal is combined with the signal driving the modulation coils, and all other frequencies except the v_{mod} are filtered out, which dramatically reduces the noise levels. Finally the DC output from the phase sensitive detector is sent to the computer and displayed as an EPR spectrum[27]

2.8. Relaxation and line width

In CW EPR the area under an absorption curve is proportional to the number of spins in the sample. As will be discussed in Chapter 4, the preferred method of quantification is by double integrating the 1st derivative signal to determine the area under the absorption curve, so that possible variations and differences in line widths and shapes can be accounted for. For example, in Figure 2.5 below, the area under both of the two absorption

lines is equal, but due to the difference in widths the height of the lines, or their first derivatives, is not a good indicator of the spin concentration. The mechanism and sources of line broadening are discussed briefly below.

When absorption of MW energy during resonance occurs, the spin system of the sample is heated and thermal equilibrium due to Boltzmann distribution (Equation 2.9) no longer holds. None the less, as the molecules in the spin system are coupled to their environment, or lattice, for example through thermal motion, the spin system loses energy to the environment and relaxes back to the equilibrium temperature in a process called *spin-lattice relaxation*. The characteristic time constant associated to this process is called the *spin-lattice relaxation time* (T_1). The line broadening due to T_1 can be considered in terms of the Heisenberg uncertainty principle:[28]

$$\Delta E\ \Delta t \geq \frac{h}{2\pi}, \tag{2.12}$$

where Δt can be replaced by T_1. If the line width is determined by T_1 and its value is very small, then the ΔE is large and the energy levels of the spin states will be smeared out, and the EPR lines will be broad. For example, a T_1 time of 10^{-9} seconds corresponds to a line width of ca. 60 Gauss, a typical value for example for transition metals.

When MW energy is absorbed by the sample, the net magnetization along the z-axis is

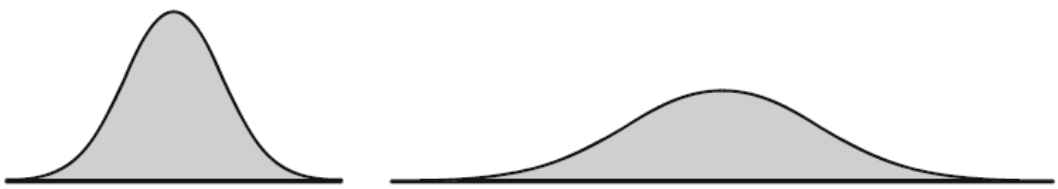

Figure 2.5. The effect of the width of the absorption line to the height of the line, when the area under the line remains the same. (Modified from ref. [23] pp. 5)

perturbed towards the x- and y-plane. This transverse magnetization starts to relax immediately towards the initial equilibrium value of zero, a phenomenon called a *spin-spin* or *transverse relaxation*, denoted by a symbol T_2. For small free radicals in solution T_1 is typically much longer than T_2, and therefore the line width (ΔH_{pp}) is determined by T_2:[23]

$$\Delta H_{pp} = \frac{2}{\sqrt{3}\gamma_e T_2} = \frac{6.56 \times 10^{-8}}{T_2} G \,, \qquad (2.13)$$

where γ_e is the gyromagnetic ratio of an electron. Equation 2.13 relates the line width to the transverse relaxation time, providing that the microwave power and H_{mod} amplitudes are not broadening the line, as discussed in Chapter 4,

The sources of line broadening can be divided to inhomogeneous and homogeneous, where the line shape due to inhomogeneous broadening is typically Gaussian, and homogeneous broadening produces Lorentzian shapes. The most important sources for each type are discussed below.[24]

- *Inhomogeneous broadening*:

For inhomogeneous broadening the static, or time averaged magnetic field varies between individual spins, and the typical sources are:

I. If the H_0 over the sample is not uniform, then individual 'spin packets' within the sample come to resonance at different times when the H_0 is swept, and the recorded spectrum consists of individual absorption lines, each shifted with respect to each other.

II. If the species under study has several magnetic nuclei, the number of hyperfine components can lead to an overlap of the EPR lines, for example F centres in KCl.

III. In solid state, or for large molecules in viscous solvent, spins experience anisotropic interaction, where the local magnetic field effecting individual spins varies due to g and hyperfine anisotropies.

- *Homogeneous broadening:*

For homogeneous broadening the time averaged magnetic field is the same at each dipole, but the instantaneous field fluctuates, making the homogeneous processes dynamic in nature, for example in case of small free radicals in low viscosity solvent:

I. In *electron-spin exchange*, electron spins from two close by radical molecules exchange their spin orientations, indicating that the effect is concentration dependent, as shown by Figure 2.6 for di-*t*-butyl nitroxide radical. A very low radical concentration yields spectrum (a), whereas higher concentration shows clear line broadening (b). A further increase in concentration yields (c) and finally (d), an *exchange-narrowed* spectrum due to the time-averaged hyperfine field approaching to zero. The spin exchange interaction should be separated from dipole-dipole effect, which is much smaller in liquids contributing only a little towards line broadening.

II. Electron transfer can occur between a radical species and its diamagnetic "parent" form, for example for naphthalene:[29]

$$naph_1^{-\bullet} + naph_2 \leftrightharpoons naph_1 + naph_2^{-\bullet} \qquad (2.14)$$

The second order rate constant for the electron transfer mechanism can be a couple of orders of magnitude smaller compared to the *electron-spin exchange* mechanism, indicating the smaller significance of electron transfer towards line broadening, at least for small free radicals in solution phase.[30]

III. Proton transfer mechanism can change the magnetic environment of an electron, if the paramagnetic molecule changes nuclei with the solvent. A good example of this type of broadening is the CH_2OH radical, where the CH_2 group gives a pH independent triplet, but the doublet splitting of the hydroxyl proton is pH dependent due to the exchange with the solvent proton.[31]

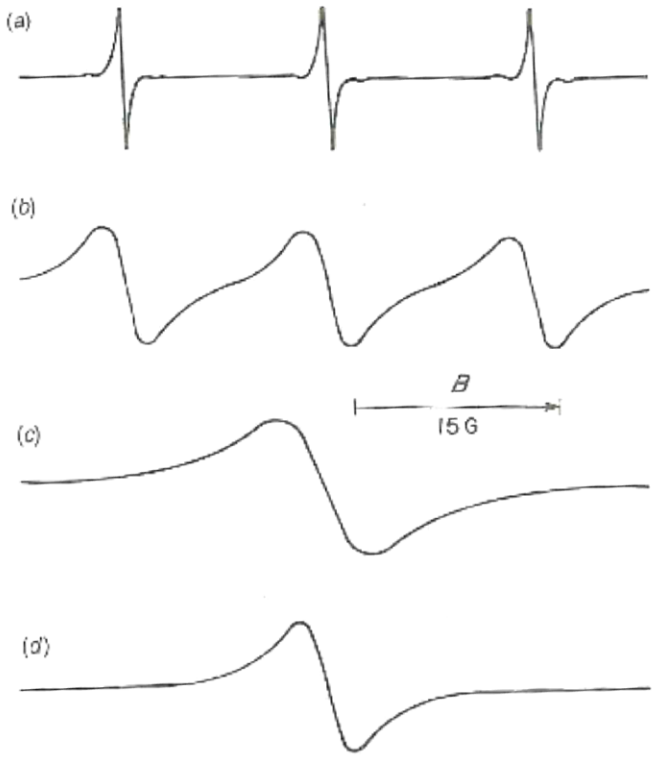

Figure 2.6. The effect of increasing radical concentration (a to d) towards the line broadening for di-*t*-butyl nitroxide radical in ethanol at room temperature. (Modified from ref. [24] pp. 323)

2.9. The EPR resonator

The main function of an EPR resonator, such as the TE_{102} cavity resonator shown in Figure 2.7, is to store MW energy and to amplify the weak signals originating from the sample. When critically coupled to the microwaves, a standing wave exists inside the cavity and the amplitudes of the electric (E_1) and H_1 components of the electromagnetic irradiation are enhanced. The design of the resonator allows the placement of the sample in the maximum H_1 field, where the E_1 has its minimum value and power loss due to the absorption by the electric dipoles in the sample is minimised. This is especially important when working with samples of high dielectric loss such as water, as discussed in more detail in Chapter 4.[32]

When the resonator containing the sample of interest is critically coupled to the transmission line, no MW radiation is reflected to the detector. When H_0 is swept to meet the magnetic resonance condition during an EPR experiment, MW power is absorbed, the resonator is no longer critically coupled and the reflected power is detected as an EPR signal.

The performance of a resonator is characterized by its Quality Factor (Q-value or Q), which

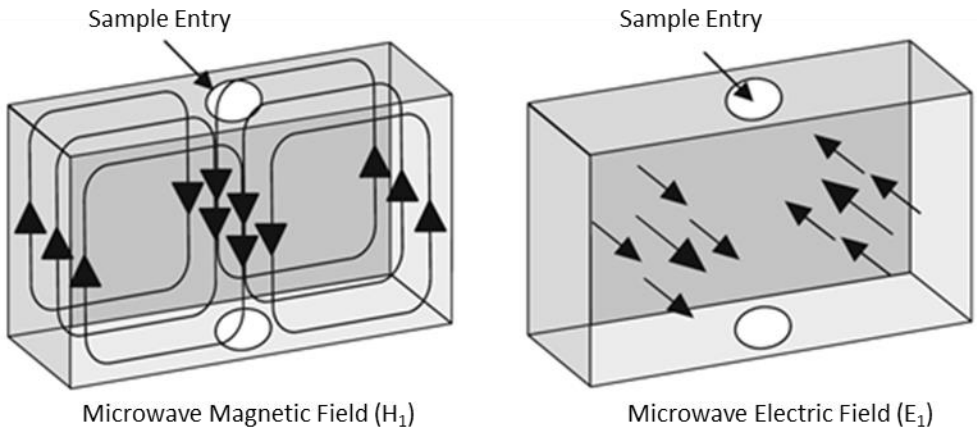

Figure 2.7. The orientation of electric E_1 and magnetic H_1 fields in rectangular TE_{102} cavity resonator. (Modified from ref. [23] pp. 9)

is defined as:

$$Q = \frac{2\pi(maximum\ MW\ energy\ stored\ in\ the\ resonator)}{energy\ dissipated\ \ per\ microwave\ cycle}, \quad (2.15)$$

a measure of how much MW energy can be stored into the resonator and to the H_1 field responsible for driving the EPR transitions. Q can also be rewritten as:

$$Q = \frac{v_{res}}{\Delta v}, \quad (2.16)$$

where v_{res} is the resonator frequency and Δv is the width of the resonance curve at half height. The EPR signal 1st derivative peak to peak amplitude (ΔS_{pp}), determining S:N, is proportional to both the Q factor and the filling factor (η):

$$\Delta S_{pp} \propto \eta \times Q, \quad (2.17)$$

where η is defined as:

$$\eta = \frac{\int_s H_1^2 dV_s}{\int_r H_1^2 dV_r}, \quad (2.18)$$

the ratio of sample volume (s) over resonator volume (r), both integrated for H_1^2.

For the sake of experimental work, two Q-values should be distinguished. Firstly Q_U is the unloaded quality factor without a sample inserted to the resonator, the value of which is dependent on the resonator geometry, operating frequency and the materials the resonator is built of. Q_L is the quality factor with a sample and sample holder inserted to the resonator, the magnitude of which is greatly influenced by sample properties. As

discussed in Chapter 3 for electrochemical EPR experiments, often performed with samples of high dielectric loss, the Q_L can vary greatly from Q_U.[33]

The Equation 2.17 indicates that both the Q factor and η should be maximised for optimum S:N. However, when a sample is inserted into the resonator, some dielectric losses occur due to the absorption of MW energy by the electric dipoles in the sample. This power loss lowers the resonator Q the larger the sample and greater the dielectric loss of the sample. Therefore a compromise between η and the resonator Q has to be found to maximize the product $\eta \times Q$,[34] depending on the type of resonator used, sample material's size, shape and dielectric constant and the frequency used. As discussed in Chapters 3 and 4, this issue is further highlighted in electrochemical EPR, as good electrochemical response often requires solvents with high dielectric constants forcing η to be reduced to prevent excessive power loss.

2.9.1. Loop gap resonator (LGR)

Loop Gap Resonator (LGR) is a novel sample resonator for Magnetic Resonance (MR) purposes. The design was first described in the 1940s[35] for magnetron designs and later on by Hardy and Whitehead[36] for NMR purposes in the frequency region of 200 to 2000 MHz. The LGR is based on lumped circuit concepts and approximates to an RLC-circuit. Typical dimensions for lumped circuit device are 1/10 to 1/100 of the used wavelength, E_1 and H_1 fields are spatially separated, oriented perpendicular to each other, and inductance and capacitance are easily identifiable.[37]

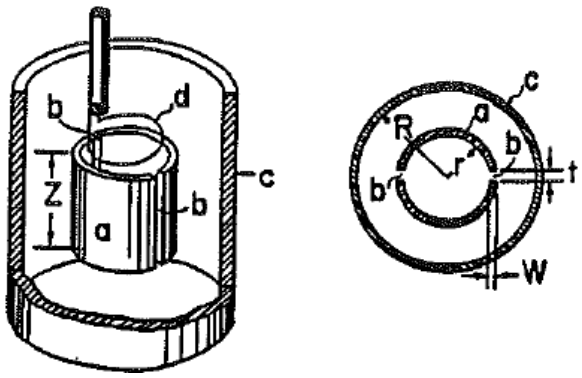

Figure 2.8. One loop two gap resonator. a, loop; b, gaps; c, shield; d, inductive coupler. Critical dimensions: Z, resonator length; r, resonator radius; R, shield radius; t, gap separation; W, gap width. (From ref. [39])

The first resonator structure reported for X-band EPR by Froncisz and Hyde in 1982 is shown in Figure 2.8. The structure consists of a loop (a) inside which the H_1 field is concentrated, two gaps (b) acting as capacitors and condensing the electric field, surrounded by a shield (c) to prevent the structure from radiating. (d) is the inductive coupler for coupling the resonator to the microwaves. As critical dimensions (Z) represent the resonator length, (r) is the resonator radius, (R) the shield radius, (t) the gap separation and (W) the gap width. The sample tube is inserted concentrically through the loop (a) where the H_1 field is concentrated, and thus the sample is subjected only to the fringing electric fields at the gaps. The return flux of the MW magnetic field is confined to the annular region between the loop and the shield.

The capacitance (*C*) and inductance (*L*) of one loop, one gap LGR can be expressed as:

$$C = \frac{\epsilon W Z}{t}, \tag{2.19a}$$

$$L = \frac{\mu_0 \pi \mathrm{r}^2}{Z}, \tag{2.19b}$$

where ϵ is the dielectric constant of the material between the gap(s), μ_0 is the permeability of free space. The resonance frequency (v_{res}) of this LGR approximates to:

$$2\pi v_{res} = \frac{1}{(LC)^{1/2}}, \tag{2.20}$$

By increasing the no. of gaps (no. of gaps goes to the denominator in Equation 2.19a) the capacitance can be reduced and larger L (or r) can be accommodated. This allows larger sample volumes to be used while keeping the resonance frequency high, as long as the dimensions of the LGR are kept below one quarter of the wave length.[38] Thus by incorporating multiple loops and gaps it is possible to manufacture LGR's with frequencies ranging from <1 GHz to 35 GHz. Common resonator geometries are shown in Figure 2.9 below, where the number of loops and gaps effect the resonance frequency and the distribution of the H_1 field in the loops.

The resonator can be machined from ceramic Macor and electroplated with silver to obtain high conductivity surfaces and relatively high Q values, while the shield is made from silver plated fiberglass epoxy.[38-40]

A typical LGR has lower Q-factor than cavity resonators, but larger η as the resonator is significantly smaller, and therefore the S:N ratio depends on the relative magnitudes of Q and η (Equation 2.17). Because the E_1 field is confined to the gap(s) of the LGR, larger

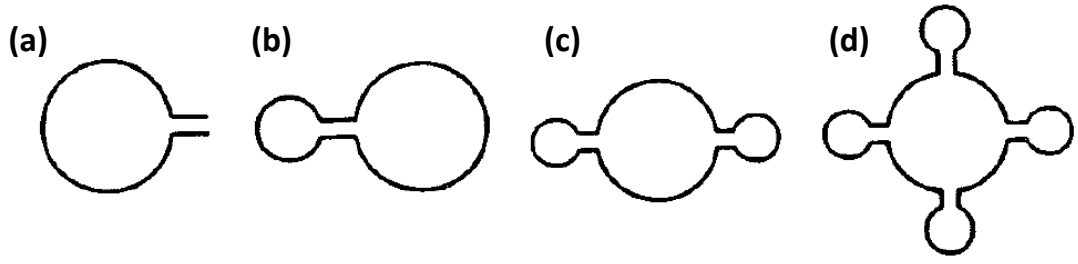

Figure 2.9. Different LGR topologies: (a) one loop, one gap; (b) two loop, one gap; (c) three loops, two gaps; (d) 5 loops, 4 gaps. [Modified from ref. [38] pp. 175]

volumes of *lossy* sample with high dielectric constant can be inserted to the sample loop and thus bigger η obtained. For example, a sample in a standard 4 mm OD, 3 mm ID sample tube running through the entire length of the traditional TE_{102} cavity resonator has a η of 0.01 (maximum η for any resonator is 1), while an order of magnitude larger values can be obtained for LGR.[41]

2.9.2. EPR sample classification

An EPR sample classification system considers 1) whether the sample is saturable, 2) is limited in size or amount and 3) does the sample have a large dielectric loss. *Yes* and *no* answers to the questions then divide samples to eight different classes (Figure 2.10) depending on their properties as follows:[42]

1. Type: Unlimited sample, negligible dielectric loss

The resonator can be filled with sample, so η is unity and the EPR signal scales with Q factor. Whether the sample saturates or not, the larger Q factor and volume of the cavity resonators always give it an advantage over LGR.

2. Type: Limited sample with varying dielectric loss, saturable and non-saturable

For sufficiently small samples, the power loss due to dielectric loss is minimal, and an efficiency parameter ($\mathbf{\Lambda}$) describing the efficiency of converting MW power to H_1 can be used to compare LGR to cavities:

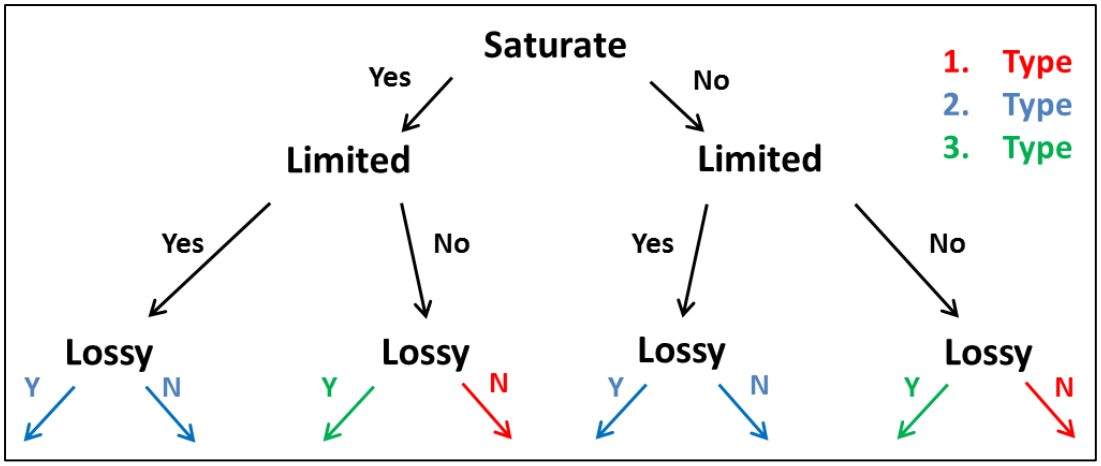

Figure 2.10. Classification of EPR samples to eight different categories based on whether they saturate, are of limited amount or size and whether they have a high dielectric constant.

$$\Lambda_x = \frac{H_1}{P_0^{1/2}}, \tag{2.21}$$

where subscript x denotes the type of resonator, either LGR or cavity and H_1 is specifically the peak magnetic field intensity *at sample position* and P_0 is the incident power to the resonator . For X-band cavities the $\boldsymbol{\Lambda}$ is close to 1 when power is in watts and H_1 in Gauss, whereas for LGRs values up to 10 have been realised. Therefore an order of magnitude sensitivity improvements can be obtained due to the larger efficiency of converting MW power to the H_1 field in LGR for non saturable samples, or when otherwise limited by the MW power. For these four sample classes with *limited* designation, a LGR can provide substantial benefits especially when accounting for the larger η obtainable.

3. Type: Unlimited samples with high dielectric loss, saturable and non-saturable

As mentioned above, the LGR is favourable in these cases, where the lossy sample is confined away from the electric field within the resonator. After optimising the sample volume in LGR and cavity, the sensitivities tend to be similar in concentration basis, but the smaller size of the LGR means that in terms of absolute sensitivity LGR is favourable, although this is dependent on the particular LGR geometry employed.[38, 42]

For Electrochemical EPR (EC-EPR) the systems tend to be of 2nd and 3rd type. First of all the radical species is always limited to the diffusion field of the EC experiment, which can give a very small η especially for short lived species, thus making the use of LGR beneficial. Also as EC favours lossy solvents, the sample volume must be limited to amounts where acceptable Q-factor is still achieved. Secondly, small organic radicals in a solution phase tend to be difficult to saturate, and the larger $\mathbf{\Lambda}$ values for the LGR give an additional advantage in terms of effective H_1 over the sample.

2.9.3. Sensitivity comparison

The geometry of the LGR can be extremely flexible, and the resonator can be designed with a specific sample type in mind, rather than adapting the sample to the mode of the resonator. The geometry also affects the η and Q factor achievable, and thus the sensitivity comparisons with traditional cavity resonators should be made on individual basis depending on the properties of the sample.

Figure 2.11 shows a sensitivity comparison between one-loop one-gap LGR (A) and TE_{102} cavity resonator (B) in the case of Type 2 sample, limited in size and with high dielectric loss. Using 0.1 mM TEMPAMINE (4-Amino-2,2,6,6-tetramethylpiperidino-1-oxyl) in aqueous solution, a sample tube with inner diameter (ID) of 0.4 mm was placed in both resonators, the effective sample volume in both of the resonators being roughly equal due to the LGR

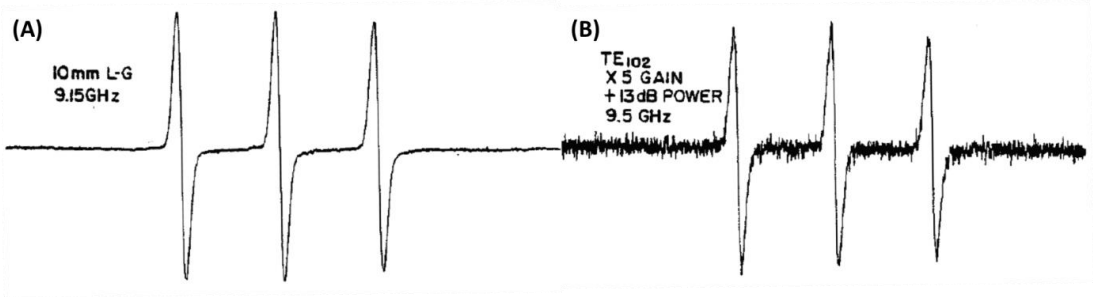

Figure 2.11. The sensitivity comparison between one loop one gap LGR (A) and TE_{102} cavity resonator for 0.1 mM of stable TEMPAMINE radical in aqueous solution in 0.4 mm ID sample tube. Due to the design of the LGR the effective length of the sample inside both of the resonators was the same, and the effective H_1 field at the sample was adjusted to same value. (Modified from ref. [39])

design. To measure the signal under equal H_1 field over the sample, the MW power utilized for the cavity resonator had to be adjusted 13 decibels (dB) higher (20 times the MW power) than that for LGR. The resulting spectrum for the LGR showed 5 times larger signal intensity demonstrating the advantageous properties of the LGR design.[38]

2.10. The absolute sensitivity

The minimum number of spins detectable (N_{min}) in EPR is:[43]

$$N_{min} = \frac{12\pi V_c k_B T_s \Gamma}{\mu_0 g^2 {\mu_B}^2 S(S+1) H_r Q_U} \left(\frac{F k_B T_d b}{P_0}\right)^{1/2}, \qquad (2.22)$$

where the symbols have the following meaning: V_c - volume of the cavity (TE_{102} mode assumed), Γ - line width of the absorption line (half-width half-height), Q_U - effective unloaded Q factor of the cavity, F_n - noise factor for sources other than thermal (F_n = 1 for ideal spectrometer), T_d - detector temperature, b - band width of the entire detecting and amplifying system.

The N_{min} equals ca. 10^{11} spins, when typical values are inserted to the equation, which depending on the sample volume suggests concentrations of 1-10 nM. None the less, this

approximation neglects several sample, resonator and spectrometer related variables and is more akin what EPR spectrometer manufacturers would report.

Equation 2.22 shows the complications related to quantitative investigations in EPR, as the signal is dependent on several parameters. The equation also omits several sample, resonator and EPR spectrometer settings related variables, which will be discussed in Chapter 4, and thus analytical measurements and the quantification of the absolute number of spins in EPR can be extremely challenging. This situation is further complicated by the insertion of the electrochemical cell into the resonator when in situ EC-EPR experiments are performed, a topic covered in the next section.

References

1. M. Brustolon, in *Electron Paramagnetic Resonance - A Practitioner's Toolkit*, eds. M. Brustolon and E. Giamello, John Wiley & Sons Inc., Hoboken, New Jersey, 2009, pp. 83-108.
2. B. Yamada, D. G. Westmoreland, S. Kobatake and O. Konosu, *Prog. Polym. Sci.*, 1999, **24**, 565-630.
3. M. Lucarini, G. F. Pedulli, M. V. Motyakin and S. Schlick, *Prog. Polym. Sci.*, 2003, **28**, 331-340.
4. M. A. Morsy and M. H. Shwehdi, *Spectrochim. Acta A*, 2006, **63**, 624-630.
5. W. Stachowicz, G. Strzelczak-Burlinska, J. Michalik, A. Wojtowicz, A. Dziedzic-Goclawska and K. Ostrowski, *J. Sci. Food Agr.*, 1992, **58**, 407-415.
6. G. Vanhaelewyn, J. Sadlo, F. Callens, W. Mondelaers, D. De Frenne and P. Matthys, *Appl. Radiat. Isot.*, 2000, **52**, 1221-1227.
7. N. D. Yordanov and V. Gancheva, *Appl. Radiat. Isot.*, 2000, **52**, 195-198.
8. E. Sagstuen and E. O. Hole, in *Electron Paramagnetic Resonance - A Practitioner's Toolkit*, eds. M. Brustolon and E. Giamello, John Wiley & Sons, Inc., Hoboken, New Jersey, 2009, pp. 325-382.
9. A. C. Díaz, S. M. Velurtas, M. L. Espino and J. L. Fenucci, *J. Agr. Food Chem.*, 2014, **62**, 12326-12331.
10. M. Polovka, V. Brezová and A. Staško, *Biophys.Chem.*, 2003, **106**, 39-56.
11. I. Spasojevic, *Crit. Rev. Clin. Lab. Sci.*, 2011, **48**, 114-142.
12. M. J. Davies, in *Electron Paramagnetic Resonance - A Practitioner's Tool kit*, John Wiley & Sons, Inc. , Hoboken, New Jersey, 2009, pp. 427-450.
13. M. Sentjurc and R. P. Mason, *Free Rad. Biol. Med.*, 1992, **13**, 151-160.
14. X. Duan, S. Indrawirawan, H. Sun and S. Wang, *Catal. Today*, 2015, **249**, 184-191.
15. D. Goldfarb, in *Electron Paramagnetic Resonance - A Practitioner's Toolkit*, eds. M. Brustolon and E. Giamello, John Wiley & Sons, Inc., Hoboken, New Jersey, 2009, pp. 451-487.
16. S. Indrawirawan, H. Q. Sun, X. G. Duan and S. B. Wang, *J. Mat. Chem. A*, 2015, **3**, 3432-3440.
17. S. Van Doorslaer and D. M. Murphy, in *Epr Spectroscopy: Applications in Chemistry and Biology*, eds. M. Drescher and G. Jeschke, 2012, vol. 321, pp. 1-39.
18. L. N. Blinov, *Glass Phys. Chem.*, 2003, **29**, 203-223.
19. A. Popa, O. Raita, M. Stan, O. Pana, G. Borodi and L. M. Giurgiu, *Appl. Magn. Res.*, 2012, **42**, 453-462.
20. C. F. Young, E. H. Poindexter, G. J. Gerardi, W. L. Warren and D. J. Keeble, *Phys. Rev. B*, 1997, **55**, 16245-16248.
21. M. E. Zvanut, *J. Phys. Condens. Matter*, 2004, **16**, R1341-R1367.
22. C. Corvaja, in *Electron Paramagnetic Resonance - A Practitioner's Toolkit*, eds. M. Brustolon and E. Giamello, John Wiley & Sons, Inc., Hoboken, New Jersey, 2009, pp. 3-35.
23. G. R. Eaton, S. S. Eaton, D. P. Barr and R. T. Weber, *Quantitative EPR*, Springer-Verlag, Wien, 2010.
24. J. A. Weil and J. R. Bolton, in *Electron spin Resonance: Theory and Practical Applications*, John Wiley & Sons, Inc., Hoboken, New Jersey, 2007, pp. 301-356.
25. J. R. Bolton, in *Biological Applications of Electron Spin Resonance*, eds. H. M. Swartz, J. R. Bolton and D. C. Borg, John Wiley & Sons, Inc., New York, London, Sydney, Toronto, 1972, pp. 11-61.

26. J. A. Weil, J. R. Bolton and J. E. Wertz, *Electron Paramagnetic Resonance: Elemental Theory and Practical Applications*, John Wiley & Sons, Inc., New York, Toronto, 1994.
27. J. R. Bolton, D. C. Borg and H. M. Swartz, in *Biological Applications of Electron Spin Resonance*, eds. H. M. Swartz, J. R. Bolton and D. C. Borg, Wiley-Interscience, New York, 1972, pp. 63-118.
28. J. E. Wertz and J. R. Bolton, *Electron Paramagnetic Resonance: Elemental Theory and Practical Applications*, 1972.
29. R. L. Ward and S. I. Weissman, *J. Am. Chem. Soc.*, 1957, **79**, 2086-2090.
30. T. A. Miller and R. N. Adams, *J. Am. Chem. Soc.*, 1966, **88**, 5713-5714.
31. H. Fischer, *Mol. Phys.*, 1965, **9**, 149-152.
32. J. E. Wertz and J. R. Bolton, in *Electron Spin Resonance: Elementary Theory and Practical Applications*, McGraw-Hill, New York, 1972, pp. 21-37.
33. D. P. Dalal, S. S. Eaton and G. R. Eaton, *J. Magn. Res.*, 1981, **44**, 415-428.
34. P. Hofer, in *Electron Paramagnetic Resonance, A Practitioners Toolkit*, eds. M. Brustolon and E. Giamello, John Wiley & Sons, Inc., New Jersey, 2009, pp. 37-82.
35. N. Kroll, in *Microwave Magnetrons*, ed. G. B. Collins, McGraw-Hill Book Company, New York, Toronto, London, 1948, vol. 6, pp. 49-82.
36. W. N. Hardy and L. A. Whitehead, *Rev. Sci. Instrum.*, 1981, **52**, 213-216.
37. J. S. Hyde and W. Froncisz, in *Electron Spin Resonance*, ed. M. C. R. Symons, 1986, vol. 10A, pp. 175-184.
38. W. Froncisz and J. S. Hyde, *J. Magn. Reson.*, 1982, **47**, 515-521.
39. M. Mehdizadeh, T. K. Ishii, J. S. Hyde and W. Froncisz, *IEEE T. Microw. Theory.*, 1983, **31**, 1059-1064.
40. G. A. Rinard, R. W. Quine, S. S. Eaton and G. R. Eaton, *J. Magn. Reson. Ser. A*, 1993, **105**, 137-144.
41. G. A. Rinard and G. R. Eaton, in *Biomedical EPR, Part B: Methodology, Instrumentation, and Dynamics*, eds. S. Eaton, G. Eaton and L. Berliner, Springer US, 2005, vol. 24/B, pp. 19-52.
42. J. S. Hyde and W. Froncisz, in *Advanced EPR: applications in biology and biochemistry*, ed. A. J. Hoff, ELSEVIER, 1989, pp. 1-29.
43. J. A. Weil and J. R. Bolton, in *Electron Paramagnetic Resonance: Elementary Theory and Practical Applications*, 2 edn., 2007, pp. 537-566.

Chapter 3 - Electrochemical EPR (EC-EPR)

As EPR detects paramagnetic species and electrochemistry inherently produces them at some point of reduction/oxidation processes, the combination of the two seems extremely favourable. The proof of concept became in the late 50's and early 60's by scientists like Maki, Geske and Austen et al.[1-3] Since then, several reviews have been written, mostly focusing on different electrochemical EPR cell designs that have been developed to tackle various electrochemistry related problems.[4-9] Some of these concentrate on electrochemical EPR, while the latest ones reflect the recent developments in the field discussing Spectroelectrochemistry. This reflects the multi-technique approach, where electrochemistry, EPR, UV-Vis, Raman and IR spectroscopy are coupled together to provide as complete understanding as possible of electrochemical processes. Also a review of the recent literature reveals that in modern day research, especially in organometallic/biochemical field, electrochemistry and EPR are used equally in tandem with a wide variety of other techniques to gain complete understanding of variety of biologically relevant systems.[10-13]

3.1. Perturbation functions

The applicability of EC and EPR has been discussed by Goldberg & McKinney in terms of differences in the energies associated to the fundamental transitions, which for the two techniques are different enough not to interfere with each other even if electrochemistry and EPR are applied simultaneously.[14]

In organic and inorganic chemical systems, each molecular orbital has its own energy level, or eigen value. For example, when an electron is added to a molecule during an electrochemical reduction, it is placed to a molecular orbital (MO) with a characteristic energy, determined against a chosen zero point, i.e. a reference electrode in electrochemistry. Therefore, the thermodynamic data recorded during electrochemical experiments relates to eigenvalues of the system, and have a typical energy of a few electron volts[15] (eV).

Each MO has its characteristic shape and spatial distribution called an eigen function, describing the distribution probability for electrons occupying that orbital, and thus the probability of finding a given electron from particular volume of space. Parameters obtained from an EPR experiment give information about these electron probability distributions. The energy of MW irradiation at X-band, around 9.5 GHz (wave length of ca. 3.16 cm) can be calculated due to relation:

$$E = h\nu = \frac{hc}{\lambda}, \qquad (3.1)$$

where ν is the frequency in hertz, c is the speed of light in meters per second and λ is the wavelength of the MW radiation in meters. Evaluation of the equation shows that typical energies involved in X-band EPR are around 3.9×10^{-5} eV, about 4-5 orders of magnitude lower than the energies involved in electrochemistry, and thus the two techniques do not interfere with each other.

3.2. The motivation for EC-EPR

Early reviews in EC-EPR already acknowledged that whereas electrochemistry can reveal thermodynamic and kinetic parameters of electrode reactions, EPR can be used to identify radical intermediates and products via *g*-values and hyperfine couplings.[2, 16-18] For complicated electrode reactions this can be of great help in determining the full reaction mechanism involved, as electrochemistry alone cannot characterise unambiguously some of the steps involved in Figure 3.1.[19-22] EPR also allows the determination of kinetic parameters, such as reaction rates and radical lifetimes,[23-26] and in the case of very short lived radicals spin trapping can be utilised to extend the applicability of EPR in electrochemistry.[27-30]

Thus EPR can provide complementary information and additional insights to electrode reactions, as individual species can be monitored in complex mixtures, and the recorded data is not distorted for example by secondary electroactive intermediates.[31, 32] Figure 3.1 overlay the possible processes related to electrochemical systems, which include complex mass transport phenomena, adsorption/desorption of species at the electrode surface,

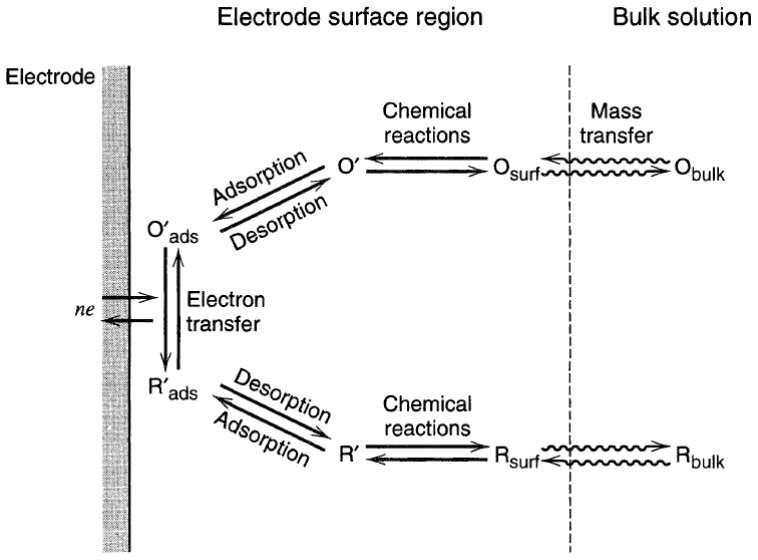

Figure 3.1. The electrochemical interface and processes complicating the interpretation of EC data. O represents Oxidized and R Reduced form of an analyte. (Modified from ref. [34] pp. 23)

heterogeneous reactions, electron transfers and homogeneous chemical transformations of intermediates.[33, 34]

Initially electrochemistry provided EPR spectroscopists a convenient and flexible way to produce radical species through electrolysis, which is reflected by the relatively crude design of these setups. Nonetheless, compared to for example alkali metal reduction, where studies were often limited to organic solvents such as tetrahydrofuran or 1,2-dimethoxyethane, a wide variety of solvents (even water) now became accessible. In addition to selecting different electrode materials and geometries, the potential applied to the electrode could be adjusted for reduction and oxidation processes, and the electrolysis time controlled in precise fashion, giving much better overall control over the experiments compared to chemical reduction. Also alkali metal ions can complicate the interpretation of the EPR spectra, whereas for the large organic tetraalkylammonium cations applicable in electrochemistry this effect is much weaker.[18, 20, 35-38]

Below in Scheme 3.1 is a typical early example of the utility of EC-EPR, where the combination of cyclic voltammetry (polarography) and EPR was utilized to validate an entire reaction mechanism for the reduction of 4-aminobenzonitrile in dimethylformamide (DMF).[20] The reduction at -3.3 V vs $Ag|AgClO_4$ produced an EPR spectrum showing 2 equivalent I=1 nuclei and two sets of 4 I=1/2 nuclei. Considering the solvent system and starting species these nuclei were concluded to be ^{14}N and ^{1}H, respectively. The first reduction step was determined to be a reversible one electron process followed by an irreversible chemical elimination reaction step leaving a neutral radical which then goes through a dimerization. The dimerized product can go through a further charge transfer step to yield an EPR active 4,4'-dicyanobiphenyl radical.

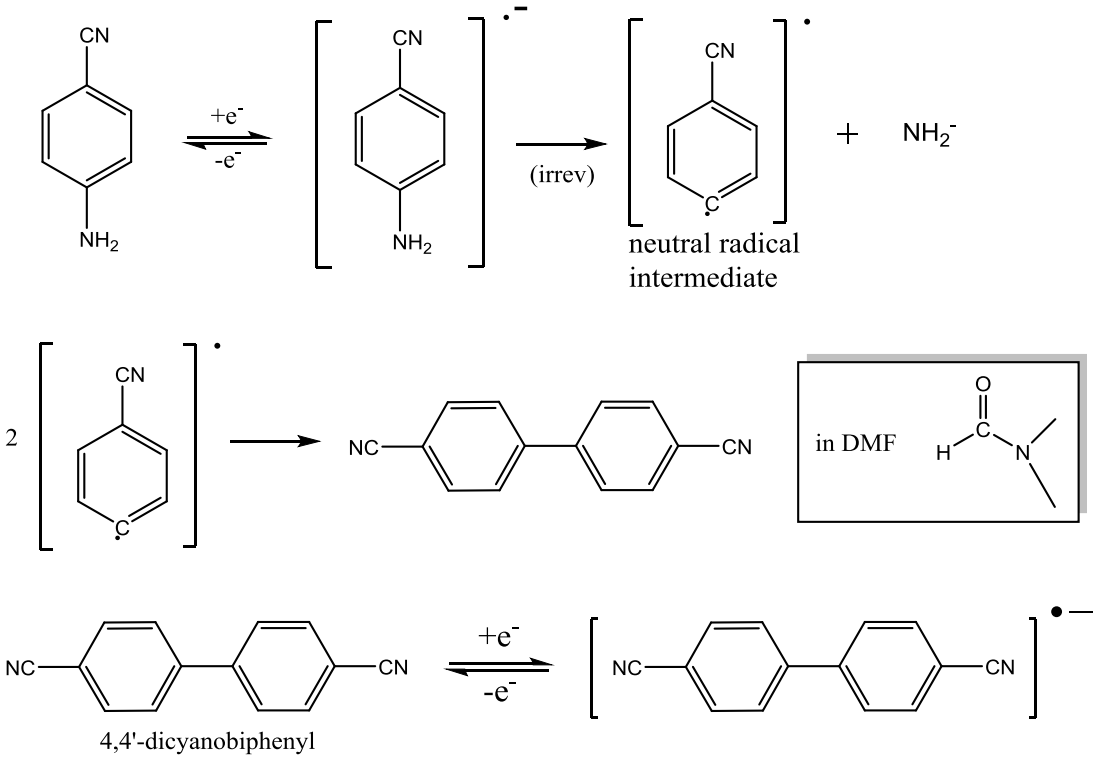

Scheme 3.1. Reduction of aminobenzonitrile in DMF and determination of the corresponding reaction mechanism by EC-EPR technique. (Modified from ref. [20])

The example at hand highlights the fact that processes involving follow-up reactions can be difficult to characterize by relying on EC alone, especially when additional factors such as solvent properties or selective adsorption complicate the electrochemical experiment or obscure the analysis of the data. With EPR, some of the processes can be interrogated and correlation with EC data can lead to more complete understanding of the system. None the less, it should be noted that the lack of EPR spectrum does not necessarily imply the absence of paramagnetic species, as in the above example no EPR spectra were observed for radical 4-aminobenzonitrile anion or its neutral radical intermediate due to the short lifetime of the species.

Furthermore, structural studies ranging from organic compounds[39-43] to organometallic[44-47] systems can be performed for the determination of electron delocalisation and structure-

function relationships between specific oxidation states of different transition metal-ligand complexes. Finally, homogeneous electron transfer reactions can be studied through the determination of line width dependency on a bulk concentration of electroactive species, which can be correlated to the Marcus theory of reaction kinetics.[36, 48-50]

3.3. Quantitative EC-EPR (QEC-EPR)

As demonstrated with the references listed above in section 3.2, QEC-EPR up to date, is mostly involved in spectral analysis and determination of g-factors and their anisotropies, hyperfine couplings, rate constants, lifetimes or line widths of radical species. Quantification involving the double integration (DI) of 1st derivative EPR spectrum signal intensity is often performed relative to analyte concentration[51], added chemical species[52], over time[53], or determining the ratio of two spectra simultaneously present in the investigated system.[54]

A deeper look into the EPR specific literature reveals that the absolute quantification of the concentration of radical species in the sample is a demanding measurement, where the nature of the interaction between the sample and the EPR spectrometer has to be understood and controlled precisely for accurate and reproducible results.[55-60] Further challenges are introduced by the dynamic nature of the electrochemistry, as discussed for example by R. N. Adams[31] as early as 1964.

Since its discovery, EPR has evolved separately from analytical sciences, and therefore the technique's analytical potential hasn't been realised, as pointed out by Nagy in 1994.[61] In quantitative EPR several variables must be accounted for, and the situation is made worse as the EPR response is further convoluted by the electrochemical cell within the resonator.

Therefore true analytical work requires that the EC-EPR setup must be carefully characterised for reliable quantitative results.

Below the general challenges related to the EC-EPR technique are discussed in more detail, and the challenges related to absolute quantification are left for the Chapter 4.

3.4. Review of EC-EPR cell designs

3.4.1. Performance criteria and challenges

As pointed out for example by Bagchi et.al. an electrochemical EPR experiment is a compromise between optimizing the electrochemical and EPR performance.[62] This work is one of the few making direct comments on the performance of different types of electrochemical cell designs. According to Bagchi, the issues faced when optimizing the electrochemical EPR performance include:

- Line broadening due to I>1/2 nuclei, and fast T_1 relaxation times in the case of transition metal complexes, where the latter problem can be overcome by lowering the temperature.

- Line broadening due to interaction between initial reactant and radical product, overcome by using flow through design or study under exhaustive electrolysis.

- Diffusion of redox active species between electrodes causing interference in EPR signal, especially in high resistance aprotic solvents.

- For short lived radicals, the working electrode must be large to produce high enough concentrations of radical species. Large electrodes lead to larger *iR* drops and cell time constants (Chapter 1), and can reduce the EPR response of the cavity.

- Absorption of the microwave electric field in solvents of high dielectric loss. These solvents give good electrochemical response, but are demanding for EPR.

Depending on the system under study some or all of the points above need to be considered when designing the electrochemical cell. An ideal cell would therefore be able to generate enough radical species for EPR detection and quantification, allow flow through or stationary solution experiments, cooling/freezing of the sample, enable accurate control of the WE potential and have a uniform current density at the WE surface while having a short enough electrochemical response time. Furthermore, the electrochemical cell has to account for the geometrical restrictions of the EPR resonator utilized and the mode of the microwave electric and magnetic fields. Also the cell design should be robust towards handling, and it should be convenient to change the WE whenever fouling of the WE occurs.

Problems related to electrochemistry; potential control, uniform current densities, time constants etc. could be alleviated by miniaturizing the cell by exploiting UMEs as discussed in Chapter 1. The greatest issue with UMEs is the fact that the overall current and thus the radical concentration is limited despite the increased current densities. EPR cavities generally employed will not be able to measure such a low concentrations of radical species, unless the electrolysis time is extended and the radical is sufficiently stable.

Very few publications exist to compare the different electrochemical cell designs in terms of their EPR sensitivity or electrochemical performance. This might be because very few designs are commercially available and therefore researchers develop and build customized cells to serve their individual needs. Below the most general cell designs are presented. Several of the designs have been modified and adjusted by different authors, and more comprehensive reviews of the cell designs exist in the literature.[4, 5, 62] Comments are also made towards the performance of the cells based on criteria discussed above.

Different criteria for the cell design arise in the case of absolute quantification of radical species, the topic which will be discussed in Chapter 4 under quantitative measurements and in the results section.

3.4.2. *Ex situ* cells with flow

In *ex-situ* cells the WE is located outside the EPR resonator. The very first EC-EPR experiment by Austen *et al.* was of this type, where anthracene, benzophenone and anthraquinone were reduced at mercury electrode, drawn into test tubes, chilled and then the spectra recorded.[3] The addition of flow to *ex-situ* experiments allows the study of species with shorter lifetimes, as the sample solution is transferred to the EPR resonator immediately after generation, and thus has less time to decay or go through follow up reactions. The other advantage of flow through designs is the fact that the electroactive species at the electrode are replenished and thus depletion of the reactant avoided, and that the mass transport to the WE is enhanced due to forced convection, facilitating a generation of a larger number of radical species.

- The Albery Tube Electrode Design

In a set of papers published by Albery and co-workers an annular WE, forming part of the wall of the sample tube through which the solution flowed into the resonator, was used to generate the paramagnetic species *ex-situ* and to flush them into the EPR resonator for detection.[63-66] Figure 3.2a shows a schematic of such a cell, where the WE is located just outside the resonator to minimize the time taken between the electrode generation and EPR detection of the paramagnetic species. The Ag|AgCl reference was situated upstream of the WE and a Pt gauze CE downstream, both outside of the resonator.

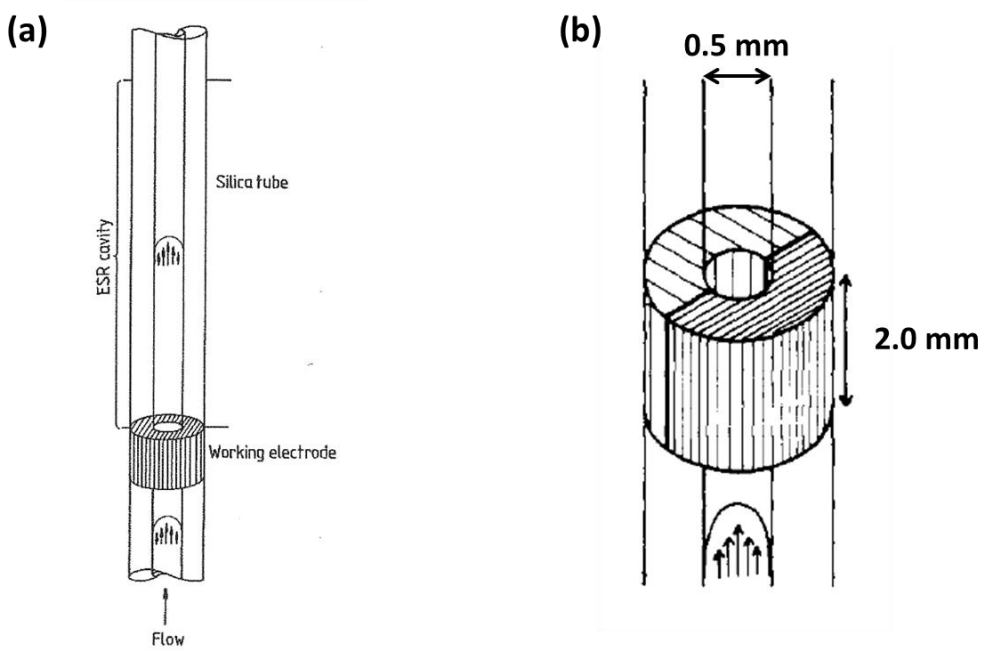

Figure 3.2. (a) The Albery tube electrode with the placement of WE with respect to the EPR cavity indicated. (b) The *in-situ* version of the cell design utilising a semi annular WE, where a section of a Pt WE (fine hatched) has been replaced with Teflon (coarse hatched). (Modified from ref [4] & [67])

Distribution of radicals within the cell was determined as a function of flow rate, electrode current and cell geometry under laminar flow conditions, allowing theories for stable radicals and those decaying with first and second order kinetics to be derived. Due to the finite distance between the leading edge of the WE and the sensitive part of the resonator, the upper limits of lifetimes for first- and second-order reactions were estimated, with rate constants of 10^2 s^{-1} and 10^4 dm^3 mol^{-1} s^{-1}, respectively.

This design has also been modified for *in-situ* work by utilising a semi annular tube electrode, as shown in Figure 3.2b, where typical diameters of the WE are 2.0 mm for the height and 0.5 mm for the inner diameter of the annulus.[67] Here the coarse hatched section represents Teflon and the fine hatched section is made of Platinum. It was shown that with semi annular electrode, placed in the region of maximum H_1 field of a TE_{102} resonator, the sin squared dependency of the H_1 field was maintained, although the

intensity diminished by a factor of two, whereas the annular electrode severely distorted the H_1 distribution of the resonator and diminished the field strength to zero at the vicinity of the WE. This was due to the fact that with an annular electrode the standing H_1 field causes eddy currents to flow along the entire circle of the electrode, whereas for a semi annular WE the eddy currents are minimised, as the current path is interrupted by non-conducting Teflon.

The disadvantages of a tubular design include the relatively large Ohmic drop due to the fact that the reference electrode is not placed between the WE and CE and the fact that the cell is not readily demountable and thus the WE cannot be easily polished when fouling occurs. Furthermore the 100 kHz modulation of the H_0 field can introduce eddy currents at the electrode making areas of it EPR insensitive.[5]

- The Wain Tube Electrode Design

An improvement to the Albery tube design was developed by Wain *et. al.*[68] and was later adapted for cryogenic studies.[69] Instead of the rectangular TE_{102} resonator used with the Albery design, a cylindrical resonator in TE_{011} mode was utilised, as for tubular cell geometry the nodal axis along the length of the TE_{011} resonator in terms of the electric field is more favourable than the nodal plane characteristic for TE_{102} resonator. Also, under similar conditions, the TE_{011} resonator has a threefold larger Q-value that the TE_{102} resonator,[70] suggesting that higher EPR sensitivities can be achievable. In terms of WE placement this cell lies between *ex situ* and *in situ*, as the resonator could be coupled with the WE inside the resonator, although the resonator coupled better when the WE was 15 mm away from the centre of the resonator, meaning that the electro generated species still

need to diffuse into the region of maximum EPR sensitivity for detection. A silver wire RE was utilised upstream of the WE, and Pt gauze CE downstream of the resonator.

The theory for diffusive and convective mass transport, and its effect on ESR response in tubular geometry was derived. Due to an inherent resistivity of the design, a 0.1 µF capacitor was placed between the RE and CE for potentiostat stability, after which the experimental results agreed with the theoretical calculations closely for electrochemical experiments when N,N,N',N'-tetramethyl-*para*-phenylenediamine (TMPD), 1,2,4,5-tetrachlorobenzoquinone (*para*-chloranil) and ferrocene in acetonitrile were used to characterise the behaviour. Also the EPR signal intensities in terms of current and flow rate agreed with the theory, suggesting that at least for stable radicals and organic solvents the cell can be used to gain analytical data of electrochemical systems.

The cell design was later used for a mechanistic study of *para*-haloanilines in acetonitrile.[71] Although the experimental results didn't match any single reaction mechanism, a presence of radical dimer was suggested, and that the dimerization mechanism involves proton and halide ion expulsion, confirming that EPR can provide additional mechanistic data that EC alone is unable to provide.

In the original paper, EC-EPR conducted with TMPD revealed that some radical $TMPD^{+\bullet}$ was present in the cell before commencing the electrolysis, probably due to aerial oxidation. The presence of molecular oxygen could severely impair results obtained with this cell design, affecting the lifetimes or line widths of radical species.

- The Wain microfluidic cell design

Wain *et. al.* have designed two microfluidic EC-EPR cells, where the well-defined hydrodynamic behaviour of microfluidic devices was combined with high sensitivity of the

cylindrical TE_{011} resonator. The rationale of using the TE_{011} resonator, as with the Wain Tube Electrode designs discussed above, lies in the fact that the H_1 field is concentrated along the centre axis of the resonator, as shown in Figure 3.3, and thus a sample with high dielectric constant can be isolated from the electric field of the resonator by adjusting the dimensions of the channel running through the length of the resonator.

The gold film WE and RE were placed upstream, just outside of the resonator, and the CE downstream to avoid the interaction with the incident microwaves inside the resonator. The channel height was 350 µm, and the width was set to 0.5, 1.0 and 2.0 mm to find the optimal performance in terms of EC and EPR performance. The cell was tested using 1 mM TMPD in acetonitrile using 0.1 M tetra-*N*-butylammonium perchlorate (TBAP) as a supporting electrolyte. The hydrodynamic and EC performance was observed to follow theoretical calculations for 1.0 and 2.0 mm channel widths, whereas the behaviour for the 0.5 mm width deviated from expectations, probably due to increasing Ohmic drop because of the narrower channel. The EC-EPR performance for the wider 1.0 and 2.0 mm cells, when normalised for the current, followed that predicted by theory, except for the slowest flow rates utilised (ca. 0.2×10^{-3} cm^3 s^{-1}), whereas for the 0.5 mm cell the behaviour deviated considerably. S:N calculations suggested that the 1.0 mm channel width will give the best

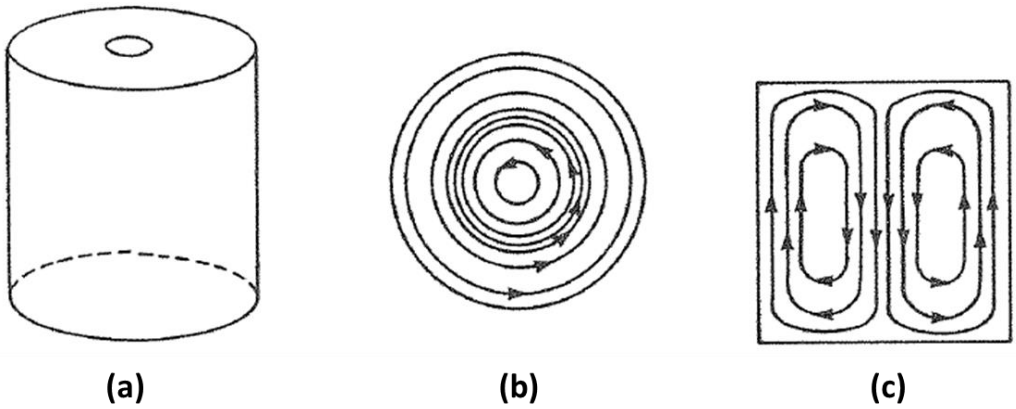

Figure 3.3. Cylindrical TE_{011} mode resonator. a) Cavity geometry, b) Electric field contours, as observed from above of the resonator, c) Magnetic field contours, as observed from the side of the resonator. (Modified from ref. [70])

performance in terms of sensitivity, EC and EC-EPR performance.[72]

As a two-stage photolithographic method was used to manufacture the cells, it is not clear if the WE can be polished between experimental runs, possibly making the design disposable once any fouling of the WE occurs. The EC-EPR sensitivity results from different cell dimensions were compared by normalising the EPR signal with respect to a secondary standard (Mn^{2+} dispersed in MgO) permanently present inside the resonator to account for the different Q-values. The problem with this approach is that although the difference in Q-values can be accounted for, it will not deal with the "lens" or "suck-in" effects due to the real part of the dielectric constant, as discussed in Chapter 4, potentially introducing an additional source of error, as the H_1 amplitude over the sample can vary from one geometry to another.

Later the microfluidic cell design was adapted for cryogenic work by constructing a U-shaped channel, which could be used with variable temperature equipment to increase sensitivity and resolution of the spectra, but also extend the range of lifetimes of radical species investigable by EC-EPR. The experiments were conducted between temperatures of 233 and 293 K in acetonitrile and TBAP as a supporting electrolyte.[73]

Meta and *para* -iodonitrobenzene radical anions were detected at cryogenic temperatures, whereas previously only the nitrobenzene radical anion resulting from ECE mechanism for the *meta* derivative had been reported at room temperature. Similarly for the reduction of *m*-nitrobenzyl chloride, only the products of chemical and electrochemical mechanisms (*m*-nitrotoluene and *m*-nitrobenzaldehyde radical anions) had been previously detected via room temperature EC-EPR, whereas at 233 K the parent *m*-nitrobenzyl chloride radical anion spectrum was clearly visible. In addition with an increased spectral resolution for the reduction products for 1-chloroanthraquinone and crystal violet, the cell design was demonstrated to be successful in the study of otherwise short lived radical intermediates.

3.4.3. *In situ* cells with flow

Issues related to *ex situ* designs discussed above, namely that there is a finite time for the electro generated species to reach the sensitive part of the EPR resonator limiting the radical lifetimes accessible, and the fact that species are not detected at the electrode but in a bulk solution where they have time to go through homogeneous reactions, can be circumvented by placing the WE directly inside the resonator. With these *in situ* cells the delay related to species arriving to the sensitive part of the resonator is avoided, and also the electrode can be functionalised and surface processes studied with EC-EPR.[4]

- The Channel Electrode Cell

Coles & Compton have designed an *in situ* flow cell with several advantages.[74] The cell is demountable, and the use of a metal foil WE allows several materials to be used. Flow rates between 10^{-4} and 10^{-1} cm^3 s^{-1} can be utilised while laminar flow throughout the cell is achieved, the design enables photoexcitation, and Ohmic drop can be made smaller than what is typical for tube electrode design by adjusting the size of the WE. The channel width utilised is usually 6 mm, length 30 mm and the thickness 0.4 mm, making aqueous work possible with this cell. A Pt gauze electrode serves as a CE downstream of the WE, whilst saturated calomel or Ag|AgCl serve as the RE upstream of the WE, both outside of the resonator. A schematic representation of the cell is shown in Figure 3.4a, and 3.4b shows the alignment of the WE relative to the EPR cavity, where $-X_u$ and X_d are the upstream and downstream edges of the resonator, respectively, X_c is the centre of the cavity and 0 and X_e indicate the upstream and low stream edges of the WE, respectively.

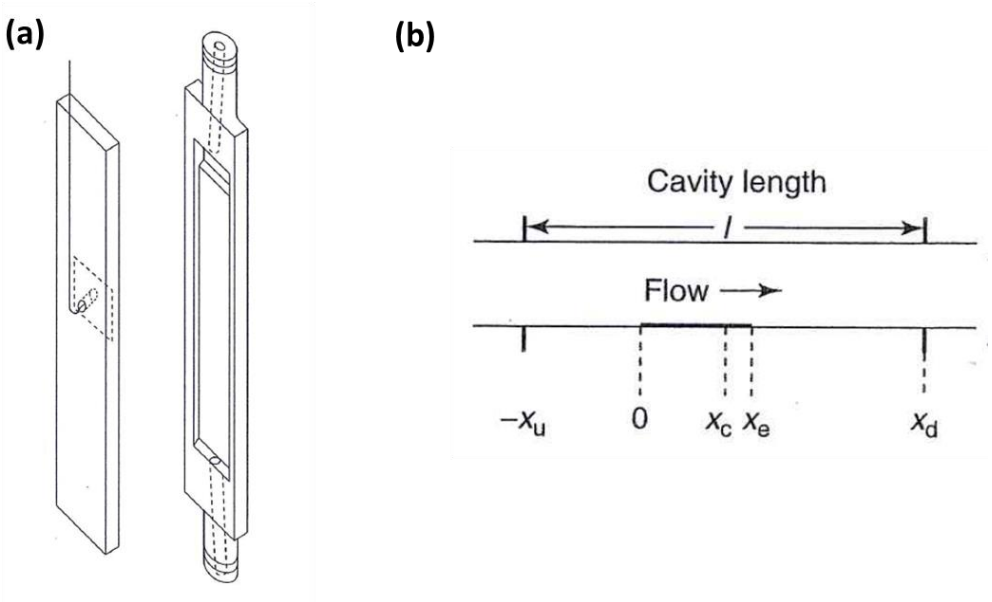

Figure 3.4. (a) the schematic representation of the channel electrode cell. (b) The alignment of the WE within the cavity with $-X_u$: the upstream edge of the resonator X_d: the downstream edge of the resonator, X_c: the centre of the cavity 0: the upstream edge of the WE and X_e: the low stream edge of the WE. (Modified from ref. [5])

The cell is used in conjunction with a TE_{102} cavity resonator having Q_u of 6400, which drops to 2500 when the cell is filled with 0.1 M aqueous electrolyte solution, and to 1200 when the WE is attached to the cell for EC-EPR experiments. This highlights the challenges related to *in-situ* experiments utilising large surface area electrodes, even when the nodal plane of the cavity is utilised, as the metal foil will interact with the incident MW field. The sensitivity of the setup is adequate for obtaining kinetic and reaction mechanism data for species with lifetimes between 10 and 100 ms.[5]

Several applications for channel electrode cell have been realised throughout the years, often in mechanistic studies[33, 75-77] for example in confirmation of ECE mechanism for bromo-anthraquinone and its diffusion coefficient,[78] comproportion reactions,[79, 80] and photo-electrochemical EPR applications where kinetics for photo-induced decomposition reactions could be measured.[81-83]

- *In situ* coaxial flow cell

Allendoerfer's coaxial cell design, discussed below in the *stationary in situ cells* -section, was adapted to EC-EPR experiments by Waller & Compton (Figure 3.5).[84] 9 mm diameter copper rod (D) was inserted into a precision-bore silica tube (G) so that an annulus of 100 to 200 µm between the two was formed depending on the solvent used, through which the solution flow was established. The rod was placed symmetrically through a TE_{011} resonator (E) so that the mercury plated Cu WE (C) insulated from the rest of the Cu rod by Teflon spacers (B), was in the middle of the resonator. Due to the copper rod, the effective volume of the resonator decreased to the extent that the resonant frequency was shifted outside of the klystron tuning range. Thus a Teflon annulus (A) was added around the silica tube to bring the resonant frequency back to the klystron range.

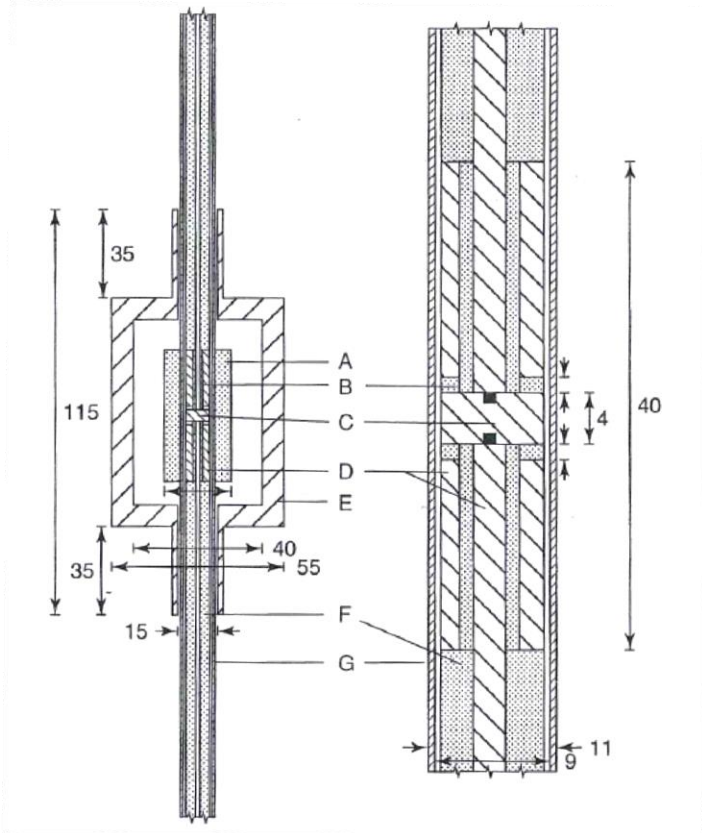

Figure 3.5. The *in situ* coaxial EC-EPR cell. A: Teflon annulus, B: Teflon spacers, C: Mercury plated Cu electrode, D: Cu rod, E: Cylindrical TE_{011} cavity, F: Teflon sheath, G: precision-bore silica tubing. The numbers represent dimensions in millimetres. (Modified from ref. [5])

The H_1 field distribution was tested by moving a crystal of a,a'-diphenyl-β-picrylhydrazyl (DPPH) across the resonator while the cell was inserted, and the intensity of the signal was observed to follow the theoretically expected sin squared relationship. As a drawback the 100 kHz field modulation was observed to cause eddy currents within the central conductor, causing the induced magnetic field to oppose the applied field and thus the sample would be subjected to different modulation amplitudes depending on the location within the cell, reducing the effective signal by one half.

The solution flow within the cell was observed to be laminar, and the cell performance closely followed the Levich and Tafel equations, indicating that the hydrodynamics of the cell were satisfactory. Also the EPR signal intensity followed that predicted theoretically, as tested by reducing fluorescein to semi-fluorescein in an alkali solution and recording the cell response.

3.4.4. Stationary *in situ* cells

The first *in-situ* experiments were performed by Geske & Maki using a two electrode setup (Figure 3.6a) placed into a cylindrical TE_{011} mode resonator, where either Pt wire or

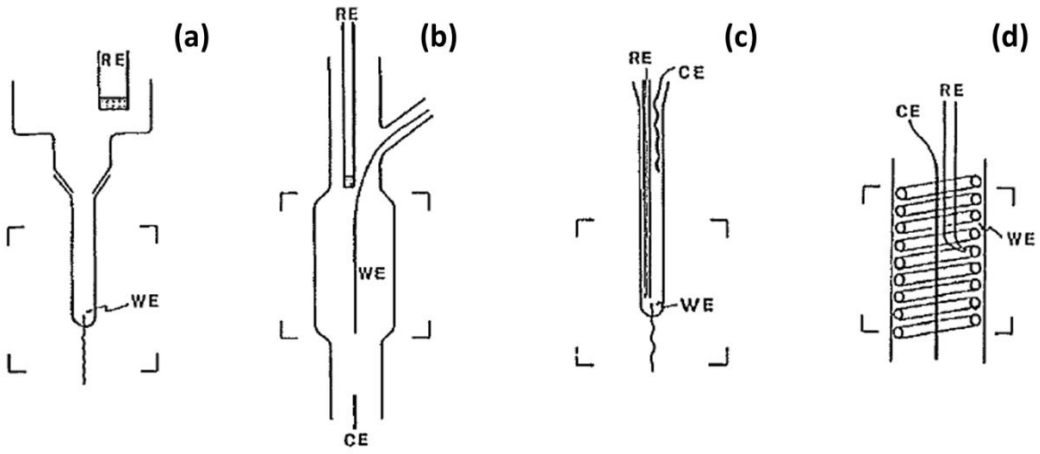

Figure 3.6. Common cell designs for in-situ stationary work. (Modified from ref. [62])

mercury pool acted as a WE and aqueous saturated calomel electrode as a RE.[1, 2, 35, 85] Due to the large currents (mA region) and high resistance solvents (20 kΩ) used, no voltammograms have been reported for this design due to large *iR* drop, and it has functioned as an electrolytic cell in oxidation and reduction processes, where hyperfine coupling constants were determined for several nitro- and dinitrobenzene compounds. Also due to the large diameter of the pyrex tube (3 mm OD) inserted to the resonator, shown by the square brackets, this cell would not allow the study of aqueous samples.

- Flat cells

A flat cell design, represented in Figure 3.6b is probably the most commonly used design in EC-EPR and are available even commercially (Wilmad Lab-Glass catalogue number WG-810-J-Q). In conjunction with cavity resonators, flat cells can be used even for aqueous studies, as the sample can be confined away from the electric fields in the resonator.[18, 37, 74, 77, 86-88] The metal wire WE in Figure 3.6b can be replaced with a foil, mesh or mercury pool, or the WE can be functionalised for example with a polymer membrane.

Electrochemical problems associated with these designs include significant *iR* drops due to the large surface area of the electrodes employed within a very narrow flat cells and large capacitive currents limiting the cell time constant, a problem further highlighted if organic solvents are used. This can introduce a potential gradient along the length of the electrode surface making the cell behaviour difficult to analyse, as the electrode reaction occurs non-uniformly along the electrode.[14, 89] A much improved potential control has been obtained by Goldberg & Bard[90], when tungsten

rods were placed along the edges of the flat cell, making the potential distribution uniform along the WE surface.

Problems in terms of EPR performance can include the deterioration of the resonator Q-factor due to large amounts of conducting metal and aqueous sample subjected to the microwave fields inside the resonator,[62] reproducible alignment of the electrochemical cell inside the resonator between experimental runs and the inhomogeneity of the H_1 field associated to cavity resonators.[31] Flat cells are also susceptible to convection during prolonged electrolysis times[18] leading to distortion of both the electrochemical and EPR performance.

The flat cell design has allowed the study of several aromatic radicals generated under cathodic and anodic potentials. Early experiments involved studying the solvent effects on the coupling constants, although correlation of the EC and EPR data also allowed determining the radical generation of *p*-phenylenediamine (PPD) to proceed via a comproportion reaction:

$$PPD^{2+} + PPD \leftrightharpoons 2\,PPD^{+\bullet}\,, \qquad (3.2)$$

which follows a two electron oxidation of the parent molecule. Also the first experiments correlating cyclic voltammetry and EPR signal amplitude were performed using flat cells, although with very limited potential control.[18, 37]

The radical decay kinetics following a current pulse was used by Goldberg *et al*. to distinguish between first order radical decomposition, second order radical dimerization and second order radical-parent addition mechanisms for several olefins. Despite the difficulties related to flat cell design, an excellent agreement for dimethyl fumarate between EPR and EC was observed, confirming the mechanism to be second order radical dimerization with a rate constant of 160 M^{-1} sec^{-1} with

standard deviation of 26 M^{-1} sec^{-1}, proving that as long as enough care is taken and the limitations of the cell design understood, accurate results can be achieved.[24, 32, 90]

Flat cells also allow the combination of EC-EPR with other spectroscopic techniques such as IR and UV-Vis, where complementary information from redox processes involving diamagnetic species can be correlated with EC and EPR data.[91-95]

- Cells based on capillary design

Various cell designs by Bagchi *et al*. attempted to overcome the issues related to potential control due to Ohmic drop effects observed with flat cells.[96-98] The use of thin wire WEs (down to 60 μm) and placing the RE right next to the WE achieved much improved potential control even for organic high resistance solvents, and variable temperature experiments could be performed. For example using CH_2Cl_2 as a solvent, the samples could be cooled to -75˚C without affecting the viscosity of the solution and thus solution state EC-EPR experiments performed.

None the less, the early designs were brittle and thus difficult to handle, and an improved design is presented in Figure 3.6c. The cell could be used with aqueous and organic solvents with a satisfactory potential control, and also flow through experiments could be performed if a drop of mercury was added to the bottom of the cell.[99] Although extremely versatile, the problem with the Bagchi cells is the small size of the WEs often employed, which makes the detection of short lived radicals challenging. Also, as small sample volumes are required, the filling factors achieved in traditional cavity resonators are not optimal for high EPR sensitivity.

A recent design, used at the UK National EPR Research Facility & Service, utilises standard quartz tubing and micro wire electrodes, and is easy and quick to assemble

and use in conjunction with a cylindrical TE_{011} cavity. The real benefit comes from the fact that the design can be used at Q and W band, i.e. at ca. 35 and 95 GHz, so that g-value anisotropies for frozen samples and dynamic parameters for solutions can be determined more accurately in addition to sensitivity gains associated to higher frequencies. Although voltammetric behaviour was not demonstrated, the cell was successfully used to study organometallic [Pt(4,4'-$(NO_2)_2$-bipy)Cl_2], biological (nitric oxide synthase reductase domain) and free radical (4-NO_2-2,2'-bipyridine) samples at temperatures between 100 and 293 K. Due to the simplicity of the design, it is by far the easiest to get acquaintance with the EC-EPR method.

- Allendoerfer's coaxial cell

In Allendoerfer's coaxial cell a standard cylindrical TE_{011} resonator is modified by placing a metallic centre conductor along the length of the resonator symmetry axis. This modification forces the node of the electric field to lie along the entire surface of the central conductor, making the volume adjacent to it the optimal place for a sample with high dielectric constant. The coaxial cell has been shown to be as sensitive as rectangular TE_{102} resonator for lossy samples, but the solid centre conductor can get heated by the 100 kHz H_{mod}, and thus the setup is not optimal for EPR measurements.[100]

In the Allendoerfer's coaxial EC-EPR cell the centre conductor was replaced by a 24 gauge gold wire helix, having 16 turns per cm and fitting snugly against the inner wall of the 6 mm id quartz test tube (Figure 3.6d), thus preventing the heating due to the AC magnetic field modulation.[19] Most importantly the metal wire helix shields the bulk of the sample inside the helix from the MW irradiation, making the cell

design ideal for lossy samples. It was estimated that the MW irradiation penetrates only ca. one radius of the wire ±10 % into the sample solution, making the Q values very high for this cell.

Also, as the surface area of the WE was ca. 22 cm^2, large amounts of radical species could be generated and thus paramagnetic species with lifetimes as short as 10^{-5} sec detected, a 5 fold improvement compared to what has been estimated for flat cells.[18] Practically unperturbed potential control was achieved by placing the CE inside the WE coil, so that the current density across the coiled WE was practically uniform, as proven by using nitrobenzene and cyclooctatetraene.[19, 101]

Allenoerfer's design has been adapted to variable temperature studies[102, 103] and also WEs of different geometries and materials have been used instead of a rather challenging helical wire.[104] The major drawbacks of the Allendoerfer design are the relatively large volumes of sample required to fill the 6 mm ID sample tube and the costs related to large WEs often constructed from noble metals.

- Allendoerfer's Loop Gap Resonator

The first and only time the LGR has been utilised in EC-EPR was by Allendoerfer, Froncisz and Hyde in 1988.[105] A 2-loop 1-gap resonator with 1 mm diameter, 5 mm height sample loop was used with a 0.25 mm diameter wire WE inside a 0.6 mm ID, 0.8 mm OD sample tube (Figure 3.7a). The effect of inserting a copper wire with 0.25 mm diameter into the active volume of the sample loop increased the microwave frequency by ca. 2 %, while introducing an insignificant change in Q factor, proving that EC-EPR experiments are feasible with LGRs. Experimental work was carried out by sealing a 0.25 mm diameter Au

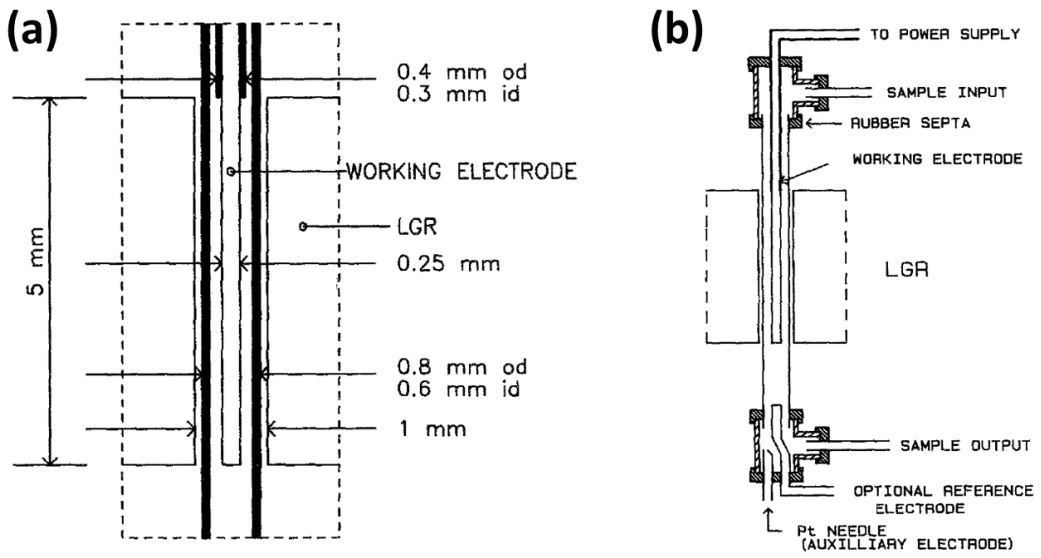

Figure 3.7. (a) dimensions of the cell relative to the LGR sensitive part. (b) Outlay of the setup showing the sample injection system and the CE. (Modified from ref. [105])

wire to a 0.3 mm ID, 0.4 mm OD precision capillary and placing the wire centrally into the sample tube.

Figure 3.7b shows the entire EC-EPR setup, where Pt syringe needle acts as a CE and an optional reference electrode can be inserted to the vicinity of the WE. Using a syringe as a means of sample delivery, stop flow experiments could be performed, although the description of the setup does not report how the sample is kept degassed during the sample injection.

Reduction of *p*-nitrobenzoic acid in water at pH 11 was used to test the system and the recorded EPR spectrum showed high sensitivity and resolution. Also the time response of the system was characterised by recording the transient EPR response as the H_0 field was fixed to the maximum intensity of the EPR spectrum. Typical currents during electrolysis were ca. 5 μA, suggesting that the potential control even for the two electrode setup should not suffer greatly from Ohmic drop effects, although the voltammetric behaviour was not specifically demonstrated.

The benefits of the system when compared to traditional flat cell designs were due to the small size of the LGR allowing an efficient miniaturization of the electrochemical cell and thus small currents diminishing the Ohmic drop, small sample volumes (order of μL) required, and 50 to 100 times improved performance in terms of absolute sensitivity. In terms of concentration sensitivity the LGR cell design performed similar to flat cell design in a rectangular cavity resonator.

References

1. A. H. Maki and D. H. Geske, *J. Chem. Phys.*, 1959, **30**, 1356-1357.
2. D. H. Geske and A. H. Maki, *J. Am. Chem. Soc.*, 1960, **82**, 2671-2676.
3. D. E. G. Austen, P. H. Given, D. J. E. Ingram and M. E. Peover, *Nature*, 1958, **182**, 1784-1786.
4. A. M. Waller and R. G. Compton, in *Comprehensive Chemical Kinetics*, ed. R. G. Compton, Elsevier, 1989, vol. 29, pp. 297-352.
5. J. D. Wadhawan and R. G. Compton, in *Encyclopedia of Electrochemistry*, eds. A. J. Bard, M. Stratmann and E. J. Calvo, Wiley-VCH Verlag GmbH & Co. KGaA, 2003, vol. 2, pp. 170-220.
6. A. Enzo, S. Daff, M. Elliot, E. Lengo, L. A. Jack, K. G. Macnamara, J. M. Pratt and L. J. Yellowlees, in *Trends in Molecular Electrochemistry*, eds. A. J. L. Pombeiro and C. Amatore, Marcel Dekker, 2004, pp. 366-381.
7. P. R. Murray and L. J. Yellowlees, in *Spectroelectrochemistry*, The Royal Society of Chemistry, 2008, pp. 207-231.
8. W. Kaim and J. Fiedler, *Chem. Soc. Rev.*, 2009, **38**, 3373-3382.
9. L. Dunsch, *J. Solid State Electrochem.*, 2011, **15**, 1631-1646.
10. F. I. Adam, P. L. Bounds, R. Kissner and W. H. Koppenol, *Chem. Res. Toxicol.*, 2015, **28**, 604-614.
11. F. M. Ferroni, J. Marangon, N. I. Neuman, J. C. Cristaldi, S. M. Brambilla, S. A. Guerrero, M. G. Rivas, A. C. Rizzi and C. D. Brondino, *J. Biol. Inorg. Chem.*, 2014, **19**, 913-921.
12. G. Macellaro, M. C. Baratto, A. Piscitelli, C. Pezzella, F. F. de Biani, A. Palmese, F. Piumi, E. Record, R. Basosi and G. Sannia, *Appl. Microbiol. Biotechnol.*, 2014, **98**, 4949-4961.
13. G. Berggren, N. Duraffourg, M. Sahlin and B.-M. Sjoberg, *J. Biol. Chem.*, 2014, **289**, 31940-31949.
14. I. B. Goldberg and T. M. McKinney, in *Laboratory techniques in electroanalytical chemistry*, eds. P. T. Kissinger and W. R. Heineman, Dekker, New York, 1984, pp. 675-728.
15. A. Streitwieser Jr., in *Molecular Orbital Theory for Organic Chemists*, John Wiley & Sons. Inc., New York, London, 1961, pp. 173-188.
16. P. R. Murray, D. Collison, S. Daff, N. Austin, R. Edge, B. W. Flynn, L. Jack, F. Leroux, E. J. L. McInnes, A. F. Murray, D. Sells, T. Stevenson, J. Wolowska and L. J. Yellowlees, *J. Magn.Res.*, 2011, **213**, 206-209.
17. D. A. Fiedler, M. Koppenol and A. M. Bond, *J. Electrochem. Soc.*, 1995, **142**, 862-867.
18. L. H. Piette, P. Ludwig and R. N. Adams, *Anal. Chem.*, 1962, **34**, 916-921.
19. R. D. Allendoerfer, *J. Am. Chem. Soc.*, 1975, **97**, 218-219.
20. P. H. Rieger, I. Bernal, W. H. Reinmuth and G. K. Fraenkel, *J. Am. Chem. Soc.*, 1963, **85**, 683-693.
21. R. D. Webster, A. M. Bond and T. Schmidt, *J. Chem. Soc. Perkin Trans. 2*, 1995, 1365-1374.
22. P. Rapta and L. Dunsch, *J. Electroanal. Chem.*, 2001, **507**, 287-292.
23. G. Mengoli, G. Farnia and E. Vianello, *Eur. Polym. J.*, 1969, **5**, 61-69.
24. I. B. Goldberg, D. Boyd, R. Hirasawa and A. J. Bard, *J. Phys. Chem.*, 1974, **78**, 295-299.
25. T. Nagaoka, S. Okazaki, T. Itoh and T. Fujinaga, *J. Electroanal. Chem.*, 1981, **127**, 289-295.

26. F. C. Laman, C. L. Gardner and D. T. Fouchard, *J. Phys. Chem.*, 1982, **86**, 3130-3134.
27. G. L. McIntire, H. N. Blount, H. J. Stronks, R. V. Shetty and E. G. Janzen, *J. Phys. Chem.*, 1980, **84**, 916-921.
28. A. Heinzel, R. Holze, C. H. Hamann and J. K. Blum, *Electrochim. Acta*, 1989, **34**, 657-661.
29. B. Marselli, J. Garcia-Gomez, P. A. Michaud, M. A. Rodrigo and C. Comninellis, *J. Electrochem. Soc.*, 2003, **150**, D79-D83.
30. J. Klima, J. Volke and J. Urban, *Electrochim. Acta*, 1991, **36**, 73-77.
31. R. N. Adams, *J. Electroanal. Chem.*, 1964, **8**, 151-162.
32. I. B. Goldberg and A. J. Bard, *J. Phys. Chem.*, 1974, **78**, 290-294.
33. F. Prieto, R. D. Webster, J. A. Alden, W. J. Aixill, G. A. Waller, R. G. Compton and M. Rueda, *J. Electroanal. Chem.*, 1997, **437**, 183-189.
34. A. J. Bard and L. R. Faulkner, *Electrochemical Methods: Fundamentals and Applications*, 2nd edn., JOHN WILEY & SONS, INC., 2001.
35. A. H. Maki and D. H. Geske, *J. Am. Chem. Soc.*, 1961, **83**, 1852-1860.
36. P. Ludwig and R. N. Adams, *J. Chem. Phys.*, 1962, **37**, 828-830.
37. L. H. Piette, P. Ludwig and R. N. Adams, *J. Am. Chem. Soc.*, 1962, **84**, 4212-4215.
38. T. Kitagawa, T. Layloff and R. N. Adams, *Anal. Chem.*, 1964, **36**, 925-926.
39. L. O. Wheeler, K. S. V. Santhanam and A. J. Bard, *J. Phys. Chem.*, 1967, **71**, 2223-2227.
40. L. S. Marcoux, A. Lomax and A. J. Bard, *J. Am. Chem. Soc.*, 1970, **92**, 243-250.
41. S. Sasaki, F. Murakami and M. Yoshifuji, *Organometallics*, 2006, **25**, 140-147.
42. S. Sasaki, K. Kato and M. Yoshifuji, *Bull. Chem. Soc. Jpn*, 2007, **80**, 1791-1798.
43. K. Haubner, K. Luspai, P. Rapta and L. Dunsch, *Phys. Chem. Chem. Phys.*, 2011, **13**, 13403-13409.
44. F. Baumann, W. Kaim, G. Denninger, H. J. Kummerer and J. Fiedler, *Organometallics*, 2005, **24**, 1966-1973.
45. W. Bruns, W. Kaim, E. Waldhor and M. Krejcik, *Inorg. Chem.*, 1995, **34**, 663-672.
46. I. R. Farrell, F. Hartl, S. Zalis, T. Mahabiersing and A. Vlcek, *J. Chem. Soc. Dalton Trans.*, 2000, 4323-4331.
47. M. Sieger, B. Sarkar, S. Zalis, J. Fiedler, N. Escola, F. Doctorovich, J. A. Olabe and W. Kaim, *Dalton Trans.*, 2004, 1797-1800.
48. B. A. Kowert, A. J. Bard and L. Marcoux, *J. Am. Chem. Soc.*, 1972, **94**, 5538-5550.
49. R. L. Ward and S. I. Weissman, *J. Am. Chem. Soc.*, 1957, **79**, 2086-2090.
50. R. Chang and C. S. Johnson, *J. Am. Chem. Soc.*, 1966, **88**, 2338-2339.
51. B. Kastening and B. Gostisamihelcic, *J. Electroanal. Chem.*, 1979, **100**, 801-808.
52. I. Romero, L. Dubois, M. N. Collomb, A. Deronzier, J. M. Latour and J. Pecaut, *Inorg. Chem.*, 2002, **41**, 1795-1806.
53. J. P. Holland, P. J. Barnard, D. Collison, J. R. Dilworth, R. Edge, J. C. Green and E. J. L. McInnes, *Chem. Eur. J.*, 2008, **14**, 5890-5907.
54. J. E. Sarneski, H. H. Thorp, G. W. Brudvig, R. H. Crabtree and G. K. Schulte, *J. Am. Chem. Soc.*, 1990, **112**, 7255-7260.
55. A. J. Saraceno, D. T. Fanale and N. D. Coggeshall, *Anal. Chem.*, 1961, **33**, 500-505.
56. R. L. Blakley, D. D. Henry, W. T. Morgan, W. L. Clapp, C. J. Smith and D. Barr, *Appl. Spectrosc.*, 2001, **55**, 1375-1381.
57. N. D. Yordanov, B. Mladenova and P. Petkov, *Anal. Chim. Acta*, 2002, **453**, 155-162.
58. N. D. Yordanov and B. Genova, *Anal. Chim. Acta*, 1997, **353**, 99-103.
59. I. B. Goldberg, *J. Magn. Res.*, 1978, **32**, 233-242.
60. D. P. Dalal, S. S. Eaton and G. R. Eaton, *J. Magn. Res.*, 1981, **44**, 415-428.
61. V. Nagy, *Appl. Magn. Res.*, 1994, **6**, 259-285.
62. R. N. Bagchi, A. M. Bond and F. Scholz, *Electroanal.*, 1989, **1**, 1-11.

63. W. J. Albery, A. T. Chadwick, B. A. Coles and N. A. Hampson, *J. Electroanal. Chem. Interfacial Electrochem.*, 1977, **75**, 229-239.
64. W. J. Albery, B. A. Coles and A. M. Couper, *J. Electroanal. Chem. Interfacial Electrochem.*, 1975, **65**, 901-909.
65. W. J. Albery, B. A. Coles, A. M. Couper and K. M. Garnett, *J. Chem. Soc. Chem. Commun.*, 1974, 198-199.
66. W. J. Albery, R. G. Compton, A. T. Chadwick, B. A. Coles and J. A. Lenkait, *J. Chem. Soc. Faraday Trans. 1: Phys. Chem. Condens. Phases*, 1980, **76**, 1391-1401.
67. W. J. Albery, R. G. Compton and C. C. Jones, *J. Am. Chem. Soc.*, 1984, **106**, 469-473.
68. A. J. Wain, M. Thompson, O. V. Klymenko and R. G. Compton, *Phys. Chem. Chem. Phys.*, 2004, **6**, 4018-4027.
69. A. J. Wain and R. G. Compton, *J. Electroanal. Chem.*, 2006, **587**, 203-212.
70. J. A. Weil, J. R. Bolton and J. E. Wertz, *Electron Paramagnetic Resonance: Elemental Theory and Practical Applications*, John Wiley & Sons, Inc., New York, Toronto, 1994.
71. I. Streeter, A. J. Wain, M. Thompson and R. G. Compton, *J. Phys. Chem. B*, 2005, **109**, 12636-12649.
72. A. J. Wain, R. G. Compton, R. Le Roux, S. Matthews, K. Yunus and A. C. Fisher, *J. Phys. Chem. B*, 2006, **110**, 26040-26044.
73. A. J. Wain, R. G. Compton, R. Le Roux, S. Matthews and A. C. Fisher, *Anal. Chem.*, 2007, **79**, 1865-1873.
74. B. A. Coles and R. G. Compton, *J. Electroanal. Chem.*, 1983, **144**, 87-98.
75. A. M. Waller, R. J. Northing and R. G. Compton, *J. Chem. Soc. Farad. Trans.*, 1990, **86**, 335-339.
76. R. G. Compton, B. A. Coles and M. J. Day, *J. Electroanal. Chem. Interfacial Electrochem.*, 1986, **200**, 205-215.
77. R. G. Compton, P. J. Daly, P. R. Unwin and A. M. Waller, *J. Electroanal. Chem.*, 1985, **191**, 15-29.
78. R. D. Webster, R. A. W. Dryfe, J. C. Eklund, C.-W. Lee and R. G. Compton, *J. Electroanal. Chem.*, 1996, **402**, 167-174.
79. R. G. Compton, B. A. Coles and R. A. Spackman, *J. Phys. Chem.*, 1991, **95**, 4741-4748.
80. C.-W. Lee, J. C. Eklund, R. A. W. Dryfe and R. G. Compton, *Bull. Korean Chem. Soc.*, 1996, **17**, 162-167.
81. R. G. Compton, B. A. Coles and M. B. G. Pilkington, *J. Chem. Soc., Farad. Trans.1: Phys. Chem. Condens. Phases*, 1988, **84**, 4347-4357.
82. R. G. Compton, B. A. Coles, M. B. G. Pilkington and D. Bethell, *J. Chem. Soc., Farad. Trans.*, 1990, **86**, 663-670.
83. R. G. Compton, B. A. Coles, G. M. Stearn and A. M. Waller, *J. Chem. Soc. Farad. Trans. 1: Phys. Chem. Condens. Phases*, 1988, **84**, 2357-2367.
84. R. G. Compton and A. M. Waller, *J. Electroanal. Chem.*, 1985, **195**, 289-297.
85. A. H. Maki and D. H. Geske, *J. Chem. Phys.*, 1960, **33**, 825-832.
86. H. Park, M. S. Won, C. Cheong and Y. B. Shim, *Electroanal.*, 2002, **14**, 1501-1507.
87. E. Dmitrieva, Y. Harima and L. Dunsch, *J. Phys. Chem. B*, 2009, **113**, 16131-16141.
88. J. G. Gaudiello, P. K. Ghosh and A. J. Bard, *J. Am. Chem. Soc.*, 1985, **107**, 3027-3032.
89. I. B. Goldberg, A. J. Bard and S. W. Feldberg, *J. Phys. Chem.*, 1972, **76**, 2550-2559.
90. I. B. Goldberg and A. J. Bard, *J. Phys. Chem.*, 1971, **75**, 3281-3290.
91. K. Haubner, J. Tarábek, F. Ziegs, V. Lukeš, E. Jaehne and L. Dunsch, *J. Phys. Chem. A*, 2010, **114**, 11545-11551.
92. A. Neudeck, A. Petr and L. Dunsch, *Synth. Met.*, 1999, **107**, 143-158.
93. A. Petr, L. Dunsch and A. Neudeck, *J. Electroanal. Chem.*, 1996, **412**, 153-158.

94. P. Rapta, A. Neudeck, A. Petr and L. Dunsch, *J. Chem. Soc.-Faraday Trans.*, 1998, **94**, 3625-3630.
95. A. Neudeck and L. Kress, *J. Electroanal. Chem.*, 1997, **437**, 141-156.
96. R. N. Bagchi, A. M. Bond, G. Brain, R. Colton, T. L. E. Henderson and J. E. Kevekordes, *Organometallics*, 1984, **3**, 4-9.
97. R. N. Bagchi, A. M. Bond and R. Colton, *J. Electroanal. Chem.*, 1986, **199**, 297-309.
98. R. N. Bagchi, A. M. Bond, C. L. Heggie, T. L. Henderson, E. Mocellin and R. A. Seikel, *Inorg. Chem.*, 1983, **22**, 3007-3012.
99. R. N. Bagchi, A. M. Bond and F. Scholz, *J. Electroanal. Chem.*, 1988, **252**, 259-267.
100. R. D. Allendoerfer and J. B. Carroll, *J. Magn. Res.*, 1980, **37**, 497-508.
101. R. D. Allendoerfer, G. A. Martinchek and S. Bruckenstein, *Anal. Chem.*, 1975, **47**, 890-894.
102. F. Gerson, H. Ohyanishiguchi and C. Wydler, *Angew. Chem.-Int. Edit. Engl.*, 1976, **15**, 552-553.
103. H. Ohya-Nishiguchi, *Bull. Chem. Soc. Jpn.*, 1979, **52**, 2064-2068.
104. L. Zhuang and J. Lu, *Rev. Sci. Instrum.*, 2000, **71**, 4242-4248.
105. R. D. Allendoerfer, W. Froncisz, C. C. Felix and J. S. Hyde, *J. Magn. Reson.*, 1988, **76**, 100-105.

Chapter 4 - Quantitative EPR (Q-EPR)

The need to determine the absolute number of radical species within a sample arises when it is not enough simply to confirm the presence of paramagnetic species or to identify them. Questions answered by Q-EPR include: How much free radicals are generated during certain industrial process? How old is an archaeological artefact? How does the spin state of a metal complex vary as a function of temperature? Q-EPR can also be used to measure drug molecules in body fluids and to estimate the shelf life of foods and beverages. The benefits of EPR include the applicability to samples that are opaque or possess scattering properties, which do not allow the use of optical techniques as a means of quantification. Also compared to gravimetric or elemental analysis methods, where separation techniques such as chromatography must be employed before quantitative work can even begin, with EPR this is often avoided as the technique is sensitive to paramagnetic species only.[1, 2]

The aim of this chapter is to walk through the challenges of determining the absolute number of paramagnetic species within a sample in EPR. The ultimate goal is to be able to count the number of radical species generated at the WE during electrochemical reactions, and the chapter finishes with electrochemistry specific challenges related to Q-EPR.

In Chapter 2.9 it was highlighted that the quantification of paramagnetic species can be extremely complicated due to several sample, resonator and spectrometer related parameters, upon which the sensitivity is also dependent. For quantitative work the equation to optimise in CW EPR is:

$$V = \chi''\eta Q_L\sqrt{P_0 Z_0}\,, \tag{4.1}$$

where V is the signal voltage at the end of the transmission line connected to the resonator, χ'' is the magnetic susceptibility of the sample and Z_0 is the characteristic impedance of the transmission line.[2] For the purposes of quantitative EC-EPR (QEC-EPR) Z_0 can be omitted from discussion, as the properties of the transmission line remain the same for all measurements.

The measured peak to peak CW EPR signal to noise ratio depends on a number of spectrometer acquisition parameters such as H_{mod}, H_1, T, acquisition time, no. of scans, filter time constant, correct tuning of the spectrometer etc., and the $\sqrt{P}$ relationship only holds in the absence of MW power saturation. These challenges, and the ultimate challenge of quantification of paramagnetic species originating from electrode reactions, are discussed below.

4.1. The magnetic susceptibility

Steady state solutions to the Bloch equations for the *in-phase* (χ') and *out-of-phase* (χ'') components of the dynamic magnetic susceptibility are:[3]

$$\chi' = \chi^0 \frac{\omega_H(\omega_H - \omega){T_2}^2}{1 + (\omega_H - \omega)^2 {T_2}^2 + {\gamma_e}^2 {H_1}^2 T_1 T_2}, \tag{4.2}$$

$$\chi'' = \chi^0 \frac{\omega_H {T_2}^2}{1 + (\omega_H - \omega)^2 {T_2}^2 + {\gamma_e}^2 {H_1}^2 T_1 T_2}, \tag{4.3}$$

where ω is the angular frequency and ω_H is the resonant frequency of the EPR transition. χ^0 is the static magnetic susceptibility:

$$\chi^0 = \frac{\mu_0 N_V g^2 {\mu_B}^2}{4 k_B T}, \qquad (4.4)$$

where N_V is the sample's spin volume density. χ' gives rise to the dispersion signal, and χ'' to the absorption signal referred to in Equation 4.1. Dispersion and absorption signals are 90° out of phase with each other, and a correctly tuned spectrometer only detects χ''. [4-6]

In Equation 4.3 the H_1 containing term in the denominator should be kept insignificant $\left({\gamma_e}^2 {H_1}^2 T_1 T_2 << 1\right)$ compared to other terms by utilising low enough P_0 so that no power saturation occurs. From the Equations 4.3 and 4.4 it is obvious that χ'' is proportional to N_V/T indicating that one should maximise the number of spins within the resonator and minimise the temperature. For quantification against an external standard, as discussed below, the temperature between the unknown and the reference must be as similar as possible.

4.2. Quantification methods

The quantification of an unknown sample can be performed in several ways, depending on the species involved and the desired accuracy and precision of the results.[7]

1. For relative concentrations in intra-laboratory work - if the measurement conditions and spectrometer settings are exactly the same between samples and the samples do not differ in their properties - a simple comparison of the 1st derivative signal amplitudes can be sufficient. Due to the sources of EPR errors discussed below this method should never be used in absolute quantification. For long measuring times a secondary reference sample can be placed permanently to the resonator to normalise the first derivative amplitudes against instrumental instabilities.

2. For undistorted spectra where the hyperfine couplings are well resolved, the product of (1st derivative signal height)*(line width)^2 can be compared to a sample with known concentration to get an estimation of the spin concentration. Unlike the first method, this method accounts for the variation in linewidths but not in the line shape and thus one should be cautious when using this approximation.

3. The number of spins can be calculated from first principles by relating the double integrated signal intensity to spectrometer, sample and experimental parameters.

4. For quantitative measurements of the spin concentration, the double integrated signal intensity can be compared to that of a reference standard either simultaneously or consecutively.

Method 1 is a severe oversimplification, whereas method 2 only estimates the line width and ignores the spectral shape, and one should be cautious if using these methods for absolute quantification. Method 3 relies on determining several specific instrument and sample related parameters[8], and has been formulated as in Equation 2.22 in section 2.9 or:[2]

$$DI = c_r \cdot [G_R \cdot C_t \cdot n_S] \cdot \left[\frac{\sqrt{P_0} \cdot H_{mod} \cdot Q \cdot n_B \cdot S(S+1) \cdot N}{f(H_1, H_{mod})}\right], \qquad (4.5)$$

where c_r is a constant from "one time" measurement of reference standard, G_R a normalised receiver gain, C_t the conversion time, n_S number of scans, n_B a Boltzmann factor for temperature dependence, N number of spins and $f(H_1,H_{mod})$ the spatial distribution of respective fields experienced by the sample. The terms in the first square brackets are normalised spectrometer settings, the numerator in the second square brackets represents measurable parameters, and the values in denominator can be

determined for example by EPR imaging. The Equation 4.5 above is used in Bruker spin counting software, and assumes that in addition to defining all of the parameters accurately, also the properties of the sample and it's placement within the resonator are exactly the same between the calibration sample and those with unknown spin concentration. In practice the method of absolute quantification given in in Equation 2.22 in Chapter 2 is considered to be too difficult to be practical[1] and for EC-EPR the Bruker method in Equation 4.5 breaks down due to several complications discussed below.

The preferred method (4) towards the determination of the absolute spin concentration in an unknown sample is via comparing the double integrated signal intensity of the unknown sample to that of a reference, for which the concentration or the absolute number of spins is known exactly. The equation to consider is:[9, 10]

$$\frac{N_{S(X)}}{N_{S(S)}} \propto \left(\frac{g_{(S)}}{g_{(X)}}\right)^2 \cdot \frac{S_{(S)}\left(S_{(S)}+1\right)}{S_{(X)}\left(S_{(X)}+1\right)} \cdot \frac{\Delta H_{pp(X)}}{\Delta H_{pp(S)}} \cdot \frac{H_{1(X)}}{H_{1(S)}} \cdot \frac{H_{mod(S)}}{H_{mod(X)}} \cdot \left(\frac{P_{0(S)}}{P_{0(X)}}\right)^{1/2} \cdot \frac{G_{R(S)}}{G_{R(X)}}, \qquad (4.6)$$

where the bracketed subscripts S and X represent the reference standard and the unknown sample, respectively. The Equation 4.6 is far from complete, assuming for example similar Q-values, temperature, η and spectrometer parameters, which is not necessarily the case, but does demonstrate the idea of scaling all of the relevant variables between the reference standard and the unknown sample. Assumptions related to equations 4.1 and 4.6 are discussed below, which contribute to the error related to quantification and should be accounted for as accurately as possible.

4.3. Dielectric properties and resonator Q-value

As mentioned above, the determination of the absolute number of spins against an external standard such as 4-hydroxy-2,2,6,6-tetramethylpiperidin-1-oxyl (TEMPOL) requires accounting for the Q-values between the reference standard and the sample under quantification. In liquid phase EPR the selection of similar solvent is not necessarily enough, but also matrix effects need to be considered, as shown by Blackley *et. al*.[11] This is especially true in EC-EPR, as the addition of supporting electrolyte can change the dielectric properties of the sample from that expected for pure solvent.[12, 13]

For lossy samples with high dielectric constant it has been shown that the EPR signal is affected by the real (*ε'*) and imaginary (*ε''*) parts of the samples dielectric constant. The ε'' leads to power losses due to the absorption of the E_1 within the resonator by the sample and any experiment related materials inserted, and thus to lower Q-values.[4, 14-16] Figure 4.1 shows the dependency of *ε'* and *ε''* of water on microwave frequency at 25 degrees Celsius.

At around 10 GHz of X-band measurements, both *ε'* and *ε''* have to be accounted for when comparing the reference standard and the unknown sample. Thus the Q-values between the unknown sample and the reference standard must be matched exactly, or if this is

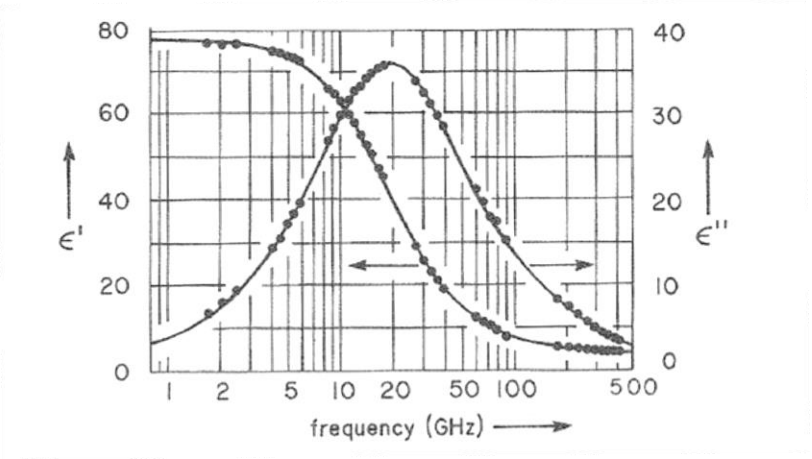

Figure 4.1. Frequency dependence of the real (ε') and imaginary (*ε''*) parts of the dielectric constant of water as a function of frequency at 25 Celsius (From ref. [15])

impossible the magnitude of Q-value must be determined exactly for both of the samples. Also, as the effect of ε'' is linear for every point within a resonator, an additional standard sample can be inserted permanently to the cavity to normalise for the changes in terms of the Q-value. Unfortunately this method does not account for the effect of ε', which is examined next.[17]

4.4. Effective filling factor

Ultimately it is the microwave H_1 field that drives the EPR transitions in the sample. The accuracy and precision of the quantitative measurements depend on the amplitude and the distribution of the H_1 field over the sample, and how precisely this can be reproduced for the reference standard. It has been suggested that errors related to H_1 field distribution over the sample is one of the largest source of uncertainty in Q-EPR.[5]

The ε' leads to redistribution of the E_1 and H_1 fields within the resonator compared to the situation when the resonator is empty. The sample's ε' introduces a "lens" or "suck in effect" which can concentrate the H_1 to the sample depending on the size, shape and the dielectric constants of the sample material. Also any accessory such as variable temperature (VT) dewar or quartz capillaries have an impact on the H_1 field distribution. For example a VT dewar is known to concentrate the H_1 field, increasing the effective filling factor from that expected solely by the volume ratio between the sample and the cavity.[5, 17]

The distribution of the H_1 along the sample axis (z) has been investigated by Yordanov *et al*. for several types of resonators, and one of the major conclusions was that the distribution of H_1 for a specific cavity has to be known before any quantitative work should be performed.[18] Furthermore, as the effect of the ε' to the EPR signal intensity can be non-linear along the sample axis, the placement and other properties of the unknown and the

reference standard, including the thickness of the sample tube walls, must be identical as possible for reliable results.[19]

The discussion above for Q, H_1 and η indicates that the sample and reference should be made exactly the same in terms of size, shape and placement inside the resonator. Furthermore solvent and matrix composition must match so that ε' and ε'' won't lead to unwanted errors in quantification. In practice for liquid samples the referencing should be done using exactly the same diameter and material capillary, positioned in exactly the same way, while matching the solvent and supporting electrolyte composition for the reference standard and the unknown.

Additional problems are introduced due to the temperature and frequency dependency of ε' and ε'', indicating that the experimental conditions have to be carefully controlled. For example a change in temperature changes the dielectric properties of the sample affecting Q-value, but also affects the critical coupling frequency of the spectrometer and the distribution of H_1 field over the sample.

4.5. Magnetic field modulation

Because CW EPR relies on phase sensitive detection through the modulation of the external magnetic field H_0, the homogeneity of H_{mod} over the sample volume is important, as its variation over the sample volume can introduce significant errors in quantitative measurements.[20] The investigation of distribution of H_{mod} for several resonator types has concluded that the combined effect of H_1 and H_{mod} inhomogeneities can result up to 150 % error.[18]

The relationship between H_{mod} and CW EPR ΔS_{pp} is shown in Figure 4.2a for Lorenzian and Gaussian lines. For Lorenzian line the ΔS_{pp} increases until H_{mod} is roughly 3 times the ΔH_{pp},

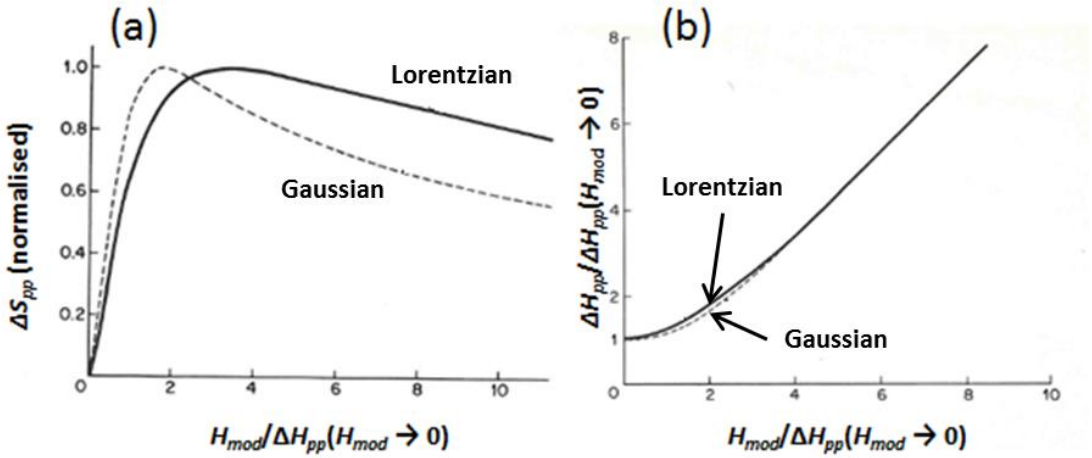

Figure 4.2. (a) Normalised peak-to-peak amplitude (ΔS_{pp}) for first derivatives of Lorenzian and Gaussian lines as a function of modulation amplitude (H_{mod}). $\Delta H_{pp}(H_{mod} \rightarrow 0)$ is the peak-to-peak separation of 1st derivative line as H_{mod} tends towards 0. (b) Relative 1st derivative line widths at increasing values of the relative modulation amplitude $H_{mod}/\Delta H_{pp}(H_{mod} \rightarrow 0)$. (Modified from ref. [26] pp. 452-453)

after which the signal starts to diminish. The implication of increasing H_{mod} is shown in Figure 4.2b, where the ΔH_{pp} is plotted against H_{mod}. For Lorenzian line, around the maximum ΔS_{pp} where the H_{mod} is three times the ΔH_{pp}, the line width is broadened by three fold also. As a rule of thumb, for a Lorenzian line, as long as the $H_{mod} < 1/3\ \Delta H_{pp}$ the line is less than 3 % broadened.[9]

It is important to note that although the ΔS_{pp} is crucial for the quantification of paramagnetic species due to its effect on S:N, it is ultimately the double integrated signal intensity (DI) that will be used as a means of quantification. DI is proportional to the modulation amplitude even when the line is slightly broadened, and thus for quantification purposes the loss of resolution due to over modulation can be justified whenever the S:N requirements demand maximization of the EPR signal.

Also v_{mod} can introduce distortion to the EPR line shapes if the frequency of the modulation approaches the frequency of the line width in Hz. For 0.03 mT ΔH_{pp}, distortion of the spectra would be observed at:

$$v_{mod} = (g\mu_B/h)\Delta H_{pp} \approx 840\ \text{kHz}\,, \qquad (4.7)$$

well above the typical modulation frequencies of 100 kHz. This distortion manifests itself as side bands in the spectrum, as the crystal detector employed is not a linear device, and its output includes the sum and difference of the microwave and modulation frequencies. At 100 kHz modulation frequency the side bands would manifest themselves at:

$$v_{mod}/\gamma_e = \ \ 3.6^{-6}\ \text{T} = 0.0036\ \text{mT}\,, \qquad (4.8)$$

away from each other, i.e. well within the line width of 0.03 mT.[9]

In more detail, Barklie et al. have investigated the dependency of ΔS_{pp} in terms of H_1 and H_{mod} amplitudes over cylindrical and point samples, noting that variation in the sample size, geometry and placement will introduce significant errors if not accounted for. The distribution of H_{mod} and H_1 were determined by a pick-up coil and a point sample of F^+ spins in MgO, respectively, and a correction factor was introduced to account for the variation of H_{mod} from the cavity centre.[21]

While deriving a correction factor for a TE_{102} cavity in terms of sample size, shape and position Nagy *et al*. observed that purely theoretical calculations for the correction factor yielded unsatisfactory results, and thus a semi-empirical approach was adopted. It was also highlighted that the numerical results obtained should not be used for other cavity resonators, but the correction factor must be obtained individually for each resonator. Also it was highlighted that the correction factor only works for non-lossy solid samples, where the sample or the sample holder do not introduce significant perturbation of the microwave field, a situation not applicable for EC-EPR cells and lossy samples.[22]

4.6. Microwave power

As discussed in Section 2.5, when a crystal detector is operating in the linear region, the EPR signal amplitude is proportional to $P_0^{1/2}$. As saturation occurs, the spin-lattice relaxation rate is not sufficiently rapid and cannot maintain the spin system at a thermal equilibrium, and the population difference between the spin states diminishes. This leads to reduced microwave absorption, which initially causes the signal amplitude to deviate from linear behaviour, and ultimately leads to a reduced signal as shown in Figure 4.3 below.

The Figure 4.3 inset displays an ensemble of electron spins in a magnetic field showing spin population levels $n_{-1/2}$ and $n_{+1/2}$, where A and E arrows show the absorption and emission processes in the presence of microwave irradiation, respectively. In Figure 4.3 inset (a), the system is initially in thermal equilibrium with the lattice, the absorption is more efficient than emission, and spin populations have their equilibrium value. Figure 4.3 inset (b) displays equal spin populations under saturation, when microwave power is too large and spin-lattice relaxation rate is not fast enough. Figure 4.3 inset (c) displays equilibrium situation required for quantitative EPR measurements after the incident power is lowered to the point where saturation does not occur and spin-lattice relaxation transfers energy to the molecule's environment efficiently enough to maintain the population difference despite incident microwave power.[23]

Figure 4.3 show the ideal behaviour for inhomogeneously and homogeneously broadened lines, and most systems exhibit behaviour somewhere between the two. For inhomogeneously broadened lines the EPR signal amplitude typically plateaus but won't decrease under saturation, and the line width is also less sensitive towards power.[24] To avoid unnecessary line broadening and saturation while maximising S:N, one of the first tasks for an unknown sample is therefore to perform a progressive microwave power

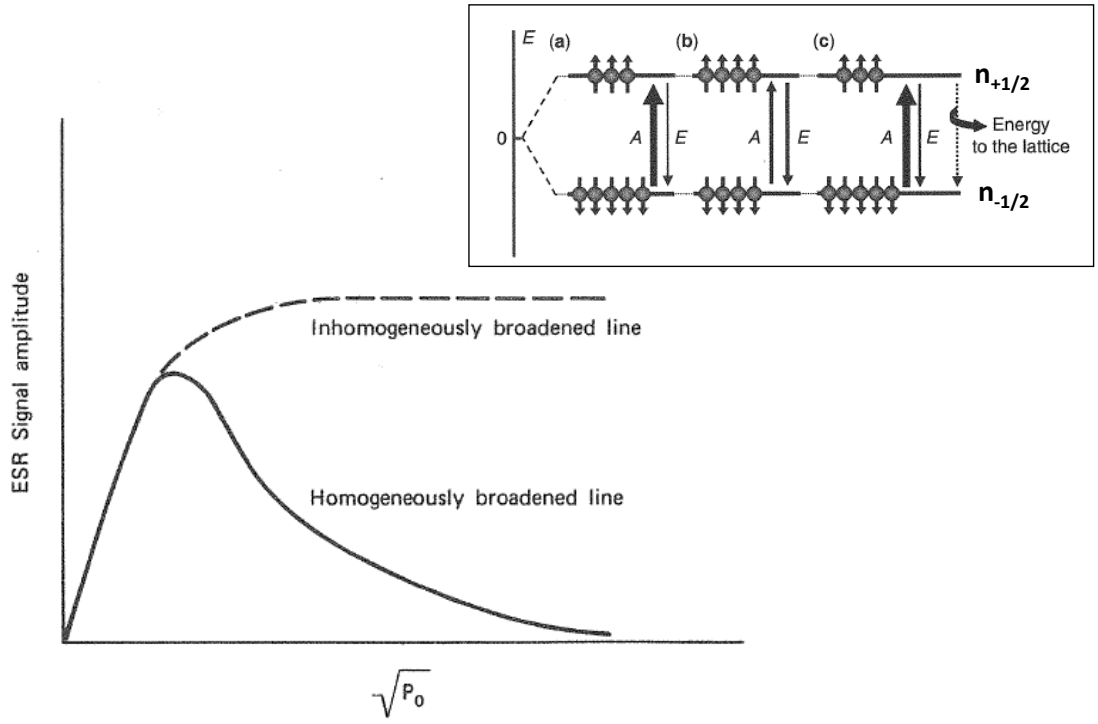

Figure 4.3. Variation of ΔS_{pp} for homogeneously and inhomogeneously broadened lines against square root of incident microwave power for ideal cases. (from ref. [24] pp. 82). Inset: An ensemble of electron spins in a magnetic field showing spin population levels $n_{-1/2}$ and $n_{+1/2}$, where the A and E arrows show the absorption and emission processes in the presence of microwave absorption. (modified ref. [23] pp. 10)

saturation study, where the EPR double integrated signal intensity is plotted against square root of the incident microwave power. A quick check for saturation is to decrease or increase the incident power by a factor of 4 (+ or - 6 dB to attenuation); due to the $P_0^{1/2}$ relationship the EPR signal should change by a factor of 2 if no saturation occurs.[2, 24]

Figure 4.4a shows DI against square root P_0 for TEMPOL radical in aqueous solution. In Figure 4.4b the EPR signal is broken into ΔS_{pp} and ΔH_{pp} components. If the aim of measurements is the quantification of absolute number of spins in the sample, the saturation curve in terms of DI is preferred method, as it accounts for possible line broadening due to P_0 in case where the area under the double integrated EPR still remains linear, thus facilitating the maximisation of S/N. If the aim is line width quantification, breaking the saturation curve to ΔS_{pp} and ΔH_{pp} guarantees that the EPR lines are not distorted due to excessive power, and the spectrum gives a true representation of the line width.[2]

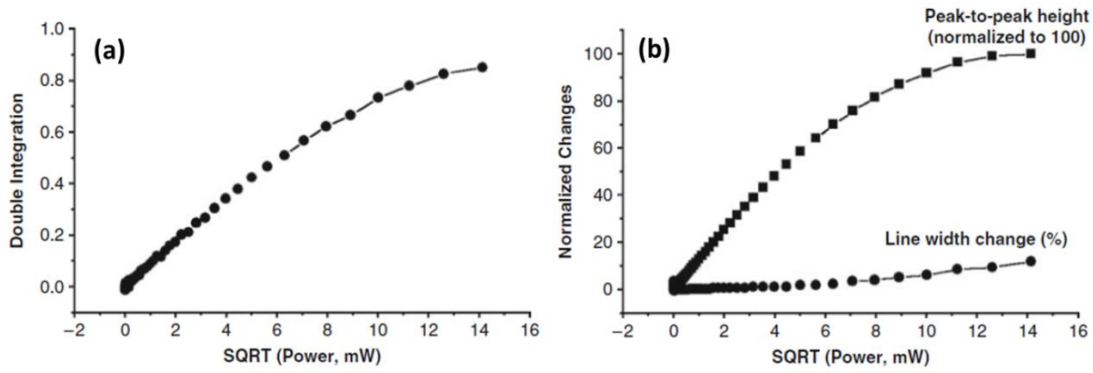

Figure 4.4. (a) The effect of incident microwave power to the double integrated signal intensity of TEMPOL radical in water using ER 4103TM cavity. (b) The effect of incident microwave power in terms of ΔS_{pp} and ΔH_{pp}. (Modified from ref. [2] pp. 117)

In QEC-EPR the size, geometry and placement of the WE inside EC-EPR cell will determine the properties of the diffusion field which contains the radical species, and this diffusion field relative to the H_1 will determine the EPR signal. Therefore the distribution of H_1 field inside the resonator with respect to the placement of the WE must also be considered for saturation behaviour, as non-reproducible WE placement can affect the results.

4.7. Scan width and double integration

As discussed above, quantitative measurements of radical concentration in a given sample require a double integration of CW-EPR signal and its comparison to that of a reference standard. Equations for normalised Lorenzian and Gaussian line shapes, encountered in EPR are:[7]

$$A(h) = \frac{A(0)}{1 + Bh^2} \quad \text{(Lorenzian)}, \tag{4.9}$$

$$A(h) = A(0)e^{-Kh^2} \quad \text{(Gaussian)}, \tag{4.10}$$

where $A(h)$ is the microwave power absorbed and h = H_0 - H_r where H_r is the value of H_0 at resonance. The intensity of absorption has its maximum value at resonance (H_0 = H_r) and approaches zero asymptotically as h increases. Especially for a Lorenzian line the wings of the absorption peak tend to infinity, which can introduce error to quantitative measurements and highlights the importance of baseline stability and S/N for wider magnetic field sweeps that must be employed.

Figure 4.5a shows the first derivative signal $D(h)$ as a function of external magnetic field h for Lorenzian line, where S is half of the experimental scan width in units of half the line width at half maximum. Integrating the derivative line from h = -∞ to h gives a true absorption curve, such as $A(h)$ *versus h in* Figure 4.5b, which will have a larger area under it than suggested by the experimental curve recorded between –S and S, indicated by the dotted line, which ignores the absorption signal in the wings of the true curve. Also the effect of an unsymmetrical experimental baseline (BL), represented by the dashed line with initial value *A*(-*S*) and slope *D*(-*S*), is shown, emphasizing the importance of recording good quality spectra that accounts for any background signals present in the resonator.

Figure 4.5c shows the double integrated signal intensity *I*(*S*) as a function of h, where the finite scan width and baseline instability decreases the observed intensity leading to errors

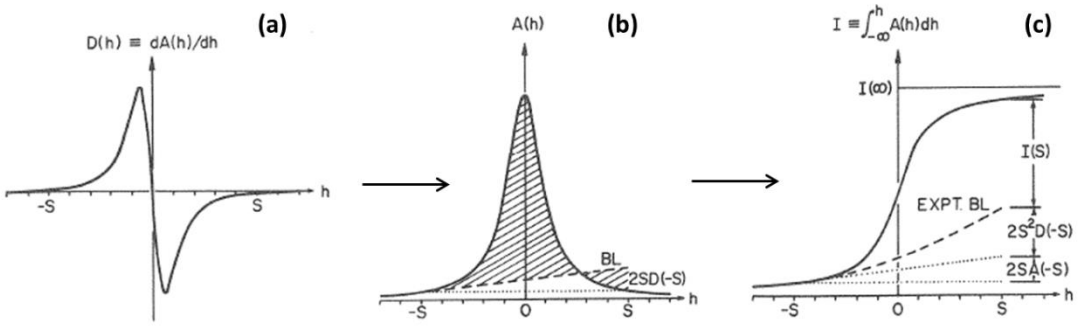

Figure 4.5. (a) the first derivative signal *D*(*h*) vs *h*. (b) The true absorption curve *A*(*h*) vs *h* integrated between ±∞ showing the effect of finite scan width (±S) and asymmetric baseline. (c) The experimental double integrated signal intensity *I*(*S*) showing the effect of finite scan width and asymmetric baseline against the true signal *I*(∞), leading to errors in quantification. (Modified from ref. [7] pp. 125)

in quantification. Figure 4.6 shows the percentage effect of finite scan width between ±S towards double integral estimation, where S is given in units of ΔH_{pp}, suggesting that the first scan point for a Lorentzian line should be recorded at least 30 times the ΔH_{pp} away from the centre of the resonance to reduce the integration error to a couple of percent. Of course further error is added by any asymmetry in the baseline. Also if overmodulation is used to enhance S/N, care must be taken when determining the required scan width, as the broadening of the line transfers more signal to the wings of the Lorentzian, thus leading to additional errors in integration over finite scan widths[7, 25]

The most important factors affecting the accuracy of the double integration are thus adequate S:N, baselining considerations and determination of the adequate scan width, which have to be accounted for with both the unknowns and the reference standards. Thus a background spectrum should be subtracted from the experimental before any numerical integration is performed, or preferably the experimental spectrum should be simulated with a corresponding Hamiltonian and then fitted to account for a baseline and finite scan width before integration. For a reliable fitting a minimum of 10 data points should be collected over the ΔH_{pp} of the narrowest EPR line.[2]

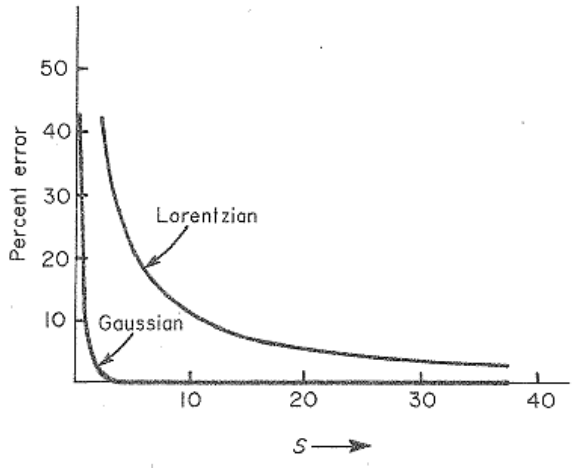

Figure 4.6. The effect of a finite scan width towards the error related to double integration for Lorentzian and Gaussian lines. (Modified from ref. [25] pp. 546)

4.8. Optimising the spectrometer settings

Some additional parameters related to the spectrometer settings required for high quality, distortion free EPR spectra are listed below.

4.8.1. Setting up phases

The biasing of the detector crystal was previously discussed in Chapter 2.5. An important aspect of quantitative measurements is the reproducible biasing of the detector to an identical current each time if consecutive measurements are to be conducted, which is always the case if several samples are to be compared to each other and to a reference standard. Also any drifts in the biasing of the detector when working with lossy solvents, or as the temperature varies, can introduce fluctuation to the measured EPR signal and thus errors to quantitative measurements. If the microwave reference arm phase is set wrong when coupling the resonator, a dispersion signal will be mixed with absorption signal, yielding reduced signal intensity.[26, 27]

An additional consideration for aqueous or lossy sample solutions is the potential mixing of χ' and χ'', leading to a shift in the frequency of the resonant cavity, yielding asymmetric 1st derivative line shapes. The resulting spectrum is thus phase shifted and due to the asymmetry the integration procedure can lead to errors in quantitative results.

Also a correct phase for the lock-in detection must be achieved. The detector phase for the 100 kHz field modulation must match that of the modulation coils and be reproducible for all of the measurements, or some of the signal intensity will be lost.[4-6]

4.8.2. Filter time constant and scan time

The filter time constant (c_t) acts as an RC filter to remove high frequency noise, thus allowing the increase in S:N in situations where the intensity of the EPR signal does not allow a reliable fitting of the data. The standard deviation of the white noise reduces as a square root of the time constant, and thus a fourfold increase in its value is needed to double the S:N. However, too large a time constant will distort the spectrum and can lead to errors in the spectral integration, and thus it is essential that this is accounted for in quantitative measurements.[24]

To determine the optimal time constant, some information about the spectrum to be recorded is required, after which Equation 4.11 can be used:[2]

$$\frac{spectrum\ width\ in\ Gauss}{line\ width\ in\ gauss} \times \frac{time\ constant\ in\ sec}{sweep\ time\ in\ sec} < 0.1\ , \qquad (4.11)$$

As the analogue to digital conversion time with the chosen resolution determine the sweep time, the time constant must be adjusted accordingly while keeping the required spectrum and line widths also in mind. The goal is to set the time constant to a value where it is ten times smaller than time taken to scan through ΔH_{pp} of the narrowest line in the spectrum, as shown by the inequality in Equation 4.11. Also the resolution should be set such that there is a minimum of 10 datapoints for the ΔH_{pp} of the narrowest line in the spectrum for reliable integration. The scan time can also be increased by averaging several scans, although for EC-EPR some additional challenges exist, which will be discussed in results section.

4.9. Referencing

Considerations above in terms of sample size, positioning etc. suggests that the sample and the reference should be measured simultaneously to match as many of the signal related variables as possible. This can be performed by using specially designed dual cavities where the sample and the reference can be inserted simultaneously provided that the spectra between the unknown and the reference do not overlap. This method ensures identical spectrometer tuning and parameter settings between the unknown and the reference[28] but does not go without problems. If the samples have different size, shape, dielectric properties or are placed in different EPR tubes, the H_1 over the sample and the reference is not uniform and errors between 10 and 20 % have been observed. For simple comparisons with proper precautions taken this error can be reduced to less than 5 %. [29, 30]

Although in some cases it is possible to use internal standards such as Mn^{2+} or K_3CrO_8,[31, 32] for electrochemical systems this does not seem suitable due to possible complications with the reference's electrochemical activity or adsorption to the WE surface. Therefore for EC-EPR the consecutive method of quantifying seems to be the most feasible, although many challenges exist.

4.10. What accuracy is achievable

EPR as a technique has traditionally suffered from a reputation of not being quantitative. This fact is highlighted by a study published in 1994, where 12 different EPR laboratories were asked to quantify the spin concentration for different types of samples.[33] The results typically varied from tens to several hundreds of percents, and up to almost four orders of magnitude in the worst case. Although a very poor agreement was observed, admittedly

the entire experimental setting was geared towards revealing the biggest problems related to Q-EPR.

The result in 1994 highlights the problems concerning the differences in procedures between laboratories, and in some cases poor understanding of the fundamentals of EPR technique. For the same sample, spectrometer and operator, two independently conducted measurements for the same sample should not deviate from each other more than ± 2%, which can be further reduced to ± 0.5 % if simultaneous reference standard is utilised.[34]

In 2008 Gancheva *et al*. used alanine dosimeters to further estimate the accuracy and reproducibility of quantitative EPR measurements.[35] After careful optimisation of spectrometer settings, an interlaboratory percentage standard deviation of 3.1 was obtained, which could potentially be further reduced if all of the spectrometers were calibrated for microwave power and modulation amplitude.

In electrochemical EPR, absolute quantification of the concentration of paramagnetic species is rarely conducted, but the error related to quantification of two cadmium complexes has been estimated to ± 15 %[36], and sometimes no details of the quantification procedure are given at all.[37] The best results available in the literature are by Dohrmann *et. al*,[38] who quantified aqueous anion radicals originating from reduction of 2-nitropropane and 2-nitro-2-methylpropane inside a flat cell using TE_{102} mode cavity resonator against electrolytically generated Cu^{2+} standard. The referencing against the Cu^{2+} was performed through different experimental runs, where the EC-EPR cell was removed from the resonator in between the experiments. The results were thus scaled by normalising against a ruby crystal permanently present inside the resonator,[39] and the error was estimated to be ± 5 % for solutions having typically ca. 10^{14} spins within the resonator.

4.11. Additional challenges due to electrochemistry

The main problems associated with QEC-EPR have been reviewed, and are discussed below,[40, 41] and explain the relatively low accuracies typically achieved.

- Reproducible EC-EPR cell placement in the resonator

If the quantification of electrogenerated species involves the removal of the EC-EPR cell from the resonator, the re-insertion will cause the tuning of the spectrometer to change, which will affect the Q-value of the resonator and thus the EPR signal intensity. This effect can be corrected to some extent by placing a secondary standard permanently in the resonator, as was done by Dohrmann *et al*. above. None the less, the external standard will not account for the "lens effect" introduced by ε' and thus there is no certainty that the H_1 field has exactly the same amplitude and distribution over the sample between the experimental runs.

- Reproducible placement of the WE

A second problem is the reproducibility in the positioning of the WE within the EC-EPR cell, if the experimental work necessitates changing of the WE for example due to fouling. If the positioning is not reproducible within the cell, the placement of the WE inside the resonator can change between experiments even if the cell was inserted in the resonator with 100 % reproducibility. As the radical species under investigation is generated at the WE, variation in its placement suggests that the species can experience different H_1 and H_{mod} fields, and the results will vary, as discussed above in sections 4.4 and 4.5.

- Inhomogeneous current density at the WE

As discussed in Chapter 1, large surface area electrodes within cells with small cross sections have a significant Ohmic drop effect associated to them. The result of this is that there exists a potential gradient across the WE surface, and the radical species are not generated uniformly at the electrode. Therefore the distribution of the radical species within the cell and thus the EPR resonator is not known exactly, and referencing against a reference standard cannot be performed reliably.

- Convection

The uneven current density at the electrode surface suggests that the diffusion field does not develop homogeneously, and thus EC-EPR cells with large Ohmic drop risk convection taking place inside the cell, especially for prolonged electrolysis times. Convection will distort the EC behaviour, making the quantification of radical species practically impossible, as the distribution of the species within the resonator cannot be defined.

- Distribution of radical species

Any EC-EPR system is highly dynamic in nature, and the distribution of the radical species limited to the diffusion field within the cell thus changes over time. This means that the effective filling factor can change over time, and that the species can diffuse out of the sensitive part of the resonator if the experimental time is long enough. Further complications arise in the case of short lived radicals, as the effective sample volume is further restricted by the finite lifetime of the species. Thus when referencing against a

stable radical such as TEMPOL, the effective distribution of the species, and its effect to the quantification process must be accounted for.

4.12. Summary

Above the most important sample related variables: χ'', η, Q, and H_1, and their significance towards Q-EPR have been discussed. All of these parameters are also temperature dependent, either directly or indirectly. For absolute quantification these parameters have to be made as similar as possible, or their values determined for rationing with an Equation such as 4.8. Also the sample material, geometry and placement within the resonator should be replicated as accurately as possible for the unknown and the reference standard.

Additional experimental parameters such as temperature, H_{mod}, P_0 also have to be considered, either by making them equal between the unknown and the reference, or scaling them. Furthermore, as quantitative work necessitates the removal and insertion of samples and references to the EPR resonator consecutively, the process of critical coupling must be reproducible so that the spectrometer response does not suffer from operator related issues.

Finally the nature of electrochemical experiments must be considered, especially as metal electrodes are required inside the resonator and polar solvents favoured in EC are somewhat incompatible with EPR, imposing fundamental challenges to EC-EPR. In addition to the technical difficulties of designing a cell and a setup that can provide quantitative results, the dynamic nature of the electrochemical systems imposes its own challenges to the process of comparing the radical species originating from the WE to the reference standard such as TEMPOL.

References

1. D. T. Burns and B. D. Flockhart, *Philos. Trans. R. Soc. Lond. Ser. A-Math. Phys. Eng. Sci.*, 1990, **333**, 37-48.
2. G. R. Eaton, S. S. Eaton, D. P. Barr and R. T. Weber, *Quantitative EPR*, Springer-Verlag, Wien, 2010.
3. J. A. Weil and J. R. Bolton, in *Electron spin Resonance: Theory and Practical Applications*, John Wiley & Sons, Inc., Hoboken, New Jersey, 2007, pp. 301-356.
4. D. P. Dalal, S. S. Eaton and G. R. Eaton, *J. Magn. Res.*, 1981, **44**, 415-428.
5. S. S. Eaton and G. R. Eaton, *Bull. Magn. Res.*, 1979, **1**, 130-138.
6. C. P. Poole Jr., in *Electron Spin Resonance*, John Wiley & Sons Inc., New York, London, Sydney, 1967, pp. 523-600.
7. M. L. Randolph, in *Biological Applications of Electron Spin Resonance*, eds. H. M. Swartz, J. R. Bolton and D. C. Borg, WILEY-INTERSCIENCE, New York, 1972, pp. 119-155.
8. C. P. Poole Jr., in *Electron Spin Resonance*, John Wiley & Sons Inc., Canada, United Kingdom, 2nd (Dover Edition) edn., 1983, pp. 400-409.
9. J. E. Wertz and J. R. Bolton, in *Electron Spin Resonance: Elementary Theory and Practical Applications*, McGraw-Hill Inc., USA, 1972, pp. 450-467.
10. N. D. Yordanov, *Appl. Magn. Res.*, 1994, **6**, 241-257.
11. R. L. Blakley, D. D. Henry, W. T. Morgan, W. L. Clapp, C. J. Smith and D. Barr, *Appl. Spectrosc.*, 2001, **55**, 1375-1381.
12. J. B. Hasted and S. H. M. El Saheb, *Trans. Faraday Soc.*, 1953, **49**, 1003-1011.
13. J. Barthel, Schmitha.F and H. Behret, *Zeitschrift Fur Physikalische Chemie-Frankfurt*, 1970, **71**, 115-131.
14. J. S. Hyde, *Rev. Sci. Instrum.*, 1972, **43**, 629-&.
15. J. A. Weil and J. R. Bolton, in *Electron Paramagnetic Resonance: Elementary Theory and Prafcical Applications*, Wiley-Interscience, Hoboken, New Jersey, 2 edn., 2007, pp. 512-536.
16. J. Barthel, K. Bachhuber, R. Buchner and H. Hetzenauer, *Chem. Phys. Lett.*, 1990, **165**, 369-373.
17. V. Nagy, *Appl. Magn. Res.*, 1994, **6**, 259-285.
18. N. D. Yordanov, B. Mladenova and P. Petkov, *Anal. Chim. Acta*, 2002, **453**, 155-162.
19. N. D. Yordanov and B. Genova, *Anal. Chim. Acta*, 1997, **353**, 99-103.
20. G. R. Eaton, S. S. Eaton, D. P. Barr and R. T. Weber, in *Quantitative EPR*, Springer-Verlag, Wien, 2010, pp. 69-78.
21. R. C. Barklie and L. Sealy, *J. Magn. Res.*, 1992, **97**, 611-615.
22. V. Nagy and J. Plaček, *Fresenius J Anal Chem*, 1992, **343**, 863-872.
23. C. Corvaja, in *Electron Paramagnetic Resonance - A Practitioner's Toolkit*, eds. M. Brustolon and E. Giamello, John Wiley & Sons, Inc., Hoboken, New Jersey, 2009, pp. 3-35.
24. J. R. Bolton, D. C. Borg and H. M. Swartz, in *Biological Applications of Electron Spin Resonance*, eds. H. M. Swartz, J. R. Bolton and D. C. Borg, Wiley-Interscience, New York, 1972, pp. 63-118.

25. J. A. Weil and J. R. Bolton, in *Electron Paramagnetic Resonance: Elementary Theory and Practical Applications*, 2 edn., 2007, pp. 537-566.
26. J. E. Wertz and J. R. Bolton, in *Electron Spin Resonance: Elementary Theory and Practical Applications*, McGraw-Hill, New York, 1972, pp. 21-37.
27. I. B. Goldberg, *J. Magn. Res.*, 1978, **32**, 233-242.
28. M. Mazúr, M. Valko, R. Klement and H. Morris, *Anal. Chim. Acta*, 1996, **333**, 249-252.
29. G. Casteleijn, J. J. TEN Bosch and J. Smidt, *J. Appl. Phys.*, 1968, **39**, 4375-4380.
30. M. Mazúr, M. Valko, H. Morris and R. Klement, *Anal. Chim. Acta*, 1996, **333**, 253-265.
31. M. Uchida and M. Ono, *J. Am. Soc. Brew. Chem.*, 1996, **54**, 198-204.
32. N. S. Dalal, M. M. Suryan and M. S. Seehra, *Anal.Chem.*, 1981, **53**, 938-940.
33. N. D. Yordanov and M. Ivanova, *Appl. Magn. Res.*, 1994, **6**, 333-340.
34. N. D. Yordanov, V. Gancheva and V. A. Pelova, *J. Radioanal. Nucl. Chem.*, 1999, **240**, 619-622.
35. V. Gancheva, N. D. Yordanov, F. Callens, G. Vanhaelewyn, J. Raffi, E. Bortolin, S. Onori, E. Malinen, E. Sagstuen, S. Fabisiak and Z. Peimel-Stuglik, *Radiat. Phys. Chem.*, 2008, **77**, 357-364.
36. M. J. Cook, I. Chambrier, G. F. White, E. Fourie and J. C. Swarts, *Dalton Trans.*, 2009, 1136-1144.
37. K. Haubner, J. Tarabek, F. Ziegs, V. Lukes, E. Jaehne and L. Dunsch, *J. Physical Chem. A*, 2010, **114**, 11545-11551.
38. J. K. Dohrmann, F. Gallusser and H. Wittchen, *Faraday Discuss. Chem. Soc.*, 1973, **56**, 330-340.
39. L. S. Singer, *J. Appl. Phys.*, 1959, **30**, 1463-1464.
40. R. N. Adams, *J. Electroanal. Chem.*, 1964, **8**, 151-162.
41. I. B. Goldberg and T. M. McKinney, in *Laboratory techniques in electroanalytical chemistry*, eds. P. T. Kissinger and W. R. Heineman, Dekker, New York, 1984, pp. 675-728.

Chapter 5 - The EC-EPR cell and the experimental setup

The first task of this project was to design and build an electrochemical cell to be utilised with 5-loop 4-gap LGR. The small size and high EPR sensitivity of the LGR enables the miniaturisation of the electrochemical cell and the use of microelectrodes, thus removing the issues related to potential control and uncertainties about uneven current densities along the WE surface, as discussed in Chapter 1.

The four gaps and four loops for the return flux (Chapter 2) of the LGR allows the increase of the diameter of the sample loop, making the sample access convenient as standard EPR sample tubes can be utilised. The radiation shield confines the microwaves to the resonator, making the coupling to the transmission line easy as the resonator can be conveniently attached to the coupling arm.

The aim was to design a system where stationary, stop flow and flow experiments could be used by utilising a syringe pump. This allows EPR signal averaging for low radical concentrations and estimation of errors related to the measurements, as standard deviations and confidence limits can be determined, making measurements analytic. Also it is essential to be able to keep the samples free from molecular oxygen and to be able to utilise both aqueous and organic solvents.

5.1. The cell material

Initial EC-EPR cell designs were made for Stereolithographic 3D printing, utilising a photosensitive resin R11. Organic solvents such as acetonitrile, acetone, dimethyl sulfoxide, tetrahydrofuran and methanol dissolved the colour off the resin, and thus the material was not feasible for EC-EPR due to contamination issues. Out of organic solvents tested, only toluene did not dissolve the resin under prolonged exposure, but due to the extremely low polarity and dielectric constant electrochemical experiments would have suffered extremely due to *iR* drop. Thus the material would have allowed only aqueous studies to be performed. The second problem with R11 was the material's fragility under mechanical stress. Due to the low *breaking strength* of the material, cells manufactured with the stereolithographic method were difficult to assemble and thus other methods of cell fabrication were explored.

As a cell material, Teflon stood out as an ideal candidate due to its chemical stability, as traditional machining methods were chosen for productions of the cell parts after failure with stereolithography. None the less, the precision of ca. 10 µm required in the cell part dimensions for a successful assembly rendered Teflon unsuitable due to its large thermal expansion coefficient. Another problem arose because of the materials chemical inertness, as attaching the cell parts, the electrode assembly and solvent tubing required the use of adhesives, which do not bind Teflon sufficiently.

Ultimately plastic polyether ether ketone (PEEK) was chosen as a cell material. It is mechanically robust, chemically inert towards organic solvents, binds easily with most adhesives and allows high precision of machining. Also, because of the material's chemical stability, any cell parts manufactured from PEEK could be re-used, as they can be soaked in acetone to dissolve off adhesives, whereas cells manufactured from R11 were ultimately of disposable type.

5.2. The cell design

5.2.1. The first generation EC-EPR cell

The original design for stereolithography is shown in Figure 5.1, where 5.1a represents the various cell parts and features within them, and 5.1b is a photograph showing the electric wires for attachment to the electrode assembly and placements of the WE and RE within the EPR tube. Parts (A) were designed to hold the EPR tubes together and allow the electric contact of electrodes to thicker wires outside the cell (blue, red and green wires in Figure 1b), whereas parts (B) allowed the connection of Teflon tubing for solvent flow through the cell via internal ducts (C). Nitrile O-rings were used (D) to seal the connection between parts A and B so that solvent could not leak out, and small channels (E) allowed the introduction of the RE and CE into the cell. The WE micro wire was inserted to the cell through central channels (F) and glued in place such that tension was holding the wire straight in the EPR sample tube.

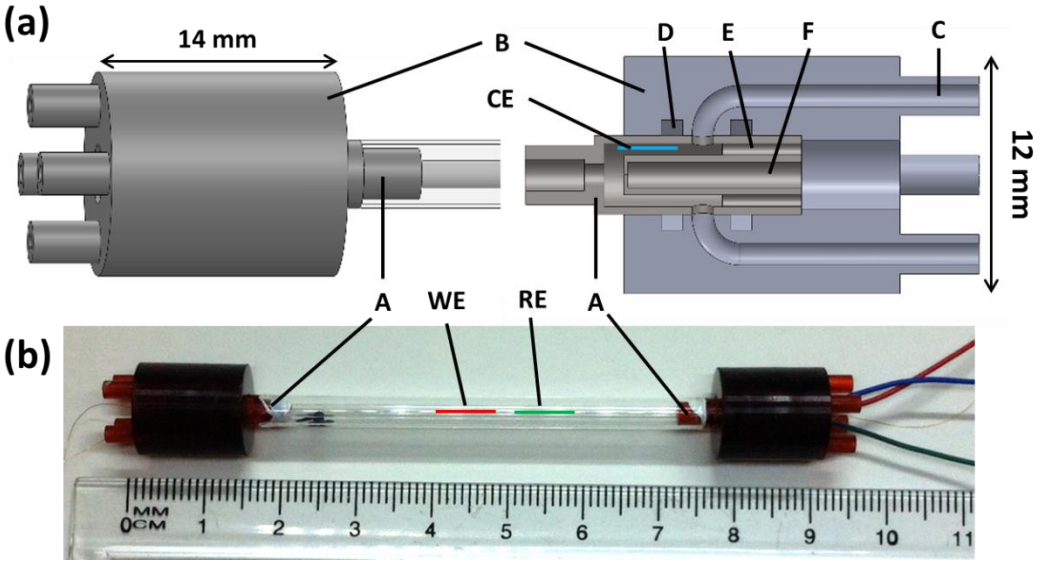

Figure 5.1. (a) a schematic representation of the 1st generation cell parts: (A) structures for holding EPR tubes and electrodes, (B) adapters for solvent flow, (C) channels for flowing the sample solution to the cell, (D) slots for O-rings to make the connection between (A) and (B) leakage proof, (E) channels to insert CE and RE to the cell, (F) central channel for inseting and attaching the WE to the cell, (CE) shows the placement of the CE. (b) A photograph of the assembled cell, with an approximate placement of the WE and RE indicated.

In practice the design was extremely difficult to assemble, as parts (A) had internal features with dimensions of the order of 100's of μm, making them brittle to handle. The parts produced through stereolitography were often non-uniform in quality, making successful fabrication of an operational cell even more challenging. For connecting the thin electrode setup to thicker electric wires outside of the cell, producing Ohmic contacts without solution leakages led to discarding of several cells even when the assembly was otherwise successful.

Ultimately several of the problems encountered with the original attempts involving stereolitoghraphy were due to the fundamental cell design, which contained too many detailed features to be practical. This combined with the inability to reuse the cell parts several times, leading to slower turnover time of cell fabrication, ultimately led to the second generation of electrochemical cells, where most of the material and design related problems were corrected.

5.2.2. The second generation EC-EPR cell

5.2.2.1. The cell design

For the second generation of EC-EPR cells the design was drastically simplified, and the main parts were machined from PEEK. All of the cell parts were designed such that only drill and laithe should be needed for the fabrication process. Figure 5.2a shows the schematic representation of the cell where parts 1, 3, 4 and 5 were machined from PEEK, and Figure 5.2b is a photograph of an assembled cell including electrode contacts to thicker wires and a Teflon tube for a sample flow.

Parts 1 and 3 support EPR test tubes, 2a: Q-band EPR tube 1.1 mm ID & 1.6 mm OD, 2b: X-band EPR tube 3.0 mm ID & 4.0 mm OD. 2a is the sample tube holding the solvent and

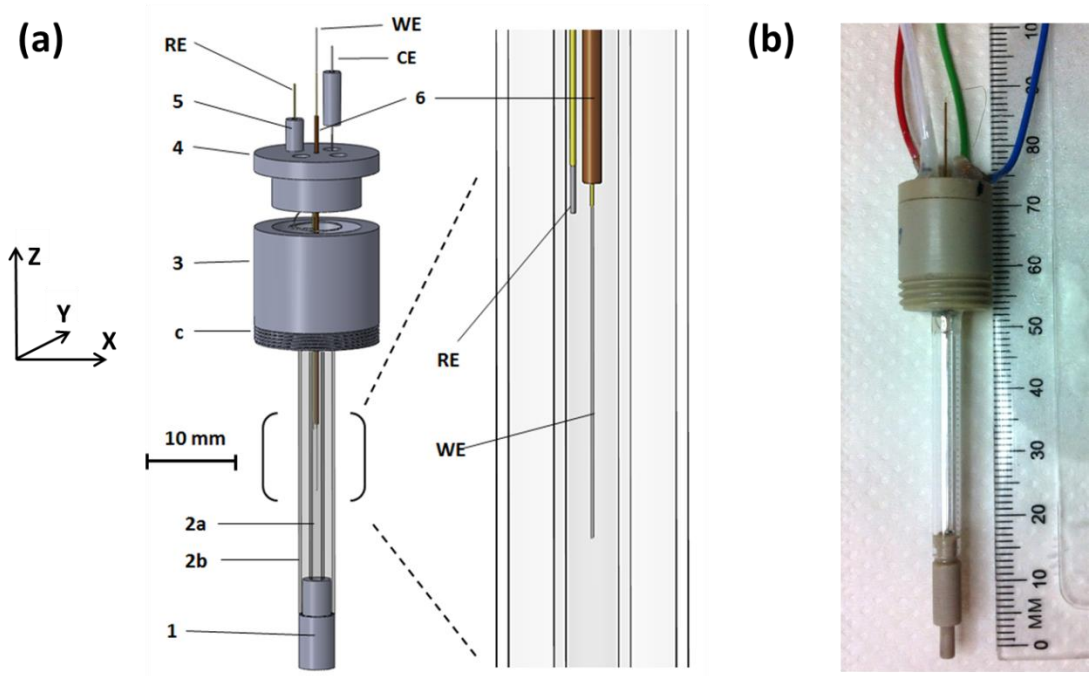

Figure 5.2. (a) The EC-EPR cell designed for a LGR. 1 & 3: capillary supports, 3c: threads to attach the cell to the resonator, 2a: Q-band EPR tube for the sample, 2b: standard X-band EPR tube for structural support, 4: adaptor for electrodes and sample flow, 5: pegs for electrode attachment, 6: capillary for inserting the working electrode (WE) to the sensitive part of the resonator, RE: reference electrode, CE: counter electrode. (b) A photograph of an assembled cell.

therefore the ID determines the sample volume inside the resonator, but also contains the WE and RE. In an assembled set up (Figure 5.3) the inner tube holds the solvent away from the fringing electric fields of the LGR gaps. Thus, if necessary, the ID of 2a can be adjusted by choosing a suitable capillary and the performance of the setup optimised for solvents with different dielectric constants. To date, cells with ID's (2a) between 0.8 and 1.1 mm have been fabricated. The X band tube (2b) acts as a structural support, making the assembled cell robust and easy to handle, while enabling symmetrical placement of the cell into the resonator.

Screw threads (c) on part 3 allow the attachment of the cell into the resonator (Figure 5.3) and also the adjustment of the WE inside the resonator in the Z-direction for optimal performance. Part 4 fits to part 3, resulting in a small chamber between them where the CE is located. The four channels in part 4 allow the attachment of Teflon tubing for solvent flow, but also permit the connection of the WE, RE and CE to thicker wires outside the cell

for electrical connection through parts 5. This arrangement makes changing the RE and CE easy if necessary, whilst the additional channel enables mixing experiments to be conducted, or insertion of a thermocouple for monitoring the sample temperature.

Part 6 is a fine capillary with dimensions of ca. 0.15 mm ID, 0.4 mm OD through which the WE is guided to the sensitive part of the LGR inside 2a. The capillary can be removed and inserted back through part 4, allowing the WE to be changed when necessary without dissembling the entire cell. The bracketed part, from where the enlarged diagram is taken, represents the sensitive region of the 5-loop 4-gap LGR used in this work and has a length of 10 mm in the Z-direction. The RE, inserted into the cell through one of the pegs (5) is placed as close as possible to the WE to minimise the uncompensated resistance. The CE in the chamber of parts 3 and 4 is far enough from the active region of the resonator so that no interference from CE products is expected.

5.2.2.2. The cell assembly

When assembled, a silicone rubber compound (RS 555-588) was used to attach various parts together whenever possible. Silicon rubber acts as a sealant, making the joints leakage proof but does not acts as an adhesive binding the parts tightly together, and thus the cell can be dissembled much easier when necessary. Ideally the only place where adhesive such as araldite is needed is to connect the thick electric wires to the parts 4 and 5 (Figure 5.2b and Figure 5.3a) to protect the connection to the micro electrode wires inside the EC-EPR cell. To achieve a low resistivity connection between the electrode wires and the thicker electric wires, silver conductive paint (RS 186-3593) was used. Silver paint was preferred over a conductive epoxy, as the electric wires come close to each other at the top of part 4, and thus it is easier to prevent the wires from short circuiting.

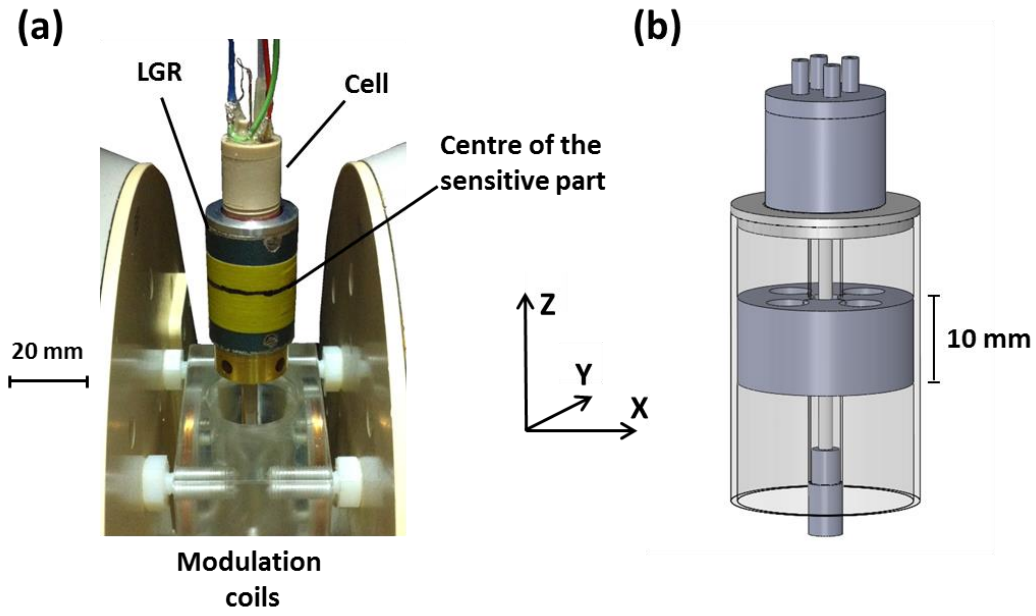

Figure 5.3. (a) Image of an assembled cell attached to the resonator. For experiments the resonator is lowered between the modulation coils. (b) A schematic representation of the cell attached to the resonator, showing the geometry of the 5 loop 4 gap resonator. The WE is located to the centre of the sensitive part of the resonator, 10 mm in height.

In the second generation design the WE is not attached from both ends anymore, as this would necessitate opening of the entire cell when the WE is changed. Instead, exposing only the tip of a metal wire and inserting it to the cell through part 6 allows the WE to be removed from the cell when fouling occurs and a new one to be inserted, making the design extremely practical. The drawback of this method is that depending on the length of the WE the tip of the wire can be leaning towards the sample tube wall, and thus the diffusion field restricted compared to a situation where the wire is placed symmetrically to the sample tube, as shown in the enlarged part of Figure 5.2a. None the less, the practicality of the design outweighs the issues related to diffusion field, and as shown in Chapter 6 the EC behaviour of the design with WE lengths of 7 mm is still acceptable.

- **Electrode wires**

WEs can be fabricated for example from polyester coated Pt, Au or Ag wires. The polyester coating can be removed by soaking the wire in saturated KOH, after which the exposed electrode is wiped with acetone and rinsed thoroughly with Milli-Q water. Cells have been fabricated successfully with WE conductor diameters of 25 and 50 µm, and for larger diameters the dimensions of part 6 (Figure 5.2a) should be adjusted accordingly. It should be noted that also a Ag mesh has been successfully used as a WE by wrapping it snugly around part 6, which allows up to 20 times larger charge generation in static solutions when compared to 7 mm long, 50 µm diameter micro cylinder. Therefore, especially if combined with signal averaging or flowing solutions to avoid depletion of the parent molecule for short lived radicals, the sensitivity of the setup could be greatly enhanced.

An ideal RE is a chloridized Ag wire with 50 or 125 µm conductor diameter in >0.1 M KCl background electrolyte, although bare Ag and Pt wires can also be used. As a CE, a bare 250 µm diameter Pt wire coiled in the chamber between parts 3 and 4 has proven to be the most reliable option.

5.2.3. The EC-EPR setup

A photograph of an assembled EC-EPR setup is shown in Figure 5.3a, and a schematic representation is displayed in Figure 5.4a. Figure 5.3b shows the geometry of the 5 loops 4 gaps LGR used in EC-EPR studies. The sensitive part height is 10 mm, while the height of the whole resonator is 35 mm and width 22.6 mm. The performance characteristics of the LGR and the setup are demonstrated in Chapter 6.

Figure 5.4b is a close up photograph of the in-house designed and built modulation coils, machined from transparent rexolite so that the resonator sensitive part can be placed to

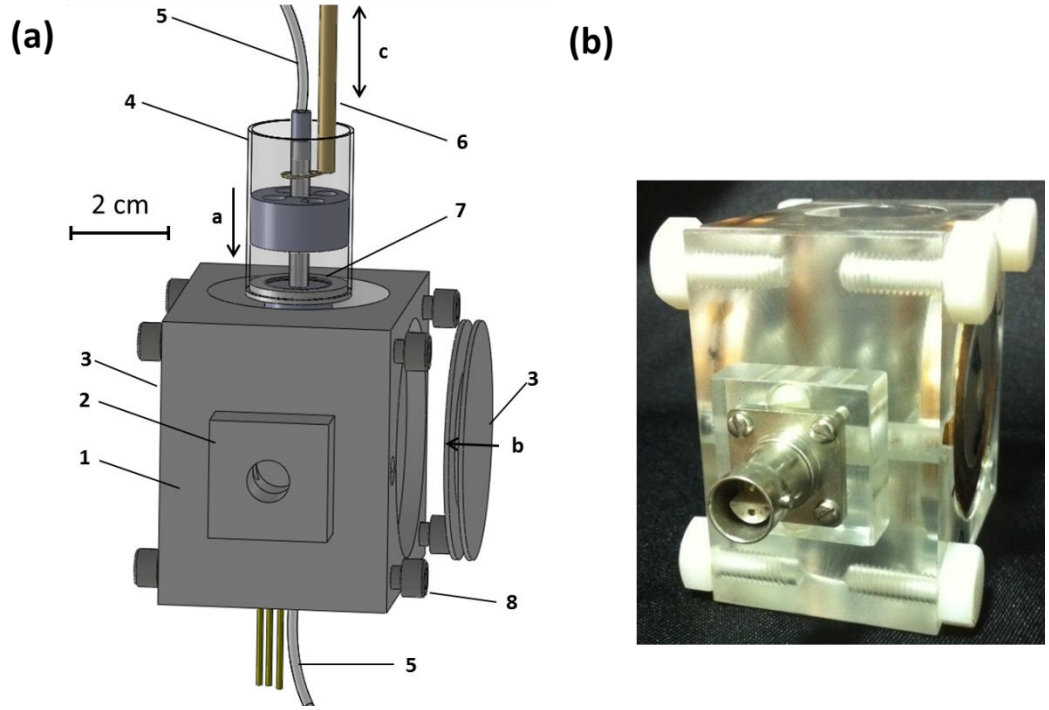

Figure 5.4. (a) A schematic representation of the setup, showing the features of the modulation system and how the coupling of microwaves to the resonator is achieved. (b) A photograph of the modulation system used to achieve the high frequency modulation of the DC magnetic field.

the middle of the coils. Modulation systems with different dimensions were designed for example to accommodate a nitrogen dewar for cryogenic work, or allowing the incorporation of fast scan coils for efficient time domain EC-EPR, but as shown in Chapter 7 the basic design can be utilised for quantitative work due to the high homogeneity of the modulation field over the sample.

In Figure 5.4a the main body of the coils (1) tighten between the EPR electromagnet's poles with screws (8). Reels (3) holding coiled copper wire are placed on both sides of the main body to provide the modulation of the DC magnetic field through BNS connection at the front of the coils (2). The LGR (4) with cell attached to it using threads (7) is lowered (a) to the central cavity of the main body, so that the sensitive part of the resonator (Figure 5.3a) is at the centre of the reels (b).

The resonator itself attaches to the coupling arm via the radiation shield (attachment not shown for clarity) and the LGR is coupled to the microwaves inductively[1, 2] through a rigid

coaxial cable with a coupling loop at the end (6). The coupling arm enables the distance between the resonator and the loop to be adjusted (c) so that a critical coupling can be achieved. A Bruker X-band continuous wave spectrometer (EMX-8/2.7) was used for the EPR measurements.

The sample is deoxygenated in a glass syringe by bubbling N_2 gas through it and introduced into the cell by a syringe pump (Legato 110) through PTFE tubing (5) surrounded by a larger PVC tubes (not shown). The interior of the PVC tubing is flushed with N_2 during the experiment and the flow guided through the whole of the central cavity of the modulation coils, thus creating an inert atmosphere around the entire EC-EPR setup, enabling high reproducibility for oxygen free experiments.

5.2.4. Benefits of the setup

The performance level of the EC-EPR cell and the setup are discussed in the following chapters. None the less, some of the general and practical benefits are commented upon here.

The possibility of changing the WE without dissembling the entire cell cannot be over emphasized, as fouling of the WE and subsequent deterioration of the EC performance is known to all experimentalists in EC. The benefits are significant especially when compared to EC-EPR cells where 3D printing or equivalent techniques have been used in conjunction with evaporating the electrodes to the cell body, thus making the exchange of the electrodes virtually impossible.

The length and thus the size of the WE can be determined within tens of micro meters with a microscope, and also the placement of the WE inside the cell in the Z-direction can be controlled within hundreds of micro meters. The positioning of the WE in the XY-plane has

also proven to be satisfactory as, depending on the sample tube diameter, the WE is centred to a region between 0.8 and 1.1 mm within the centre of the 4 mm resonator sample loop, where the H_1 field has the highest homogeneity.

Even when the setup and the cell is dissembled, parts 1 to 3 (Figure 5.2a) may remain untouched, and thus because of the threading in part 3 the cell can be re-inserted to the resonator with high precision. The threading also allows the fine tuning of the position of the WE relative to the resonator sensitive part well within 0.5 mm, thus removing the ambiguity in terms of WE and EC-EPR cell placement, the issues related to traditional EC-EPR cell designs discussed in Chapter 4.12.

The utilisation of the syringe pump allows flow, stop-flow and stationary experiments, making the signal averaging significantly straight forward and allowing detection and quantification levels inaccessible with systems relying on simple stationary work.

Also the reproducibility of degassing the samples and keeping them oxygen free during the experiments have turned out to be successful, even when fresh solution is infused with the syringe pump to the cell, proven by the TEMPOL line width experiments described in Chapter 6.

5.2.5. Practical advice

Before commencing EC or EC-EPR experiments, the WE has been cycled in the appropriate background electrolyte within the potential range for the mediator of interest, until a stable response is recorded. If several concentrations or samples are to be measured, the cell can be rinsed in between the samples and the WE cycled again in the background electrolyte to confirm that the behaviour hasn't changed from that observed initially. In the case of drastic changes the WE can be replaced with a fresh one. If quantification of species

is the aim of the experiments, a new calibration graph must be constructed every time the WE is changed or changes made to the cell/resonator assembly to account for possible discrepancy in the experimental conditions.

The problem with bare RE wires is that the metal/solution interface is more sensitive to adsorption of species during EC-EPR experiments and thus the precision and accuracy of the potential control deteriorates faster that for Ag|AgCl system. Therefore it can be justified to leave the RE some distance away from the WE, if it seems probable that species generated at the WE reach the RE surface and cause a fluctuation in the potential control. If supporting electrolytes other than KCl is used, or experiments conducted in organic solvents, a chloridized Ag wire is still a good starting point before turning into bare Ag or Pt wires, for example.

Finally it should be noted that the stereolithographic method of manufacturing the cell parts might be worth exploring, even with resin such as R11, if a simplified structures such as those for the second generation were to be produced. The machining of the cell parts by conventional methods to an acceptable precision requires a highly skilled technician and about a weeks' worth of working hours to produce parts for a single cell. Therefore, in cases where access to a high quality mechanical workshop is limited and studies are limited to aqueous systems, stereolitographic method would be a convenient way of producing cell parts in large quantities with several beneficial modifications based on the requirements of the experiment.

References

1. M. Mehdizadeh, T. K. Ishii, J. S. Hyde and W. Froncisz, *IEEE T. Microw. Theory.*, 1983, **31**, 1059-1064.
2. G. A. Rinard, R. W. Quine, S. S. Eaton and G. R. Eaton, *J. Magn. Reson. Ser. A*, 1993, **105**, 137-144.

Chapter 6 - The EPR and EC performance of the setup

The EC-EPR setup described in Chapter 5 is characterised for its EPR and EC performance. The adaptation of the setup for quantification of the concentration of paramagnetic species originating from electrode reactions is left for Chapter 7.

6.1. Matherials and methods

- **Chemicals**

Potassium chloride (BioXtra ≥99.0 %), potassium nitrate (ReagentPlus®, ≥99.0 %), paraquat dichloride (Methyl Viologen; PESTANAL®, analytical standard), tetrabutylammonium perchlorate (TBAP; Fluka, ≥99.0 %), hexaammine ruthenium (III) chloride (98 %) and 4-hydroxy-TEMPO (TEMPOL; 97 %) were purchased from Sigma-Aldrich. Milli-Q water (Millipore Corp.) (resistivity 18.2 MΩ cm, 25°C) was used for aqueous work and anhydrous acetonitrile (Sigma, 99.8 %) as an organic solvent. All chemicals were used as received. **(**Ferrocenylmethyl) trimethylammonium hexafluorophosphate ($FcTMA^+$) was prepared as described elsewhere.[1]

- Electrode wires

WEs were 50 µm diameter Pt or Ag micro-wires coated with a 7.5 µm layer of polyester (Goodfellow, ±10 % tolerance in conductor diameter). The desired length of

polyester (typically 7 mm) was removed by soaking in saturated KOH. CEs were bare Pt or Ag wires, and either bare or chloridized Ag wires of diameter 50 µm or 125 µm served as REs. Before commencing EC or EC-EPR experiments, the WE was cycled in the appropriate background electrolyte within the potential range for the mediator of interest, until a stable response was recorded. The potential was controlled through a potentiostat (CH Instruments, CHI 1140B) in a three electrode configuration.

6.2. The EPR performance

6.2.1. Degassing

When studying paramagnetic species it is crucial that the samples, whether aqueous or organic, remain oxygen free. Unwanted presence of molecular oxygen can introduce artificial line broadening as discussed with Figure 6.1, and may also act as an oxidiser especially when reduction processes are studied with electrochemistry, complicating the analysis of the EPR data.

The sensitivity of TEMPOL line width towards dissolved oxygen was used to characterise the ability of the setup to keep the samples oxygen free during EC-EPR, and the results are shown in Figure 6.1. The initial line width of 100 µM aqueous TEMPOL solution without degassing was determined to be 1.93 ±0.003 Gauss (0.193 mT). Degassing the solution before introduction to the cell and flowing N_2 through the setup, as described in Chapter 5 gave a line width of 1.83 ±0.003 Gauss, and remained at that value for ca. two hours. A slight increase in line width was observed at times beyond 2.5 hours, which turned out to be statistically significant at 0.05 level (p-value), after checking for outliers and confirming that the sample observations were normally distributed. Thus the time during which experiments can be performed in aqueous solutions is at least 2.5 hours.

At point (A) 0.3 mL of fresh TEMPOL solution was infused into the cell, after which the line width returned to ca. 1.83 Gauss, proving that the sample inside the Teflon tube remains also oxygen free and fresh aliquots of sample can be infused to the cell even during prolonged experiments. The break in the X-axis signifies turning the N_2 flow off and leaving the sample to stand inside the cell overnight. The point at time 0 after the break shows the measured line width 12 hours after point (A). Surprisingly the sample, once introduced to the cell oxygen free, remains almost oxygen free even without flowing N_2, as evident from the consecutive measurements up to 2.5 hours.

At point (B) an aliquot of 0.1 mL was infused to the cell, and the line width observed increased to 1.90 ±0.003 Gauss, showing that if the N_2 is turned off the sample in the Teflon tube does get oxygenated. Finally at point (C) a sample completely exposed to the environment was infused to the cell, and a line width of 1.95 ±0.003 Gauss was measured.

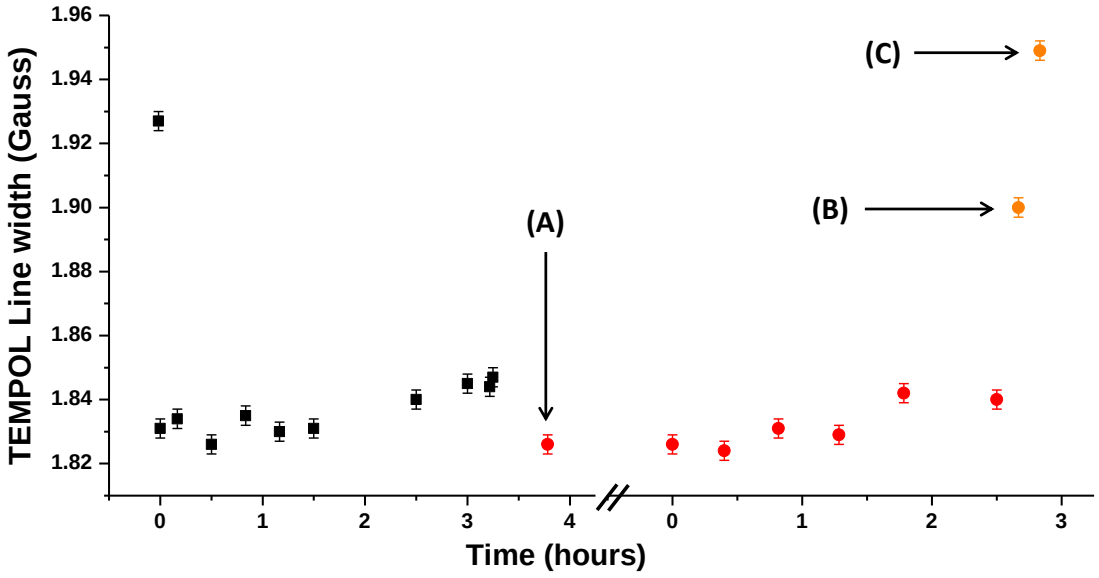

Figure 6.1. Test for keeping the samples deoxygenated. The minimum time for measurements is 2 hours, and fresh solution can be infused to the cell oxygen free (A). The sample remains oxygen free overnight even without the flow of N_2. Infusing fresh sample without the flow of N_2 shows the line broadening due to oxygen (B) and (C).

6.2.2. The effect of the sample tube ID towards the EPR performance

The larger the ID of the sample tube, the closer the sample is to the fringing electric fields in the gaps of the LGR, leading to an increasing dielectric microwave loss. The Q_u of the 5-loop 4-gap resonator is approximately 1,700 in accordance with the literature.[2] For water the 1.1 mm ID sample tube gives a typical Q_L = 500-600 at around 9.57 GHz, one third of the Q_u. If the cell is filled with acetonitrile, $Q_L \approx 900$. A cell assembled with the 0.8 mm ID sample tube filled with water gives a Q_L = 900-1000 at around 9.51 GHz frequency. It is worth noting that the filling factor for homogenously distributed radical in 0.8 mm ID sample tube is ½ of that in 1.1 mm ID sample tube, and thus in aqueous solutions scales roughly linearly with Q-value. Crucially the insertion of a micro-cylinder WE to the resonator does not introduce a noticeable change in the Q-value or the microwave coupling.

In EC-EPR experiments higher Q-values suggest higher sensitivity, as the radical is limited to the diffusion field of the EC experiment and thus the capillary ID does not necessarily determine the filling factor, which would suggest decreasing the ID of the sample tube to the smallest possible. However, eventually the diminishing ID of the tube starts to hinder the electrochemical performance (see Figure 6.6 and discussion) and a compromise between the two has to be made depending on the system under investigation.

6.2.3. EPR sensitivity comparison between LGR and cylindrical resonator

The EPR performance between the LGR and a cylindrical TE_{011} resonator was compared by placing a 1.1 mm ID capillary filled with water containing 10 μM of the stable radical TEMPOL as a reference concentrically through each resonator.

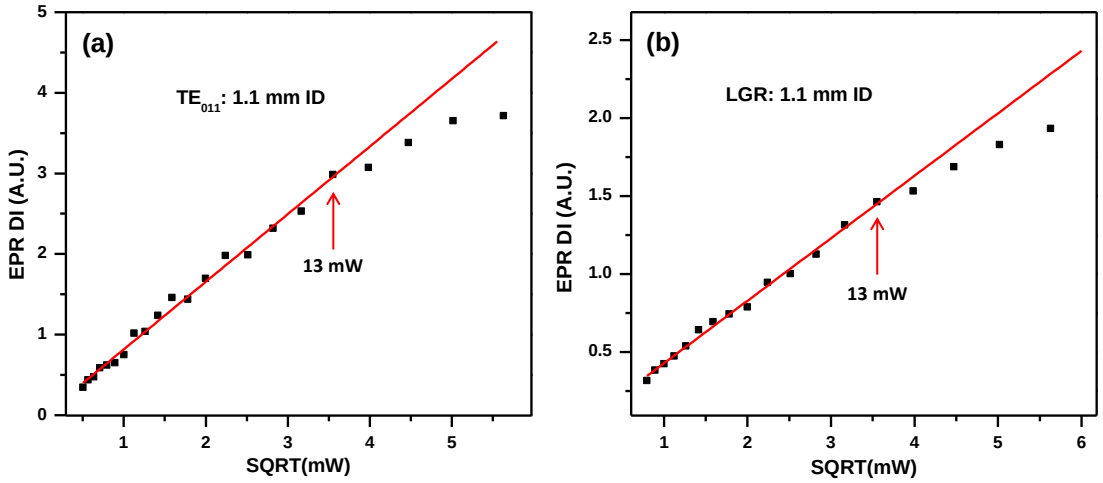

Figure 6.2. Saturation curves for aqueous 10 µM TEMPOL solution: (a) TE_{011} cylindrical resonator with 1.1 mm sample tube ID, (b) LGR with 1.1 mm sample tube ID.

The TE_{011} cavity coupled critically with a Q-value of 1,500, whereas the Q_u for this resonator was closer to 5,000, suggesting that both resonators performed at approximately 1/3 of their Q_u. Using a microwave power sweep, saturation curves for both resonators were constructed, and the results are shown in Figure 6.2.

Both the cylindrical resonator and LGR displayed saturation at powers beyond 13 mW (Figure 6.2a and b), which when accounting for the three times higher Q-value for the cylindrical resonator would suggest that the power densities obtained with this particular LGR are three fold higher due to the smaller size and larger conversion factor. The difference in physical sizes of the resonators is displayed in Figure 6.3. Using 13 mW as operating power and identical spectrometer settings, the S:N achieved for both of the resonator was approximately 120:1 (Figure 6.4), indicating that in terms of concentration sensitivity they perform equally. Note that the EPR spectrum for TE_{011} cavity in Figure 6.4 is offset for clarity. Although the two resonators performed similarly, taking into account sample volumes inside the resonator, in terms of absolute sensitivity the LGR performed 2-3 times better. In the future the η for the LGR could be further increased by reducing the diameter of the

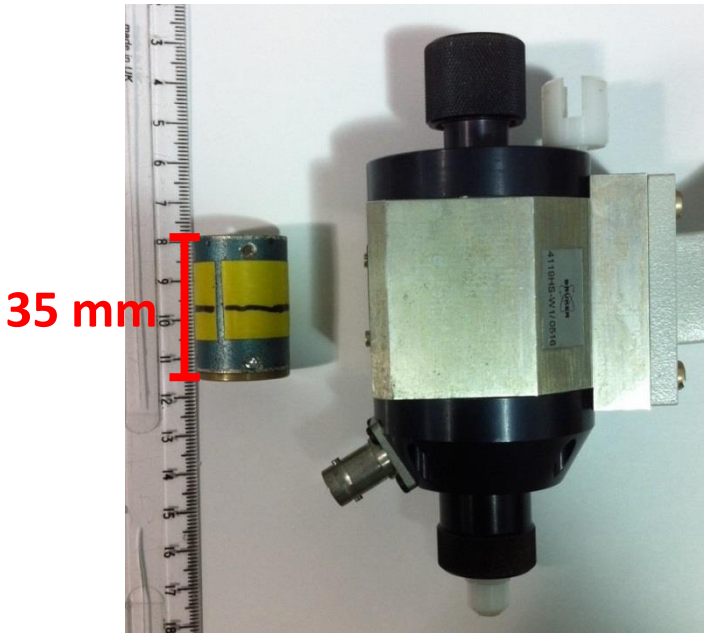

Figure 6.3. Comparison between the physical size between 5 loops 4 gaps LGR used and commercially available cylindrical TE_{011} resonator.

sample loop, and adjusting the EC-EPR cell accordingly, leading to further sensitivity gains.

TEMPOL measurements were also performed in a LGR with 0.8 mm ID sample tube with 13 mW power, and the comparison of results to 1.1 mm ID are shown in Table 6-

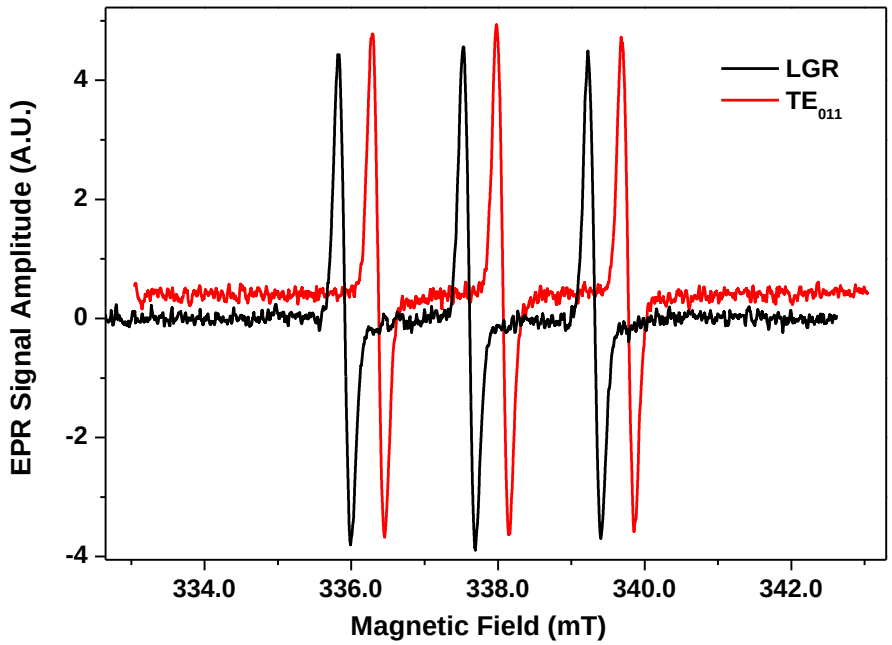

Figure 6.4. The comparison of aqueous 10 µM TEMPOL EPR spectra with S:N = 120 for TE_{011} and LGR

Table 6-1. Comparison of 1.1 mm ID and 0.8 mm ID sample tubes in LGR.

2r	Q_L	η (r^2)	ηQ_L	S:N
1.1 mm	550	1.21/4	660	120
0.8 mm	950	0.64/4	600	100

1, where the Q_L, filling factor (r^2), the product of the two and S:N values are collected. The ratio of the ηQ_L for the two resonators is 1.1, and that of the S:N values 1.2. This would indicate that the 1.1 mm sample tube would be favourable in terms of sensitivity at least in cases where the radical species is evenly distributed. None the less, as slight saturation occurred for the 0.8 mm sample tube at 13 mW, and the fact that the stability of the critical coupling is greater, the decision must ultimately be made according to the saturation properties of the sample and the electrochemical requirements, as discussed next.

6.3. The electrochemical performance

6.3.1. Finite element simulations

As discussed in Chapter 1, the theory for the diffusion of electro-active species to a micro-cylindrical electrode has been developed for linear sweep and potential step experiments. COMSOL allows the extension of the theory to CV experiments, and thus the comparison of the experimental work to simulations representing an ideal performance.

The WE placed inside a 0.8 mm ID sample tube (part 2a, Figure 5.2a, Chapter 5) was modelled using COMSOL Multiphysics 4.4 (COMSOL AB) Finite Element Modelling (FEM) software. Figure 6.5a shows a schematic representation of the model. The domain height and width are 11.2 and 0.4 mm, respectively, for the modelled 0.8 mm

ID capillary in 2D axisymmetric geometry. Therefore, the model is not shown to scale, as the height of the domain is significantly greater than the width, but distinguishes the different types of boundaries used.

Boundary 1a is the wire electrode surface where the small edge (1b) represents the tip of the wire. Boundary 2a is the wire insulation with 2b representing the insulation edge (7.5 µm) at the electrode/insulation interface. Boundary 3 represents the bulk solution in the capillary far away from the WE. Boundary 4 is the capillary wall where the concentration of the electro active species goes to zero. Corresponding boundary conditions for the model are summarised in Table 6-2.

For 100 and 20 mV/s scan rates simulated, 20,000 and 15,000 mesh points were applied along the 7 mm long wire electrode (boundary 1a), respectively, and 25 mesh points to the electrode tip (boundary 1b). The domain was then meshed continuously with a maximum element growth rate of 1.02 from the electrode surface. $FcTMA^+$ oxidation and the subsequent reduction of $FcTMA^{2+}$ under diffusion control was modelled for CV by solving Fick's second law for the concentration of reactant species (Chapter 1, Equation 1.10). The D of 6.7×10^{-6} cm^2/s and the E_0 of 0.356 V were

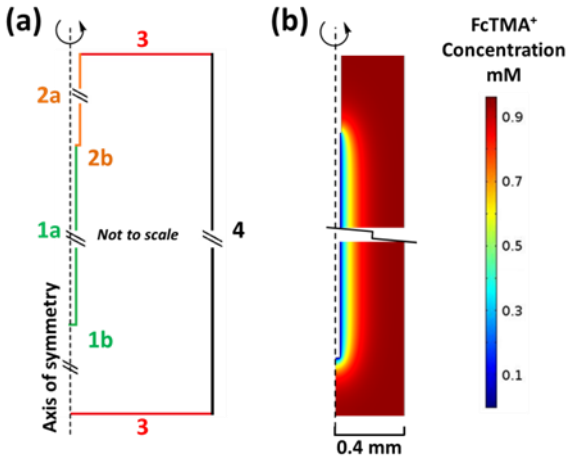

Figure 6.5. 2D axisymmetric COMSOL model. (a) Boundaries 1 a&b: WE, 2 a&b: insulation, 3: bulk concentration, 4: capillary wall. (b) A snapshot of the concentration of $FcTMA^+$ within the cell during a 20 mV/s cyclic voltammogram between 0 and 0.6 V at the switching potential for oxidation of 1 mM $FcTMA^{+/2+}$ couple at 50 µm diameter wire electrode.

Table 6-2. Boundary conditions for the finite element model for CV. C^*= 1.0 mM $FcTMA^+$, T = 294 K, n = 1, E_0 = 0.356 V, E_{appl} swept between 0.0 and 0.6 V linearly over time, $C_{0,j}$ = [$FcTMA^+$] at the electrode surface as a function of the E_{appl}, F = 96485 C mol^{-1} and R = 8.314 J mol^{-1} K^{-1}.

Boundary	Boundary type	Boundary condition
1a	Wire electrode	$C_{0,j} = (C^*\theta)/(1+\theta)$ $\theta = exp\left[\left(\frac{nF}{RT}\right)(E_0 - E_{appl})\right]$
1b	Electrode tip	
2a	Wire insulation	$n \cdot \nabla C = 0$
2b	Insulation edge	$n \cdot \nabla C = 0$
3	Bulk solution	$C = C^*$
4	Capillary wall	$n \cdot \nabla C = 0$
Axial symmetry		$n \cdot \nabla C = 0$

determined with 12.5 µm disc UME in a bulk solution of 1 mM $FcTMA^+$ in 0.4 M KCl against Ag|AgCl reference, and were used in the simulations. Nernstian behaviour (Chapter 1, Equation 1.11) during CV was modelled at boundaries 1 a&b, where the concentration of $FcTMA^+$ ($C_{0,j}$) relative to $FcTMA^{2+}$ was controlled by sweeping the applied potential (E_{appl}) between 0 and 0.6 V linearly over time.

Figure 6.5b is a snapshot of the concentration of $FcTMA^+$ in the cell during a 20 mV/s CV recorded between 0 and 0.6 V at the switching potential of 0.6 V. The figure is zoomed to the electrode/insulation interface and to the wire tip and thus boundaries 3 where $C = C^*$ lie further away than suggested by the Figure. A 0.8 mm ID sample tube was chosen for the model, as the simulations results were identical to those obtained with the wire electrode in a bulk solution, indicating that for a symmetrically placed WE, the cell wall does not hinder the diffusion field, and thus the model is expected to be representative of analytical equations in Chapter 1.

The finite element simulations allowed the prediction of an ideal EC behaviour of the cell, to which the experimental performance could be compared. Also, in the design

phase of the cell simulations aided to estimate the required diameter of the sample tube, thus avoiding unnecessary trial and error.

6.3.2. Experimental results

Experimental electrochemical characterization of two cells, representing the largest and smallest ID sample tubes used in this study, i.e. cell A (1.1 mm) and cell B (0.8 mm) are shown in Figure 6.6. The working electrode was a 50 µm diameter Pt wire, 7 mm in length, with 125 µm diameter Ag|AgCl RE and a bare Pt wire as a CE, while 0.4 M KCl acted as a supporting electrolyte. The results of the COMSOL simulation (identical for cells A and B) for the $FcTMA^{+/2+}$ are also shown.

Figure 6.6a reveals that at scan rate of 100 mV/s the EC CV behaviour for the oxidation of 1 mM $FcTMA^{+}$ is very close to that predicted by the simulation, run without utilising any fitting parameters, assuming a reversible diffusion-controlled process. From the simulated peak to peak separations a value of ΔE_P = 78 mV is predicted, which shows that diffusion is not purely linear at the micro-cylinder electrodes, as the expected ΔE_P for purely linear diffusion is 59 mV for a conventional macro electrode.[3] For cell A the experimentally recorded ΔE_p value 83 ± 2 mV is in good agreement with the theory. Note that increasing the supporting electrolyte concentration was observed to decrease the ΔE_P (due to Ohmic drop effects in the cell geometry employed) until values of ca. 0.4 M, beyond which increasing the concentration showed no appreciable effect. For the cell B measured ΔE_p value was 94 ± 2 mV, the difference to that obtained for cell A essentially due to a stretched out oxidative wave of the CV.

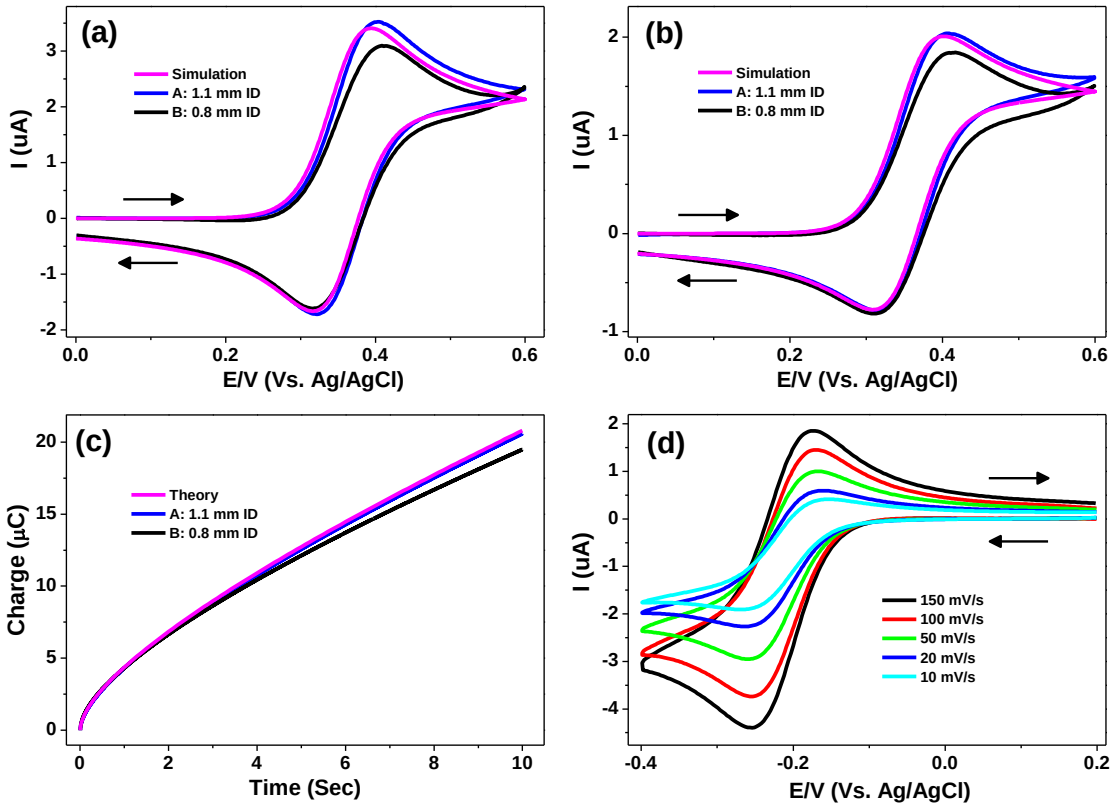

Figure 6.6. Electrochemical characterization of cells A (1.1 mm ID) and B (0.8 mm ID) in water and comparisons with simulations. (a) 1.0 mM $FcTMA^+$; CV at 100 mV/s, (b) 1.0 mM $FcTMA^+$; CV at 20 mV/s, (c) 1.0 mM $FcTMA^+$; potential step to 0.5 V for 10 seconds, (d) 1.0 mM $Ru(NH_3)_6^{3+}$ at different scan rates. All results recorded at Pt wire electrode 50 µm in diameter, 7 mm length vs. Ag|AgCl reference and 0.4 M KCl as a supporting electrolyte.

Figure 6.6b shows the behaviour at 20 mV/s scan rate, where increased radial diffusion effects will contribute. This is reflected in a larger simulated ΔE_P = 93 mV which compares favourably with 94 ± 2 mV measured for cell A. For cell B a typical experimental ΔE_P value of 104 ± 2 mV suggests that at slower scan rates the cell behaviour is closer to ideal.

For cell A, the experimental peak current (i_P) was within 3 % of the simulated irrespective of the scan rate whereas for cell B the i_P value was consistently 8 % lower. As discussed above in the simulations section, the capillary wall is not expected to hinder the diffusion field for 0.8 mm ID sample tube. A possible explanation for the slightly lower i_P and larger ΔE_P values is the fact that the WE is not completely symmetrically placed within the capillary. Thus the diffusion field might be restricted

by the capillary wall, although the observed i_P values for the cell B are still within the tolerance of the wire diameter (±10%) reported by the manufacturer.

The simulated i_P for the oxidation wave at 20 mV/s agreed with the analytical equations shown in Chapter 1 to within 0.5 %, and for 100 mV/s the agreement was to within 2 %. For the latter scan rate the number of mesh points required to approach the value predicted by the analytical equations started to increase exponentially for an incremental increase in simulated i_P.

For the potential step experiment in Figure 6.6c, the charge generated during a potential step to 0.5 V for 10 seconds was 20.6 ± 0.5 µC for cell A and 19.5 ± 0.5 µC for cell B. The amount of charge predicted by the analytical equation 1.15 presented in Chapter 1 was 20.8 µC, within 1 % of the charge generated with cell A and 7 % larger than for cell B, confirming the trend observed for potentiodynamic experiments. Cell A behaves almost exactly as predicted by the theory, whereas cell B suffers from the slightly diminished currents generated, probably due to unsymmetrical placement of the WE in the sample tube.

Figure 6.6d shows a reduction of $Ru(NH_3)_6^{3+/2+}$ couple for the cell A with 1.1 mm ID sample tube at different scan rates. The gradual change in the shape of the CV is evident, as the measured ΔE_P increases from 80 to 114 mV as the scan rate is reduced from 150 to 10 mV/s, which can be explained by the increased radial component of the diffusion at micro-cylinders as shown for $FcTMA^{+/2+}$ between 100 and 20 mV/s. In terms of reproducibility, for reversible mediators such as $Ru(NH_3)_6^{3+/2+}$ and $FcTMA^{+/2+}$, scan rates between 10 and 150 mV/s seem to be practical for the cell described.

6.4. The electrochemical EPR performance

EPR was carried out in the presence of the electrochemical redox mediator methyl viologen (MV^{2+}) which undergoes two consecutive one electron reduction steps, the first being:

$$MV^{2+} + e^{-} \rightleftharpoons MV^{+\bullet}\,, \qquad (6.1)$$

where the paramagnetic species $MV^{+\bullet}$ is formed. Previous work has shown this species to be sufficiently stable for convenient detection in EC-EPR.[4, 5] A typical CV for the reduction of 1 mM MV^{2+} in water and 0.4 M KNO_3 at a Ag wire electrode (50 µm diameter, 7 mm length) for cell A is shown in Figure 6.7, and the structure of the MV^{2+} is displayed in the inset. The ΔE_P value of 98 mV for 20 mV/s scan rate suggests essentially a reversible behaviour, as discussed for Figure 6.6b above and previously suggested by literature.[6, 7]

From the CV in Figure 6.7 a potential of -0.9 V was chosen to generate $MV^{+\bullet}$ under

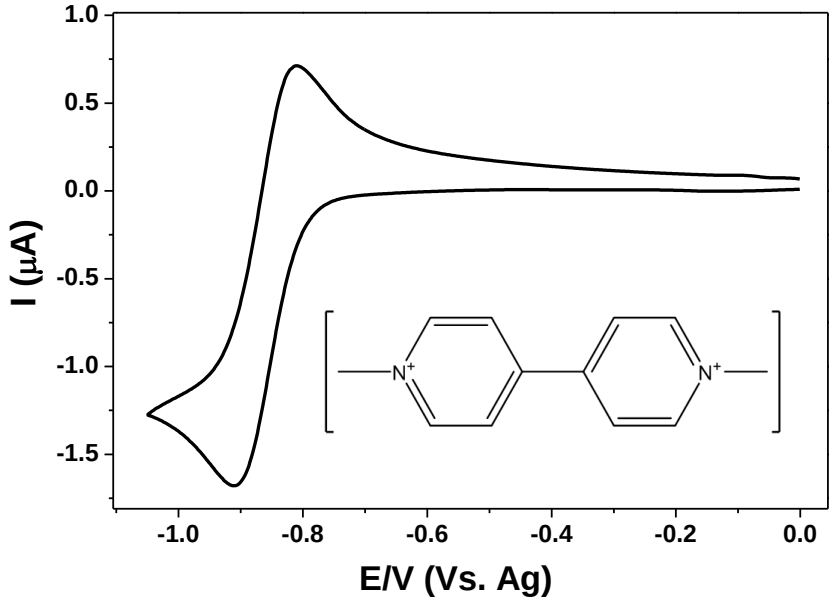

Figure 6.7. CV at 20 mV/s for 1 mM MV^{2+} at 50 µm diameter, 7 mm long Ag wire electrode vs. Ag-pseudo reference in water with 0.4 M KNO_3 , ΔE_P = 98 mV. Inset: the molecular structure of MV^{2+}.

diffusion limited conditions. Figure 6.8 shows the spectrum of the radical after electrolysing 1 mM MV^{2+} solution in Cell A with a 1.1 mm ID sample tube for 2 min. The EPR scan was initiated as the potential was switched off.

The EPR spectrum obtained with 0.02 mT modulation, averaging 5 scans gave a signal to noise of 740:1. The Root Mean Square (RMS) value for the noise was calculated from the baseline on a low field side of the spectrum. The emerging hyperfine coupling suggests that no line broadening occurs due to electron exchange between radical-parent interaction proposed previously:[8]

$$(MV^{+\cdot}) + (MV^{2+})^* \rightleftharpoons (MV^{+\cdot})^* + (MV^{2+}) \,, \qquad (6.2)$$

This is probably due to the relatively low concentration of the parent molecule with respect to the radical species in the active part of the resonator. In fact the best least squares fit yielded a line width of 0.017 ± 0.003 mT for the smallest hyperfine

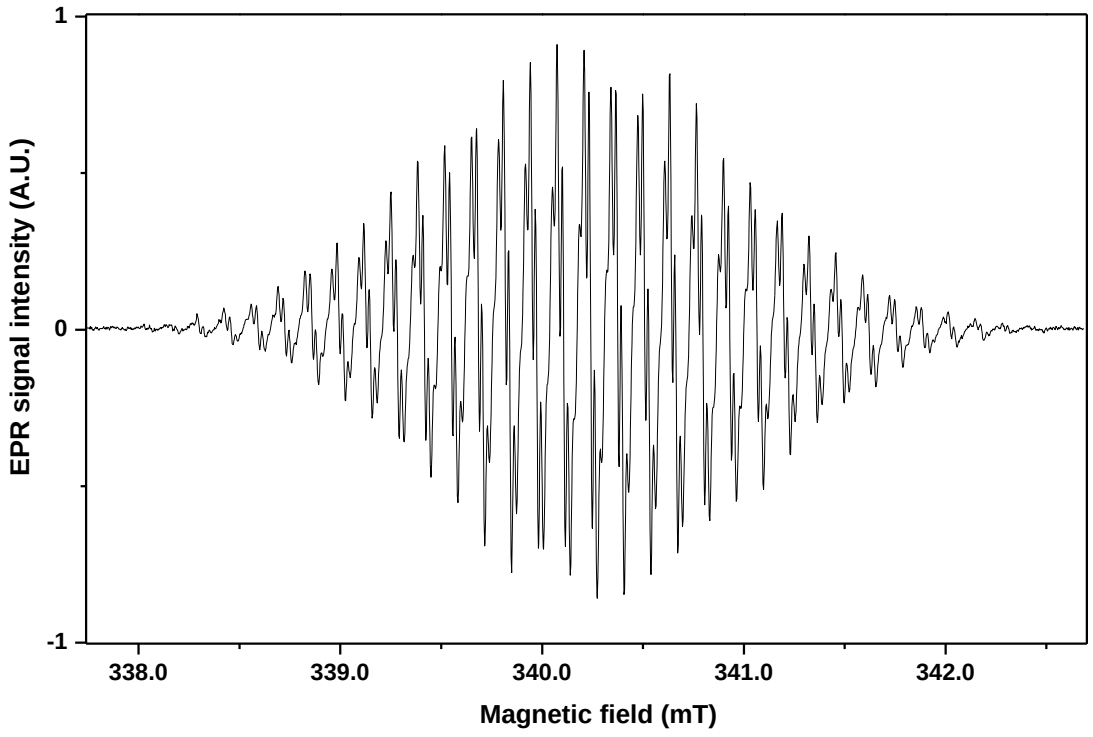

Figure 6.8. EPR spectrum of $MV^{+\bullet}$ recorded after a 2 min potential step at -0.9 V, 2 mW microwave power, 0.02 mT modulation

couplings, further suggesting that the lines were not excessively broadened by radical-radical or radical-parent molecular interactions, as in that case the line width would exceed the used modulation amplitude of 0.02 mT. The result in Figure 6.8 is in fact closer to those obtained through chemical reduction[9] or an exhaustive electrolysis of 1 mM MV^{2+} reported by Bard *et al.*[4]

A complementary option for scanning the magnetic field to record the entire EPR spectrum is to fix the field to a given value and monitor the signal amplitude as a potential perturbation is applied. This allows the generation of radical species at the electrode as a function of time and potential to be monitored simultaneously. Figure 6.9 shows an average EPR signal amplitude of 5 repetitions as a function of potential and time for 1 mM MV^{2+} in water and 0.4 M KNO_3, as the WE is stepped to -1.0 V for 10 seconds in cell B. Between the 5 repetitions, fresh solution was inserted to the cell via syringe pump.

The charge generated during a 10 second potential step was ca. 1.4×10^{-5} C, indicating

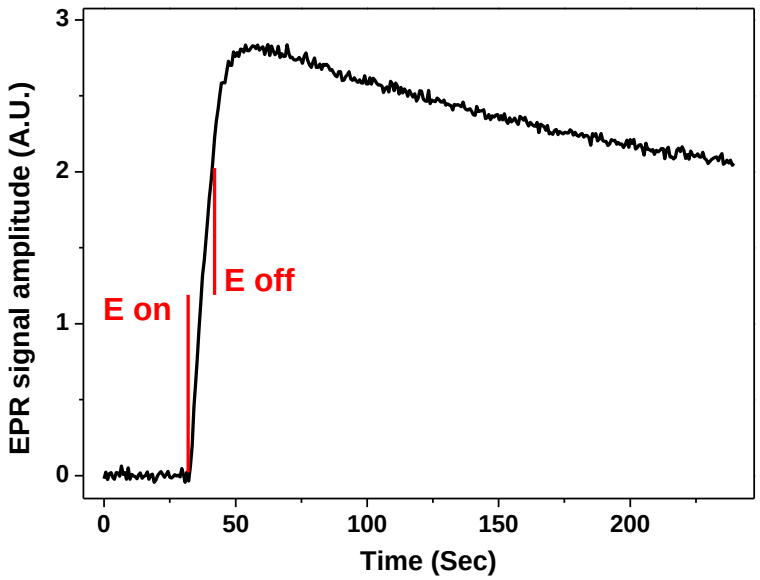

Figure 6.9. 5 scan average of the EPR signal amplitude at constant magnetic field as a function of potential and time during a 10 second potential step to -1.0 V. 1 mM of MV^{2+} in water at 50 µM diameter Ag wire electrode vs Ag pseudo RE and 0.4 M KNO_3 in the cell cell B. S/N = 122 with 2 mW microwave power and 0.1 mT modulation.

that the number of radical species ($MV^{+\bullet}$) generated was 8.7×10^{13}. The volume of sample inside the sensitive part of the resonator was 5 µL, and thus the concentration of the radical species can be estimated to ca. 30 µM, assuming 100 % efficient electron transfer and that the radical decay is negligible during the relatively short potential step. The S:N = 122:1, when the signal was taken to be the maximum EPR amplitude, while for the noise a RMS was calculated from the region before the potential step. Extrapolating from the results in Figure 6.9, the limit of quantification (LOQ) was estimated to be 7.1×10^{12} and the limit of detection (LOD) 2.1×10^{12} spins or 2.4 and 0.7 µM, respectively if the experiment was to be repeated 5 times.

The increase in the EPR signal is rapid after the potential step is applied at 32 seconds into the experiment. The EPR signal intensity increases for ca. 10 seconds after the potential switches off at 42 seconds, which could be attributed to the radical diffusing away from the electrode surface introducing changes to the filling factor and to the distribution of the radical within the H_1 field inside the sample volume. Also a formation of EPR silent radical cation dimer in water has been proposed[10, 11]

$$2\ MV^{+\cdot} \rightleftharpoons (MV)_2^{2+}\ , \qquad (6.3)$$

the presence of which could have an effect on the EPR signal at least on short timescales at the vicinity of the WE. The reliability of the transient method is further investigated in Chapter 7, where the artefact of increasing EPR signal amplitude after the potential is switched off is explained in more detailed fashion.

During the following 180 seconds after the potential was switched off the signal intensity decreased to 70 % of the largest value, confirming the observation that $MV^{+\bullet}$ is indeed a stable radical in aqueous systems at least around neutral pH. No decay constant was calculated, as with the setup employed the possibility of the stable

radical diffusing out of the sensitive part of the resonator within 180 seconds could not be ignored.

A wider potential sweep CV between -0.2 and -1.4 V for both reduction peaks of MV^{2+} is shown in Figure 6.10 for the cell B, corresponding to the electron transfer process in Equation 6.1 and also

$$MV^{+\cdot} + e^{-} \rightleftharpoons MV^{0}\,, \qquad (6.4)$$

where the paramagnetic one electron reduction product is further reduced to diamagnetic and EPR silent MV^{0} species. An increase in the EPR signal amplitude (right y-axis) was observed (1) as the reduction in Equation 6.1 started to produce the paramagnetic species at the WE (left y-axis), and did not cease until the peak current for the second reduction step (2). After this point, the EPR signal remained constant while the switching potential was reached and the scan reversed, indicating that a

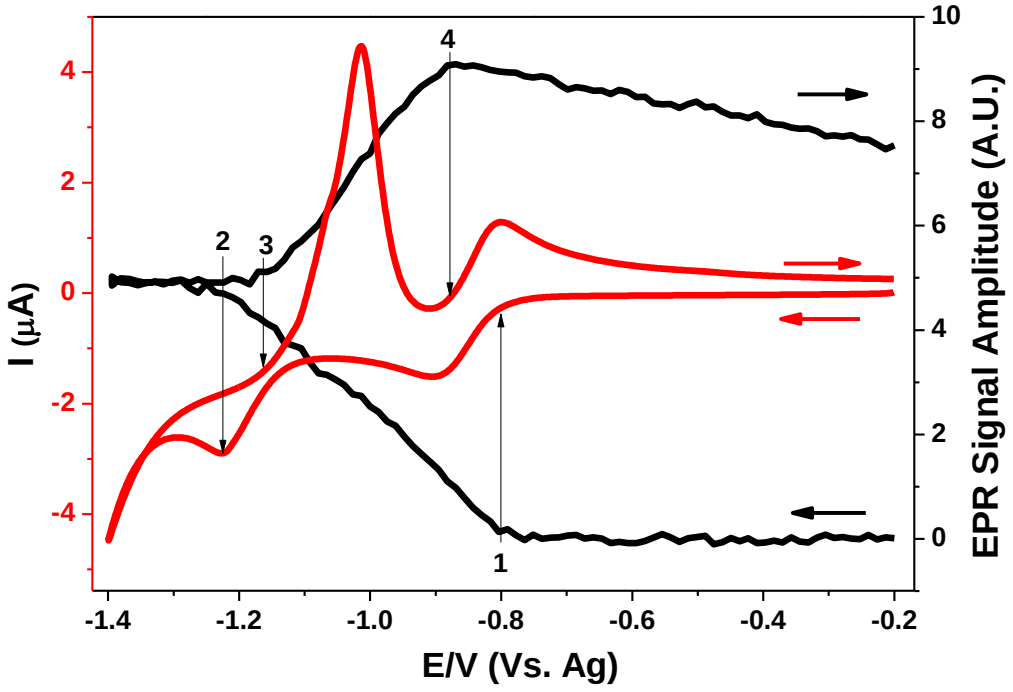

Figure 6.10. EPR signal amplitude (right y-axis) vs redox processes for 1 mM $MV^{2+/1+\bullet/0}$ (left y-axis) in water during 20 mV/s CV with 50 µm diameter Ag wire electrode vs Ag pseudo RE, 0.4 M KNO_3 in the cell B. 2 mW microwave power and 0.1 mT modulation.

steady concentration of radical species was maintained in the cell for ca. 20 seconds, at least on the EPR sensitivity scale. This result seems surprising as at high negative potentials the parent MV^{2+} molecule would be expected to reduce to MV^{0}, while the already generated $MV^{+\bullet}$ would also go through the second reduction step, thus leading to diminishing EPR signal.

The EPR signal intensity started to increase again during the return scan at the onset of the stripping peak (3) on the voltammogram, where the Equation 6.4 was reversed. The shape of the first oxidation peak during the reverse scan suggested a precipitation or deposition of the neutral MV^{0} to the electrode surface, from where it was released during the return scan. This was also supported by the EPR as the rate of EPR signal increase between points (3) and (4) was ca. 25 % larger than between (1) and (2), suggesting that the arrival of the species to the electrode surface exceeded the diffusion limit. Integration of the stripping peak yielded a charge of 2.5×10^{-5} C or 1.6×10^{14} molecules being oxidized during the reversal of Equation 6.4.

Finally the EPR signal intensity started to decrease at the onset of the second oxidation peak of the return wave (4) where the Equation 6.1 was reversed. The signal intensity diminished by less than 20 %, as the radical diffused throughout the sample volume did not have time to arrive to the electrode for oxidation before the experiment finished.

The unexpected levelling of the EPR signal intensity at potentials beyond ca. -1.2 V in Figure 6.10 was further investigated by applying two independent 10 second potential steps at -1.1 V and -1.3 V, corresponding to points just before and after the second reduction step, respectively. Figure 6.11 displays the EPR amplitudes (y-axis) as a function of time (x-axis), and the applied potentials.

For the -1.1 V potential step corresponding to the process in Equation 6.1 the EPR signal increased as expected based on -1.0 V potential steps in Figure 6.9 and ca. 1.5×10^{-5} C of charge was transferred. On the other hand, when the potential was stepped to -1.3 V, after the initial increase in the EPR signal a distinct plateau of slower rate was observed, and didn't resume at the expected rate until the potential was switched off. None the less, as almost exactly twice the charge was generated during the step (3.1×10^{-5} C) combined with exactly double the EPR signal, there is a clear quantitative evidence that the final product in the solution is the paramagnetic $MV^{+\bullet}$ and not the neutral MV^0 that the applied potential would suggest.

With Figure 6.10 it was determined that MV^0 is likely to deposit to the surface of the electrode, so the increase of the EPR signal after the potential is switched off at -1.3 V can be attributed to a process in Equation 6.5, proposed for example by Monk *et al.*[11]

$$MV^0 + MV^{2+} \rightarrow 2MV^{+\cdot}\,, \tag{6.5}$$

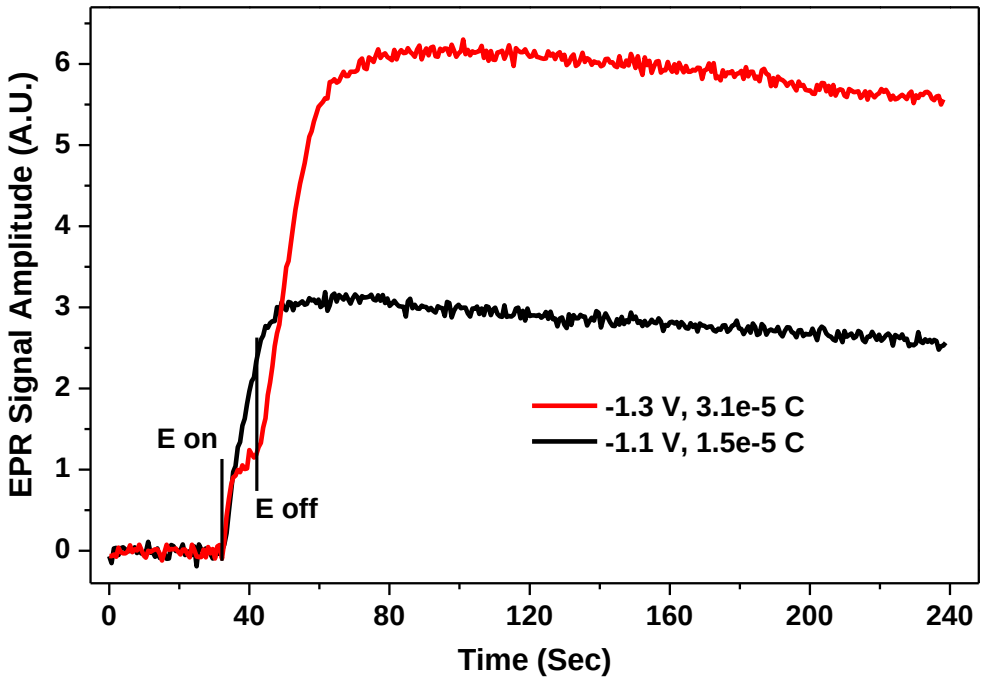

Figure 6.11. EPR signal amplitude vs time during 10 second potential steps from -0.2 V to -1.1 V and -1.3 V with 50 µm diameter Ag wire electrode vs Ag pseudo RE, 0.4 M KNO_3 in the cell B. 2 mW microwave power and 0.1 mT modulation.

although results reported therein did not display similar quantitative behaviour described here. Due to an existing concentration gradient, MV^{2+} species still diffuses to the electrode surface after the potential step and can react with the MV^{0} thus yielding two paramagnetic molecules. As long as there is applied potential the paramagnetic product from Equation 6.5 is further reduced to the diamagnetic form almost quantitatively, and a plateau in the EPR signal intensity is observed.

Clearly this setup allows the characterization of electrode processes under a precise potential control on a quantitative level with high EPR sensitivity. In the future EC-EPR could be used for example to study comproportionation reactions, previously performed on UMEs, at equal or even lower redox mediator concentrations than before.[12]

Finally cell A with 1.1 mm ID sample tube was tested using acetonitrile with a moderate dielectric loss as a solvent. Figure 6.12a displays the CV obtained with 100 mV/s scan rate over both reduction steps for 1 mM MV^{2+} at 50 µm diameter platinum WE vs. Ag-pseudo reference using 0.2 M TBAP as a supporting electrolyte. Clearly in acetonitrile the neutral MV^{0} does not deposit to the electrode nor precipitate out of the solution at least to any significant extent, as both peaks of the return wave have symmetry indicative to mass transport limitation when compared to the CV in Figure 6.10. The larger cell resistance is obvious from the stretched ΔE_p value for the first wave (118 mV) when compared to the aqueous results.

The high EPR sensitivity is evident from Figure 6.12b which was obtained after stepping the potential to -0.3 V with a single EPR scan for a concentration of ca. 20 µM of $MV^{+\bullet}$ giving S:N of 72:1 for 42 sec scan time, indicating that EC-ERP measurements are possible also with organic solvents.

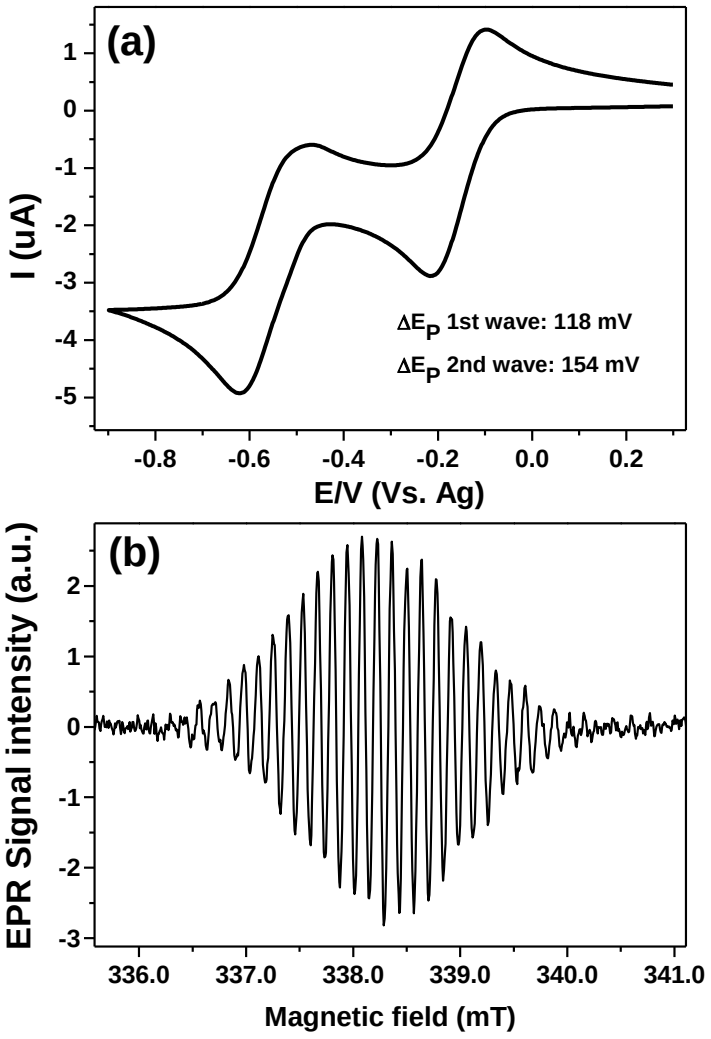

Figure 6.12. 1 mM MV^{2+}, 0.2 M TBAP in anhydrous acetonitrile at 50 µm diameter Pt wire electrode vs. Ag-pseudo reference (a) 100 mV/s CV, (b) EPR spectrum of $MV^{+\bullet}$ in the cell A, 2 mW microwave power, 0.05 mT modulation and 42 sec scan time.

6.5. Conclusions

A novel design of EC-EPR cell has been presented and its electrochemical performance demonstrated with well-known redox mediators. The electrochemical EPR performance was analysed by characterising the behaviour of MV^{2+} in an aqueous system. Although designed primarily for aqueous samples, the applicability for organic solvents has also been demonstrated. These results suggest that the potential control of the cell is precise enough for analytical experiments, while the

simultaneous EPR behaviour of the system can be monitored quantitatively under inert atmosphere.

Silver, gold and platinum can be used as a WE material, but also a piece of mesh has been inserted to the capillary instead of a wire and successful EC-EPR experiments performed, although at the expense of the potential control.

In terms of EPR sensitivity the LGR turned out to perform as well as a commercially available cylindrical TE_{011} resonator. The sensitivity of the LGR allows the use of relatively small surface area micro wires and also a true miniaturization of the electrochemical cell. On the other hand, as the syringe pump/potentiostat/EPR interface can be programmed and thus certain experiments automated, in the future signal averaging can be efficiently used to study short lived radicals.

Furthermore, especially for organic solvents it is strongly recommended that an oxygen saturation study, such as in Figure 6.1 is conducted to confirm the time period within which the sample remains oxygen and moisture free, as both electrochemical and possible follow up chemical reactions are extremely sensitive towards the presence of molecular oxygen and water in the sample solution.

Obviously there are several parameters to optimise in EC-EPR, depending on the system under study. The design demonstrated here allows the maximum flexibility between the electrochemistry and EPR. The next chapter involves a detailed characterization of the setup for the absolute quantification of paramagnetic species in EC-EPR experiments.

References

1. I. Dumitrescu, P. R. Unwin and J. V. Macpherson, *Electrochem. Commun.*, 2009, **11**, 2081-2084.
2. J. S. Hyde and W. Froncisz, in *Advanced EPR: applications in biology and biochemistry*, ed. A. J. Hoff, ELSEVIER, 1989, pp. 1-29.
3. A. C. Fisher, *Electrode Dynamics*, Oxford University Press, Oxford, 1996.
4. J. G. Gaudiello, P. K. Ghosh and A. J. Bard, *J. Am. Chem. Soc.*, 1985, **107**, 3027-3032.
5. L. Zhuang and J. Lu, *Rev. Sci. Instrum.*, 2000, **71**, 4242-4248.
6. R. M. Elofson and R. L. Edsberg, *Can. J. Chem.*, 1957, **35**, 646-650.
7. C. L. Bird and A. T. Kuhn, *Chem. Soc. Rev.*, 1981, **10**, 49-82.
8. R. N. Bagchi, A. M. Bond and F. Scholz, *J. Electroanal. Chem.*, 1988, **252**, 259-267.
9. W. R. Dunham, J. A. Fee, L. J. Harding and H. J. Grande, *J. Magn. Reson.*, 1980, **40**, 351-359.
10. E. M. Kosower and J. L. Cotter, *J. Am. Chem. Soc.*, 1964, **86**, 5524-5527.
11. P. M. S. Monk, R. D. Fairweather, M. D. Ingram and J. A. Duffy, *J. Chem. Soc. Perkin Trans. 2*, 1992, 2039-2041.
12. C. Amatore, M. F. Bento and M. I. Montenegro, *Anal. Chem.*, 1995, **67**, 2800-2811.

Chapter 7 - Analytical measurements in quantitative EC-EPR

Requirements for Quantitative EPR and analytical measurements were discussed in Chapter 4. This chapter involves the characterisation of the EC-EPR setup described in Chapters 5 and 6 for analytical work, addressing the most significant sources of errors in quantification of the number of paramagnetic species in EC-EPR. 1,4-benzoquinone was used as a model system due to its simple EPR spectrum[1], but also because of its relevance in biochemical processes,[2-11] and will be further studied in Chapter 8.

7.1. Experimental section

7.1.1. Materials

1,4-Benzoquinone (Fluka, certified purity 99.99 %), Tetrabutylammonium perchlorate (TBAP; Fluka, ≥99.0 %, for electrochemical analysis), 4-hydroxy-TEMPO (TEMPOL; Fluka, ≥98 %), 2,2-Diphenyl-1-picrylhydrazyl (DPPH) and anhydrous acetonitrile (99.8 %) were purchased from Sigma-Aldrich. The acetonitrile was dried inside a glove box over 3 Å molecular sieves (10 % m/v) for 48 hours.[12]

7.1.2. Methods

The sample tube diameter throughout the experiments was 0.8 mm. Except for the weighing of the chemicals, all solutions were prepared and stored inside a glove box. An aliquot of sample was removed from the glove box just prior to measurements in a gas tight glass syringe, and was purged with dry N_2. The setup utilised allows the study of samples *in situ* within an inert atmosphere, making sure that the samples remained oxygen free and dry throughout.

For the quantitative measurements a fine gauge K thermocouple (RS) was inserted in to the EC-EPR cell, downstream of the WE and outside of the sensitive part of the Loop Gap Resonator (LGR) to measure the temperature of the sample solution during experiments, thus removing errors related to the temperature dependency of EC and EPR. All of the EC and EC-EPR experiments were performed in dried acetonitrile using 0.2 M TBAP as supporting electrolyte vs Ag|AgCl.

Saturation curves for TEMPOL and the semiquinone radical ($SQ^{-\bullet}$) were constructed, and saturation started to take place gradually at powers beyond 1.2 mW for both species (Figure 7.1). During QEC-EPR experiments, further 2 to 4 dB was added to the attenuation

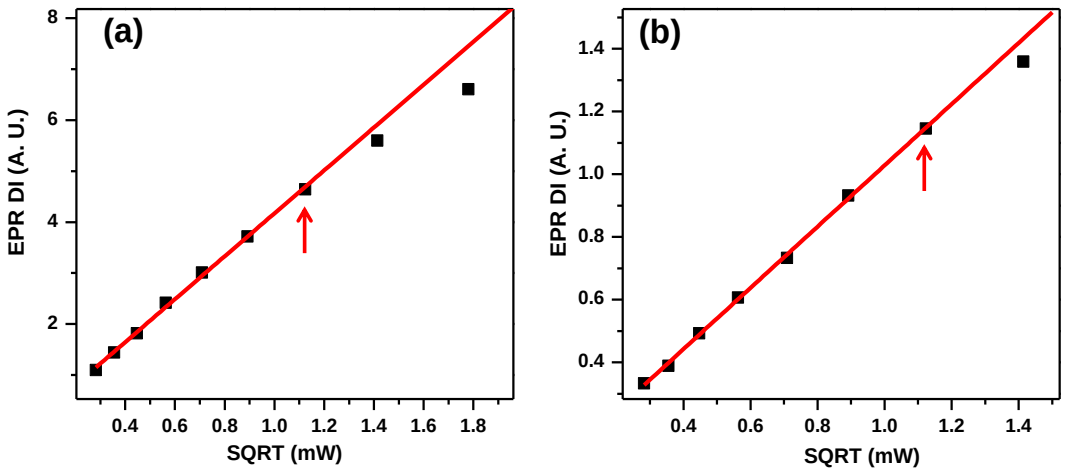

Figure 7.1. Saturation curves for (a) TEMPOL and (b) $SQ^{-\bullet}$ in anhydrous acetonitrile + 0.2 M TBAP. Saturation was observed to occur at powers beyond 1.26 mW. The last non-saturated point is marked with a red arrow.

to make sure that the samples remain unsaturated for quantification. For $SQ^{-\bullet}$ the saturation was measured for the centre line, as it has been observed to be the most easily saturated[13] by applying 10 seconds potential steps and waiting for 10 seconds before initiating the EPR scan, infusing fresh solution into the cell between each measurement.

When reporting EPR results, signal amplitude (SA) is used to indicate the peak to peak height of the 1st derivative EPR line, and double integrated (DI) signal intensity signifies the area under an EPR absorption curve. This distinction is significant, as in EPR the area under the absorption curve is proportional to the number of radicals in the sample, and thus quantification should only be performed by double integrating the EPR spectrum, as the SA is sensitive to the line width of the radical.

7.2. Results and discussion

7.2.1. 1,4-benzoquinone electrochemistry

To estimate the accuracy and precision of quantification in the *in situ* EC-EPR cell, a reduction of BQ in acetonitrile was studied. In an aprotic solvent, in the absence of proton donors, two consecutive 1 electron reductions take place to produce mono- and dianions according to:[14]

$$BQ + e^- \rightleftharpoons SQ^{-\bullet} + e^- \rightleftharpoons BQ^{2-}\,, \qquad (7.1)$$

where the intermediate of the first reduction step is EPR active semiquinone radical $SQ^{-\bullet}$. Figure 7.2a displays the EPR spectrum of $SQ^{-\bullet}$, where the 4 equivalent protons give rise to 1:4:6:4:1 spectrum for DI. Figure 7.2b displays a CV of 0.8 mM BQ at 6 mm length WE in the *in situ* electrochemical cell at 150 mV/s scan rate, where the two reduction steps are clearly visible. The first reduction is reversible compared to the second one, where adsorption

effects have been suggested to be the cause for the asymmetry.[15] The potential difference between the 1st and 2nd reduction peaks is ca. 1.2 V, indicative of the difficulty of further reducing the negatively charged $SQ^{-\bullet}$.

Figure 7.2c shows the charge generated during 10 second potential steps to diffusion

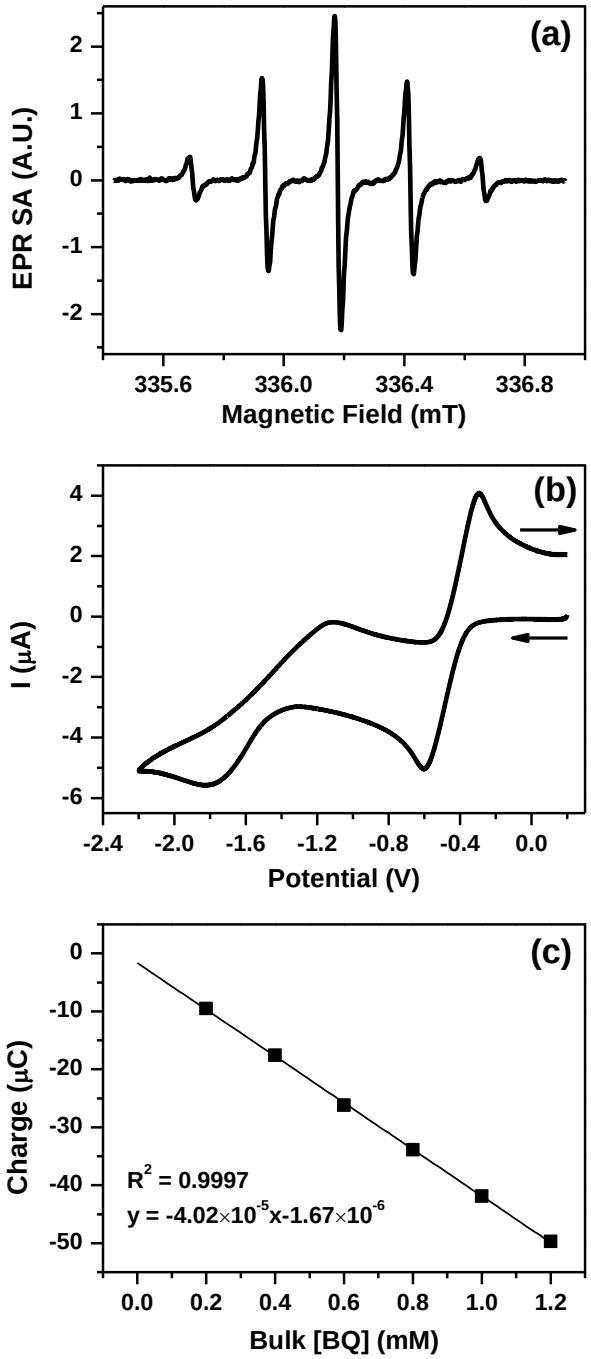

Figure 7.2. (a) EPR spectrum of $SQ^{-\bullet}$ radical displaying expected 1:4:6:4:1 line intensity ratio. (b) CV of 0.8 mM BQ in acetonitrile at Pt wire electrode, 6 mm length, 150 mV/s. (c) Relation between charge generated and [BQ] from 10 second potential steps to limiting potential of -0.8 V.

limiting potential of -0.8 V as a function of bulk [BQ]. Each data point represents an average of 5 individual potential steps with relative standard deviation of ≤ 1% across the entire concentration range, where fresh solution was infused to the EC-EPR cell between each repetition. Due to high reproducibility and linearity of the results, the intercept of the straight line (-1.67×10^{-6} C) was treated as a background and subtracted from the data. Thus comparing the charge generated between 1.2 and 0.2 mM BQ, the ratio obtained was 6.1, suggesting that convection, which would be expected to play a bigger role at high concentrations yielding larger than expected currents, was negligible.

The charge generated at a 6 mm long electrode for 1.0 mM BQ was compared to that generated at a 2 mm long electrode, and the relationship was observed to be proportional to the length within 3 % after subtracting the background current, indicating that the current density at the 6 mm electrode should be relatively evenly distributed along the electrode length. This is important for QEC-EPR, as the density of the radical species can be assumed to be uniform throughout the WE length. This is not the case for large surface area electrodes in flat cells or channel flow cells,[16, 17] where error would be introduced when quantifying against a reference standard. An additional problem for large surface area electrodes is the large cell time constant, which makes the study of short potential steps or current pulses unreliable.[18]

7.2.2. BQ EPR transient measurements

The mean lifetime of the $SQ^{-\bullet}$ was investigated by utilising transient measurements. The WE was stepped to -0.8 V for 10 seconds and the EPR SA was measured as a function of time, as the external magnetic field (H_0) was fixed to the centre line of the $SQ^{-\bullet}$. As the $SQ^{-\bullet}$

line width is extremely [BQ] dependent,[19] the effect of the position of H_0 and the amplitude of the modulation field (H_{mod}) to the transient response was investigated first.

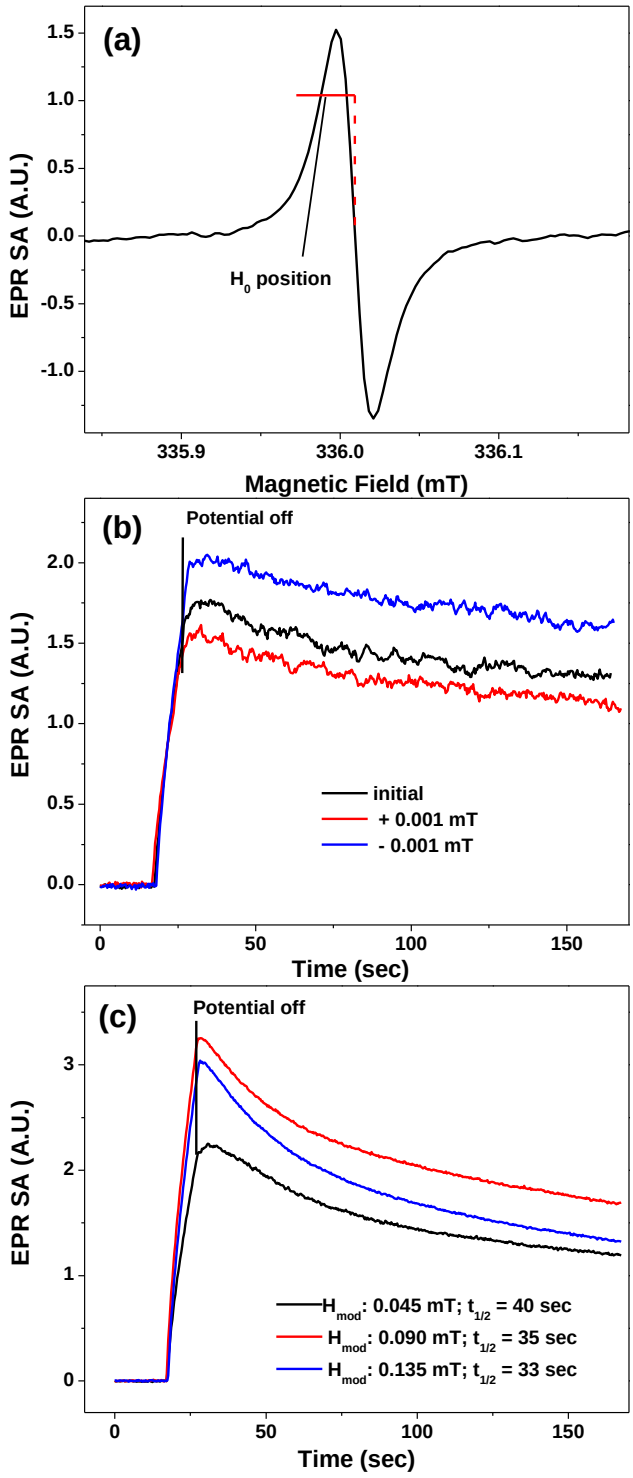

Figure 7.3. (a) Static field position for transient measurements, (b) The effect of setting the static field position to EPR SA during transient measurements, (c) The effect of over-modulation to the EPR SA. b) and c): 5 mm Pt wire electrode, 1.0 mM BQ.

Figure 7.3a shows the position of H_0 used to record the black transient in Figure 7.3b, where the high field end of H_{mod} was set to the zero amplitude of the 1st derivative (dashed red line), and the H_{mod} amplitude is represented by the red horizontal line. Figure 7.3b displays the effect of choosing the H_0 position in terms of EPR SA during transient measurements for the reduction of 1.0 mM BQ solution. For 0.04 mT modulation amplitude, only a 0.001 mT increase in H_0 position, keeping the modulation amplitude the same, can result up to 11 % reduction in the EPR SA (red transient), whereas 0.001 mT decrease was observed to increase the amplitude by 15 % (blue transient). It is important to notice that 0.001 mT shift in the magnetic field equals ca. 30 kHz drift in the microwave frequency, suggesting that monitoring the frequency while the transient is recorded is crucial to avoid errors in mean lifetime estimations, and for repetitive work the H_0 position must be adjusted accordingly.

Excessive over-modulation of the EPR line could be assumed to average out any drifts in the microwave frequency, or ambiguity related to selecting the H_0 position. Figure 7.3c shows a distortion in the decay behaviour for 1.0 mM BQ solution, where the H_0 relative to the $SQ^{-\bullet}$ centre line was set as in Figure 7.3a for each transient. Increasing the modulation amplitude increased the SA initially, but after H_{mod} ≈ three times the full width half height (FWHH), the EPR response had started to decrease, and the apparent half lifetime ($t_{1/2}$) to shorten because of the over modulation.

These observations are contrary to those of Goldberg *et. al.*,[20, 21] where the over-modulation was not observed to affect the decay behaviour, probably due to relatively short lifetimes of the species investigated. None the less, in EC-EPR one should have reservations about any work relying on transient measurements, as decisions about H_{mod} amplitude and the H_0 position can influence the results significantly.

Transient measurements for concentrations between 0.2 and 1.2 mM are shown in Figure 7.4, where the modulation amplitude was adjusted to equal the FWHH for each BQ concentration and the static field position adjusted as in Figure 7.3a, as this procedure was observed to result in the highest reproducibility. 0.2 and 0.4 mM concentrations were recorded as 5 repetition averages, where fresh solution was injected to the cell between repetitions, and higher concentrations were recorded as averages of 4 repetitions. The microwave frequency was not allowed to drift more than 10 kHz during individual measurements.

Further investigation of Figure 7.4 shows the inconsistency of the results, even though experiments were conducted under rigorous control of the EPR parameters. The vertical black line sketched at the 33 second point indicates the time when the potential was switched off. For lower concentrations of 0.2 and 0.4 mM the EPR SA starts to decay right after the potential step, while for higher concentrations the SA increases even without applied potential, being most significant for 1.2 mM BQ.

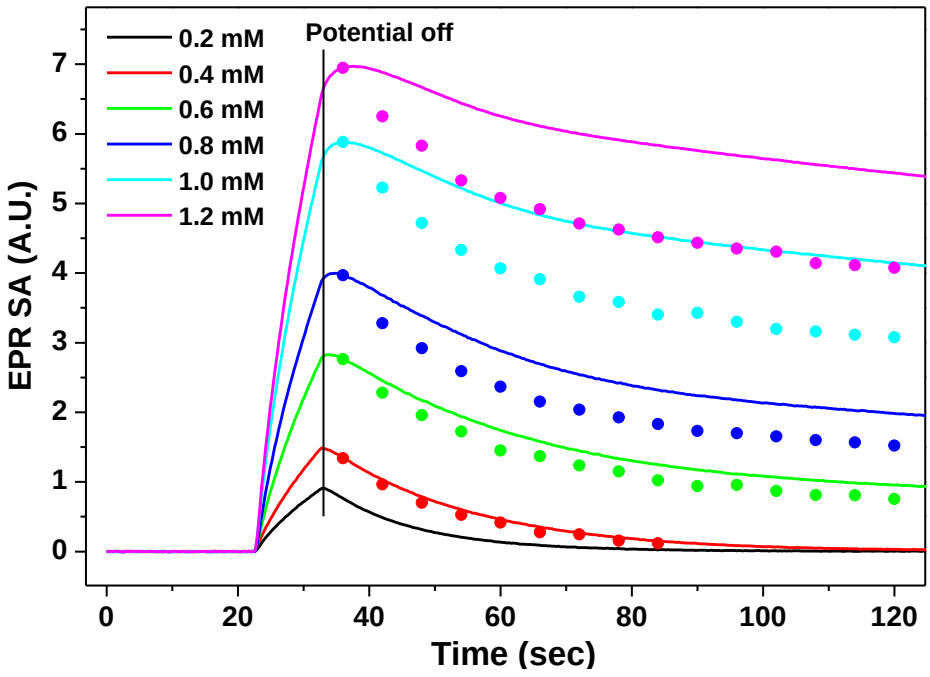

Figure 7.4. The dependency of EPR SA on [BQ] for transient measurements (solid lines) and for corrected transients, as explained in Figure 7.5 (circles). 6 mm length WE, 10 sec potential steps.

In previous work the effect of increasing EPR SA without applied potential for benzoquinone in aqueous, non-buffered solutions has been attributed to a comproportionation reaction, where an intermediate reduced by two electrons donates the other one to a parent molecule, thus yielding two paramagnetic species and accounting for the increase in SA.[1] Considering that in acetonitrile the first reduction step is known to be a single electron process, this does not seem like a reasonable conclusion.

To investigate the phenomenon of increasing EPR SA without applied potential, the measurements were repeated by recording only the centre line of the $SQ^{-\bullet}$ spectrum over time after switching off the potential. Figure 7.5a shows the change in the centre line width for 0.8 mM BQ, where the first time point was recorded at 3 sec after switching off the potential. Similar behaviour was observed for [BQ] between 0.4 and 1.2 mM, where the H_{mod} amplitude used was 1/3 or less of the FWHH throughout, as for Lorenzian lines this will introduce a maximum of 3 % modulation broadening.[22] A change in the line width versus time for stable radicals has been observed before by Petr *et. al.*[23], suggesting that transient measurements with fixed modulation amplitude can indeed lead to errors in radical lifetime estimations.

The line width was observed to decrease exponentially, implying that on short time intervals the amplitude of the Lorezian line will increase significantly, as shown in Figure 7.5a inset, where the amplitude of the Lorentzian line as a function of line width is plotted assuming that the signal area does not change over time. The red lines represent 95 % prediction bands of the exponential fit through regression analysis. The significance of this is that during transient measurements the EPR SA will increase spontaneously even after the potential is switched off as the recorded SA is convoluted by the change in line width, and this process competes with the decay of the radical species.

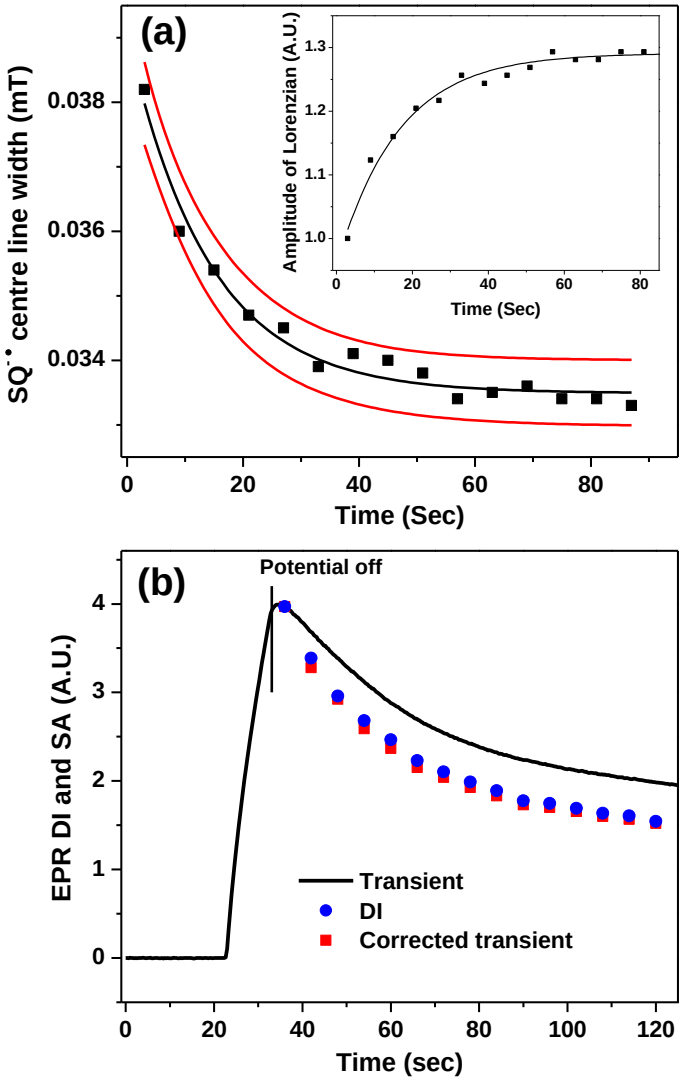

Figure 7.5. (a) The change in the $SQ^{-\bullet}$ centre line width as a function of time after the potential is switched off at 0 seconds, black line: an exponential fit, red lines: 95 % prediction bands. Inset: The effect of the line narrowing to the amplitude of the Lorenzian line. b) Transient measurement, EPR DI and transient deconvoluted by the change in the amplitude of the Lorenzian line. In 0.8 mM BQ at 6 mm long WE.

This is demonstrated in Figure 7.5b for 0.8 mM BQ showing the respective transient measurement (black line) from Figure 7.3, but also the DI (blue circles) of the $SQ^{-\bullet}$ centre line, normalised to match the transient SA for the first recorded data point. When the results from the transient measurement were corrected with the change in the Lorenzian amplitude from Figure 7.5a inset (red squares), almost a perfect match was observed. The change in the line width over time was observed for the whole range between 0.4 and 1.2

mM BQ, where the effect was minimal for the former and almost 25 % for the latter, and the corrected transients are collected to Figure 7.4. (circles)

A change in the line width therefore has a significant effect on the amplitude of the transient, but also to the recorded $t_{1/2}$ of radical species when using transient methods. Figure 7.6a shows the comparison of centre line widths while applying the potential (black squares) and 40 seconds after switching the potential off (red circles). For 0.2 mM BQ the reliable line width determination 40 seconds after the potential step was not possible due to fast decay and weak SA, and for 0.4 mM the result is a subject to large uncertainty, but extrapolation to 0.2 mM suggests that the line width is essentially identical whether the

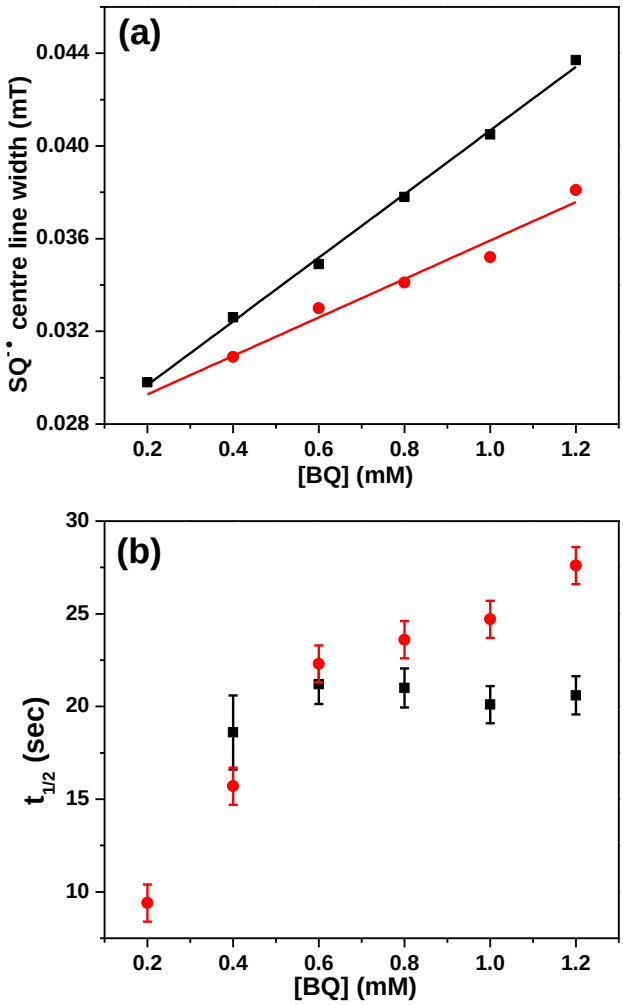

Figure 7.6. (a) The dependency of the $SQ^{-\bullet}$ centre line width across [BQ] during applied potential (black squares) and 40 seconds after switching off potential (red circles). (b) The $t_{1/2}$ estimations across [BQ] for transient measurements (red circles) and consecutive DI determinations of $SQ^{-\bullet}$ spectrum (black squares).

potential is applied or not.

Thus it is likely that as long as the potential is applied there is a strong spin-spin interaction between the radical species generated at the electrode surface, causing the increased linewidth due to shorter spin-spin relaxation time (T_2),[24] an effect that manifests more strongly at high BQ concentrations. After the potential is switched off, diffusion equilibrates the system, and the observed line width is more dependent on the radical-parent exchange interaction. This result emphasizes the importance of time-dependent diffusion when characterising radical species generated through EC-EPR experiments.

Figure 7.6b shows the $t_{1/2}$ values for transients fitted for 1st order exponential decay between 36 and 96 seconds from Figure 7.4 (red circles). The black squares show the decay behaviour when the whole $SQ^{-\bullet}$ spectrum is recorded and double integrated consecutively up to 60 sec after switching off the potential, and the resulting data plotted as ln(DI) vs time yielding straight line with a negative slope. The data point for 0.4 mM BQ was plotted only up to 36 sec, as the fast decay of the $SQ^{-\bullet}$ diminished the signal beyond reliable integration, and thus the data point has large uncertainty associated to it. The average $t_{1/2}$ for concentrations between 0.6 and 1.2 mM is 20.7 sec and the value is essentially independent of the [BQ]. Most importantly the results for 1.0 mM BQ, around a typical concentration for EC-EPR studies, the errors in $t_{1/2}$ values for transient measurements can be up to 20 % even if performed under rigorous control of EPR parameters, hardly a desirable situation.

If the line broadening is indeed due to the spin-spin interaction, the effect might not be as pronounced in setups where large surface area electrodes are used which do not benefit from enhanced mass transport and thus the concentration of the radical species in the vicinity of the electrode is lower. None the less, as setups utilising large surface area electrodes in conjunction with flat cells act as thin layer cells, the radical species can still be

confined to a relatively small volume and thus the dependency of the line width over time should always be checked due to the significant dependency of the Lorenzian line amplitude on the line width. Furthermore, different cell geometries and volumes are most likely to yield different line width data, depending on the relative amounts of radical and parent molecule concentrations. The results above also show the importance of studying electrochemical systems across a range of concentrations to discover the fundamental behaviour of the system.

Considering the corrected transients in Figure 7.4, it is clear that the decay observed is not purely 1st order, but has a significant constant associated to it. The decay could be due to residual O_2 in the solutions despite the utmost effort to keep the samples degassed, as the solubility of O_2 in acetonitrile can be up to 2.4 mM[25] and is known to reduce $SQ^{-\bullet}$ to BQ.[26] This notion is supported by the fact that the equivalent of 50-60 μM of $SQ^{-\bullet}$ was lost between 0.6 and 1.2 mM [BQ] on a time scale of 60 seconds after switching of the potential, which is also a plausible concentration for residual oxygen in the sample. Thus, due to the $SQ^{-\bullet}$ concentration gradient within the sample tube the decay can look essentially pseudo 1st order in terms of [$SQ^{-\bullet}$], even if two species are involved in the decay process.

The decay of EPR SA to zero for 0.2 and 0.4 mM BQ could then be explained by the fact that the [$SQ^{-\bullet}$] generated was 27 and 55 μM, respectively, determined from the EC data. Thus the [O_2] is large enough to re-oxidise $SQ^{-\bullet}$ to BQ in the time scale of the experiment. This re-oxidation would also explain the decreased $t_{1/2}$ values in Figure 7.6b for these two concentrations.

7.2.3. Quantification

Requirements for analytical measurements and quantitative EPR have been discussed in Chapter 4. The most important sample related variables: Q_L, η and H_1 are discussed below with some additional experimental parameters.

Quantification was performed by comparing the DI of the unknown amounts of $SQ^{-\bullet}$ against a reference standard TEMPOL by preparing a calibration graph with known concentrations. Varying amounts of TEMPOL were dissolved to dried acetonitrile containing 0.2 mM TBAP, making sure that the sample properties between $SQ^{-\bullet}$ and TEMPOL standards matched exactly. Thus the Q_L will be the same throughout the measurements and related errors in quantification are avoided as also the sample size and shape will remain the same due to utilisation of a flow through device where the cell position remain untouched between measurements.

The accuracy and precision of the quantitative measurements depend on the amplitude and the distribution of the H_1 field over the sample determining the effective η, and how accurately this can be reproduced between $SQ^{-\bullet}$ and TEMPOL.

To determine the H_1 distribution over the sample volume, the EPR response as a function of the z-placement in the 5L4G-resonator sample loop was measured by gluing a minute grain of DPPH to ca. 350 µm diameter capillary, thus making effectively a point sample, and inserting it into the EC-EPR cell. The cell was then attached to the resonator, filled with dried acetonitrile containing 0.2 M TBAP as electrolyte, thus making sure that the determined H_1 distribution in the resonator was exactly as during the EC-EPR experiments, and errors related to ε' and ε'' are avoided.

The H_1 distribution was first determined by moving the point sample across the resonator, and the results are shown in Figure 7.7 (black squares). The point sample was then placed

in the middle of the resonator (z-position 5), and the whole resonator moved relative to the modulation coils in z-direction to determine the uniformity of H_{mod} relative to the H_1 (red circles). The magenta line shows the location of the sensitive part of the loop gap resonator. The H_1 clearly extends outside the sensitive part of the resonator, 99.5 % of the signal originating between points -3 mm and 12 mm, and due to the uniformity of the H_{mod} relative to the H_1, the EPR response of the setup is governed by the distribution of H_1. To confirm this statement the corresponding H_1 values were multiplied by respective H_{mod} values and the results are displayed as green triangles in Figure 7.7 (H_1 convoluted). When comparing the integrated areas between H_1 and convoluted H_1, the disagreement was only ca. 1 %, indicating that the EPR signal within the LGR sample loop in z-direction is determined by the distribution of H_1 field.

When referencing against an external standard, one must consider the differences in η. Despite of being an ideal reference in terms of matching the resonator response between

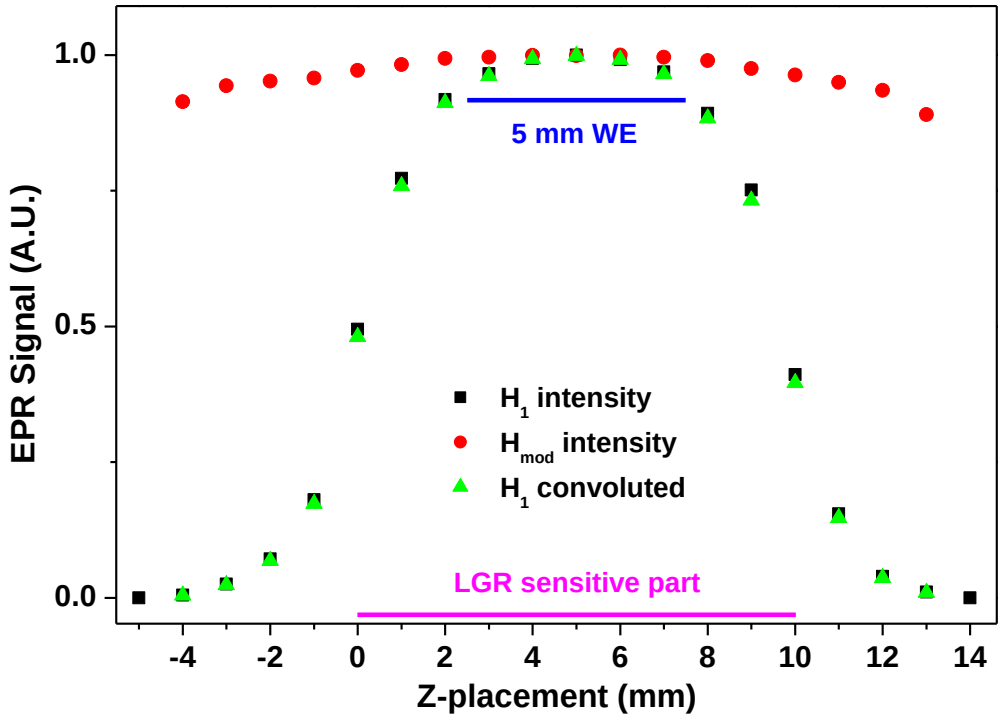

Figure 7.7. The EPR intensity of H_1 and H_{mod} across the LGR in z-direction. The blue line shows the length and location of the WE during quantification.

the unknown and the reference, TEMPOL fills the sample tube through its entire length, and the signal originates from a much larger volume than that of the EC-EPR. Knowing the length and placement of the WE allows the integration of the EPR signal from Figure 7.7 and a true correlation with the TEMPOL. For example, radical species generated at 5 mm WE placed as shown in Figure 7.7, and assuming an even current distribution over the electrode, occupies 50.7 % of the length from which the EPR signal originates in z-direction, which needs to be scaled with the signal originating from TEMPOL (positions -5 to 14). The precision in WE placement within the sample loop is better than +/- 0.5 mm, leading to maximum of 0.5 % error in signal intensity for 5 mm long WE.

7.2.4. $SQ^{-\bullet}$ generation efficiency

The absolute spin quantification for $SQ^{-\bullet}$ in acetonitrile was performed at [BQ] between 0.6 and 1.2 mM at 5 mm long WE positioned in the resonator as shown in Figure 7.7 above. The temperature of all the measurements, including the TEMPOL referencing, was 20.7°C (±0.5°C). Figure 7.8a displays the DI values of the entire $SQ^{-\bullet}$ spectrum against time for 1.0 mM BQ solution after stepping the WE potential to -0.7 V for 10 seconds. The experiment was repeated 3 times and the error bars represent 1 standard deviation of the mean value obtained. The quantification was performed by normalizing all of the data points to time zero and taking an average of them. Averaging the error bars across all of the data points yielded a mean standard deviation of 4 %.

The radical decayed exponentially with 1st order kinetics (red line), with mean lifetime of 20.1 sec. Scan times of 5.2 and 2.6 sec for the 1.5 mT sweep width used did not produce differences in EPR DI, once adjusted for the conversion time, suggesting that results

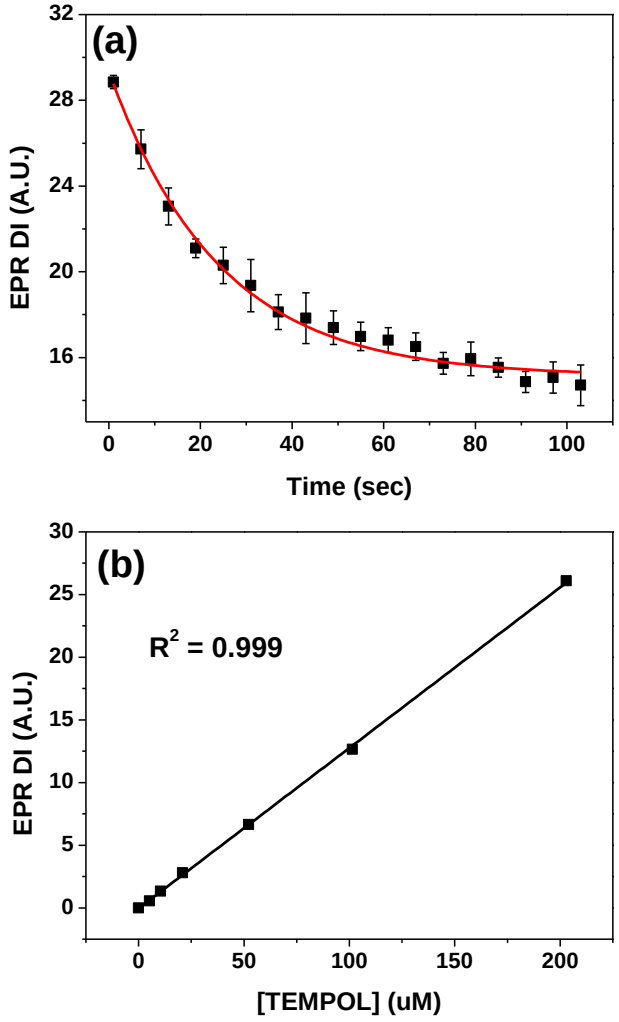

Figure 7.8. (a) The decay of the EPR DI of $SQ^{-\bullet}$ after 10 second potential step to -0.7 V at 5 mm length WE, 1.0 mM BQ. (b): TEMPOL calibration graph

obtained accurately characterize the concentration of the benzoquinone radical, and the error related to decay while the EPR spectrum is swept was minimal.

To quantify, a TEMPOL calibration graph between concentrations of 5 and 200 uM was constructed and is shown in Figure 7.8b. The high linearity of the graph confirms the reproducibility in critical coupling and consistent Q-value, which is a crucial factor in analytical work when high levels of accuracy and precision is required,[27] as the cell needs to be emptied between experimental runs. Before quantification with the calibration graph, the $SQ^{-\bullet}$ EPR DI was scaled to that of the TEMPOL by accounting for modulation amplitude, microwave power, difference in filling factors (explained with Figure 7.7) and scan times.

Figure 7.9 shows a graph of [$SQ^{-\bullet}$] versus charge generated, comparing the calculated concentration via electrochemistry (red circles) and that detected by the EPR for 0.6, 1.0 and 1.2 mM BQ (black squares) for potential steps between 3 and 10 seconds. To get the EC data, the charge generated was converted to number of electrons and then to concentration by accounting for the volume of the sample tube around the WE.

Across all 10 data points collected, the agreement for the radical concentration between the quantitative EPR and calculations based on charge generated through EC agreed within 3 %. The error bars for EPR data represent 4 % standard deviation, as determined in Figure 7.8a. The values obtained through EC are used as a benchmark against which the QEC-EPR data is compared due to the high R^2 value obtained, indicating that BQ in acetonitrile behaves as expected for quantitative one electron reduction.

Surprisingly the accuracy of quantification did not present any time dependency due to

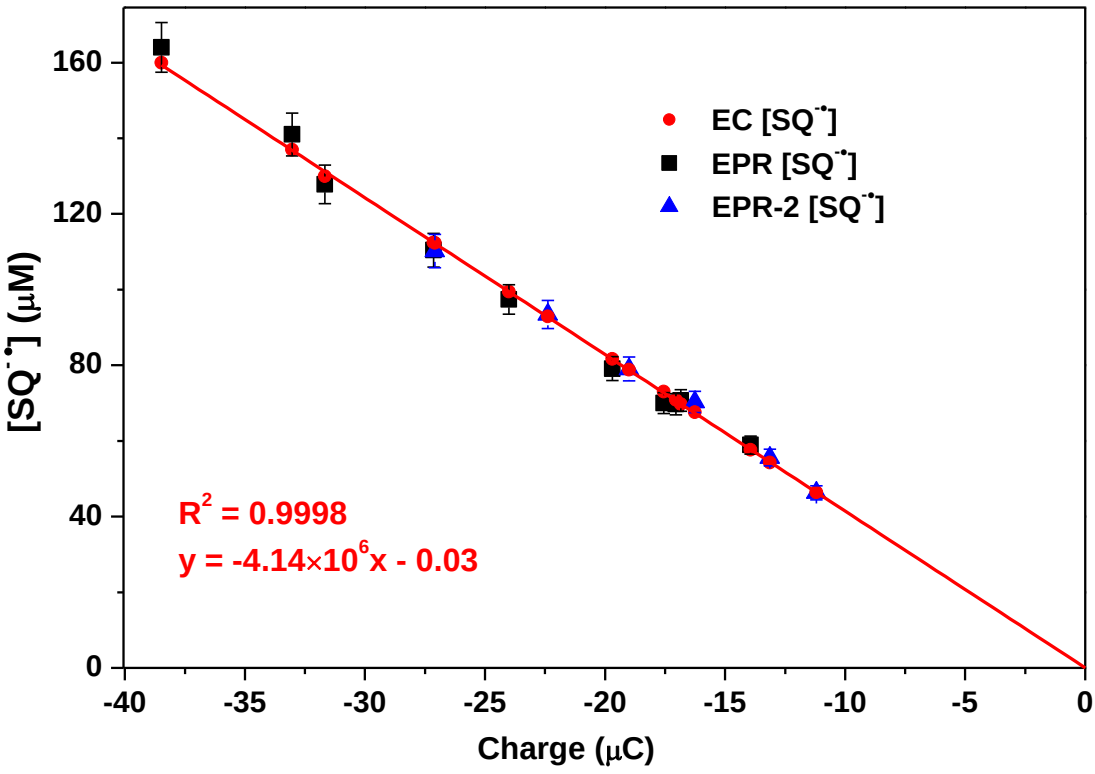

Figure 7.9. Red circles: radical concentration calculated based on charge generated at the WE. Black squares: quantitative EPR results for $SQ^{-\bullet}$ for 0.6, 1.0 and 1.2 mM BQ solutions after varying potential step lengths to the WE. Blue diamonds: EPR results for 0.8 mM BQ after reassembling the setup.

equilibration of the concentration gradient of $SQ^{-\bullet}$ after switching off the potential which would affect η, as would be expected for the radical species diffusing from the electrode surface towards the sample tube wall. This is probably due to the very narrow sample tube utilized (0.8 mm ID) relative to the diameter of the LGR sample loop (4 mm), making the effective H_1 uniform over the sample. Also COMSOL simulations suggested that the diffusion in the z-direction is negligible over the timeframe of the quantification.

To test the reproducibility of quantification, the whole setup including the EC-EPR cell was dismantled and a new 5 mm WE installed into the cell, and the EPR microwave bridge swapped to a different one. The blue triangles in Figure 7.9 represent the new quantitative results through EC-EPR for 0.8 mM BQ versus charge generated (red circles) for potential steps between 3 and 10 seconds after constructing a new calibration graph (not shown). High accuracy between the 6 data points, and when compared to the first dataset is obvious, providing evidence that high reproducibility of quantitative measurements is possible with our system.

The first conclusion based on the data in Figure 7.9 is that the radical generation efficiency is very close to 100 % for BQ in acetonitrile. Rather surprisingly the normalization of the EPR DI data to the time zero, as explained in Figure 7.8a was observed to yield accurate concentrations when compared to concentration obtained from EC, indicating that the radical does not decay during the 10 second potential step. This can be confirmed for example for 1.2 mM BQ data. The ratio between the charge generated between 10 and 3 second potential step was 2.29, while the respective ratio for the quantitative EPR data was 2.32, ca. 1 % difference. If the radical decayed during the potential step, the ratio of the EPR data would be less, accounting for the number of radicals lost during the excess 7 seconds of applied potential.

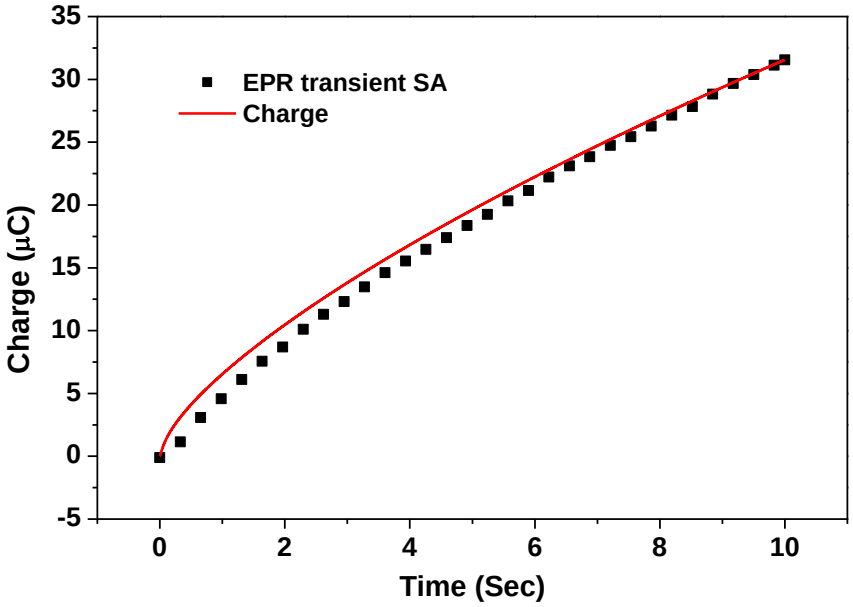

Figure 7.10. Rate of change of Coulombs and EPR SA of a transient during 10 second potential step for 1.0 mM BQ. The EPR data is normalised to 10 seconds.

This observation is further confirmed by Figure 7.10, where the rate of change of Coulombs is contrasted to that of an EPR transient SA for $SQ^{-\bullet}$ during a 10 second potential step for 1.0 mM BQ solution. At times under 1 second the amount of charge generated increases faster than the EPR signal, as the species diffuse from the WE surface to the bulk solution. For the final 5 seconds into the potential step the two rates match closely, indicating that any significant decay cannot take place. With respect to the EPR line widths and transient measurements, the $SQ^{-\bullet}$ line width was confirmed to remain constant at least between 5 to 10 seconds during the potential step, proving that the rate of increase of the EPR transient is an accurate representation of the rate of radical generation.

Finally considering the sensitivity of the system employed, the lowest quantified concentration was 46 µM originating from 3 second potential step in 0.8 mM BQ solution, where the S:N of the center line ca. 1 second after switching off the potential was 69. The modulation amplitude employed was 1/2 of the $SQ^{-\bullet}$ center line width. If a modulation amplitude equal to the center line width was used, concentrations of 3-4 µM could be

quantified with S:N = 10, provided that it would be performed relying only on the center line DI, equaling ca. 6×10^{12} spins with a single 5 second scan.

Results reported here show that the EPR decay behavior for $SQ^{-\bullet}$ in acetonitrile has a constant associated to it, as evident for example in Figure 2. The decay follows 1st order kinetics for about 60 seconds when the potential is switched off, after which a steady concentration is achieved. The decay of the $SQ^{-\bullet}$ did not interfere with the quantification, the main goal of this work.

7.3. Conclusions

An EC-EPR cell has been characterized for quantification of the number of paramagnetic species originating from electrode reactions using $BQ/SQ^{-\bullet}$ in organic solvent as a model system. Careful analysis of the setup employed and the results confirm that most of the sources of error typical to Q-EPR can be avoided or circumvented by proper precautions and understanding the physics behind EPR measurements.

The quantification was performed over varying [BQ] and potential step lengths covering over a threefold range in concentration, and all results showed linear dependency and excellent correlation with the expected behavior. Results suggest that for species producing a simple EPR spectrum such as $SQ^{-\bullet}$, micro molar concentrations can routinely be quantified, and by utilizing over modulation and signal averaging even sub-micro molar concentrations will be accessible.[28] If transient measurements are performed it is essential to control the EPR parameters precisely and to characterize the time dependent behavior of the system, although when possible it is often simpler to record consecutive EPR spectra to measure time dependent behavior.

The time taken to record a traditional field swept EPR spectrum limits the shortest transient response that can be recorded. However, an obvious extension to this work would be to utilize faster scans or even "rapid scan EPR"[29] combining multiple potential steps and stepped flow for recording much faster transients while reducing detection limits even further.

References

1. Y. H. Tang, Y. R. Wu and Z. H. Wang, *J. Electrochem. Soc.*, 2001, **148**, E133-E138.
2. H. Rauchová, M. Vrbacký, C. Bergamini, R. Fato, G. Lenaz, J. Houštěk and Z. Drahota, *Biochem. Biophys. Res. Commun.*, 2006, **339**, 362-366.
3. J. d. D. Ndikubwimana and B. H. Lee, *Biotechnol. Lett.*, 2014, **36**, 1917-1926.
4. N. Gueyen, K. Woolley and J. Smith, *Redox Biol.*, 2015, **4**, 289-295.
5. V. Geromel, N. Darin, D. Chrétien, P. Bénit, P. DeLonlay, A. Rötig, A. Munnich and P. Rustin, *Mol. Genet. Metab.*, 2002, **77**, 21-30.
6. J. Kundu, K.-S. Chun, O. I. Aruoma and J. K. Kundu, *Mutat. Res.-Fund. Mol. M.*, 2014, **768**, 22-34.
7. A. Vasseur, J. Muzart and J. Le Bras, *Eur. J. Org. Chem.*, 2015, 4053-4069.
8. B. Sarkar, D. Schweinfurth, N. Deibel and F. Weisser, *Coordin. Chem. Rev.*, 2015, **293–294**, 250-262.
9. S. Fukuzumi and K. Ohkubo, *Org. Biomol. Chem.*, 2014, **12**, 6059-6071.
10. R. Tang, H. Su, S. Duan, Y. Sun, L. Li, X. Zhang, S. Zeng and D. Sun, *RSC Advances*, 2015, **5**, 41949-41960.
11. M. Najam Khan, M. Al-Hinai, A. Al-Hinai and J. Dutta, *Ceram. Int.*, 2014, **40**, 8743-8752.
12. D. B. G. Williams and M. Lawton, *Journal of Organic Chemistry*, 2010, **75**, 8351-8354.
13. J. W. H. Schreurs, G. E. Blomgren and G. K. Fraenkel, *The Journal of Chemical Physics*, 1960, **32**, 1861-1869.
14. M. Quan, D. Sanchez, M. F. Wasylkiw and D. K. Smith, *J. Am. Chem. Soc.*, 2007, **129**, 12847-12856.
15. L. Jeftić and G. Manning, *J. Electroanal. Chem. Interfacial Electrochem.*, 1970, **26**, 195-200.
16. I. B. Goldberg, A. J. Bard and S. W. Feldberg, *J. Phys. Chem.*, 1972, **76**, 2550-2559.
17. B. A. Coles and R. G. Compton, *J. Electroanal. Chem.*, 1983, **144**, 87-98.
18. I. B. Goldberg and T. M. McKinney, in *Laboratory techniques in electroanalytical chemistry*, eds. P. T. Kissinger and W. R. Heineman, Dekker, New York, 1984, pp. 675-728.
19. T. Nagaoka, S. Okazaki, T. Itoh and T. Fujinaga, *J. Electroanal. Chem.*, 1981, **127**, 289-295.
20. I. B. Goldberg and A. J. Bard, *The Journal of Physical Chemistry*, 1971, **75**, 3281-3290.
21. I. B. Goldberg, D. Boyd, R. Hirasawa and A. J. Bard, *J. Phys. Chem.*, 1974, **78**, 295-299.
22. J. E. Wertz and J. R. Bolton, in *Electron Spin Resonance: Elementary Theory and Practical Applications*, McGraw-Hill Inc., USA, 1972, pp. 450-467.
23. A. Petr, L. Dunsch, A. Neudeck, N. Oesterreich, M. Mann and G. Domschke, *Berichte Der Bunsen-Gesellschaft-Physical Chemistry Chemical Physics*, 1994, **98**, 1033-1038.
24. J. A. Weil and J. R. Bolton, in *Electron spin Resonance: Theory and Practical Applications*, John Wiley & Sons, Inc., Hoboken, New Jersey, 2007, pp. 301-356.

25. C. Franco and J. Olmsted, *Talanta*, 1990, **37**, 905-909.
26. Y. Esaka, N. Okumura, B. Uno and M. Goto, *Analytical Sciences*, 2001, **17**, 99-102.
27. I. B. Goldberg, *J. Magn. Res.*, 1978, **32**, 233-242.
28. G. R. Eaton, S. S. Eaton, D. P. Barr and R. T. Weber, *Quantitative EPR*, Springer-Verlag, Wien, 2010.
29. R. W. Quine, G. A. Rinard, S. S. Eaton and G. R. Eaton, *J. Magn. Res.*, 2010, **205**, 23-27.

Chapter 8 - 1,4-benzoquinone electrochemistry in unbuffered aqueous solutions

In the previous section the reduction of BQ in dry acetonitrile was used to characterise the EC-EPR setup's capability to produce quantitative EPR results of electrochemical processes occurring at the electrode surface. In this solvent the electrode reaction is widely accepted to be two consecutive one electron reductions, where the product of the first step is paramagnetic semi-quinone. The chemistry of BQ in aqueous systems is much more complicated and to some extent controversial, and very few EC-EPR experiments exist. As discussed below, these EC-EPR experiments are also arguably of low quality, and do not show any quantitative character. Thus, to demonstrate the utility of QEC-EPR, and to probe some of the controversies of aqueous BQ chemistry, the setup was utilised to investigate BQ in unbuffered aqueous systems.

8.1. Background

The EC reduction of 1,4-benzoquinone (BQ) in well buffered aqueous solution is agreed to occur via a two electron, two proton process[1] where two electrons and two protons are transferred in one reduction wave to yield hydroquinone (HQ or BQH_2), as shown in Scheme 8.1. The same mechanism is also observed in non-buffered solutions at pH values where the proton concentration is higher than the BQ concentration.

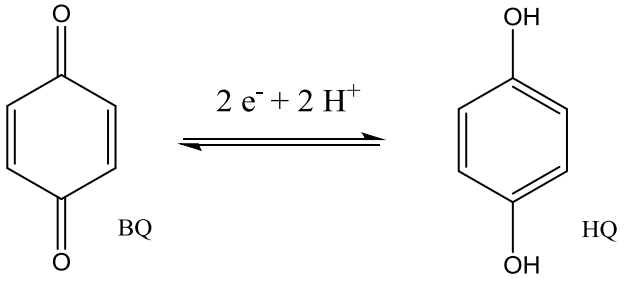

Scheme 8.1. Reduction mechanism for BQ in well buffered aqueous solutions

A "nine membered square" shown in Figure 8.1 has been used to characterise the possible pathways for BQ reduction, which depends for example on the [BQ], pH, solvent system and buffer components present in the sample. The possible electron transfers are shown horizontally and proton transfers vertically. Also the relevant pK_a values are included, the omitted values being -1 and below and therefore not of concern to this study.[2, 3]

In unbuffered aqueous solutions around neutral pH the reduction mechanism has been debated. Based on theoretical and experimental work Laviron[4] suggested that the mechanism varied with pH being either CECE, ECCE or ECEC where E represents an electron transfer and C is a chemical step, here a protonation (Figure 8.2).

Work done by Bailey *et. al.*[3] on quinone electrochemistry clearly demonstrated the mechanism shown in Scheme 8.1 for buffered aqueous solutions. The variation of pH of

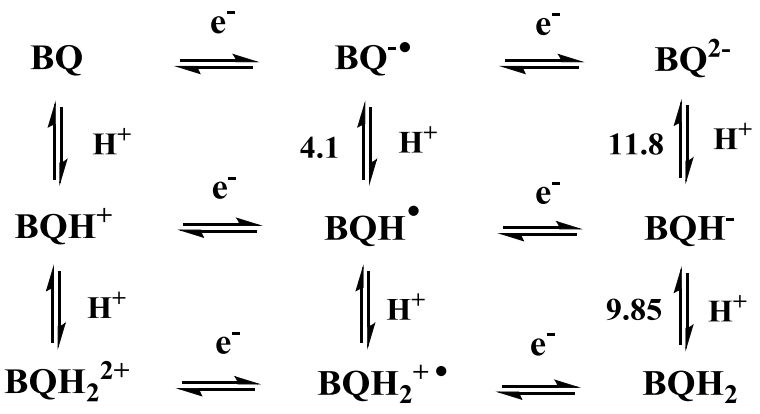

Figure 8.1. "Nine membered square" representing possible electron transfer (horizontal) and proton transfer (vertical) steps for reduction of BQ to BQH_2. Relevant pKa values are 4.1, 11.8 and 9.85.

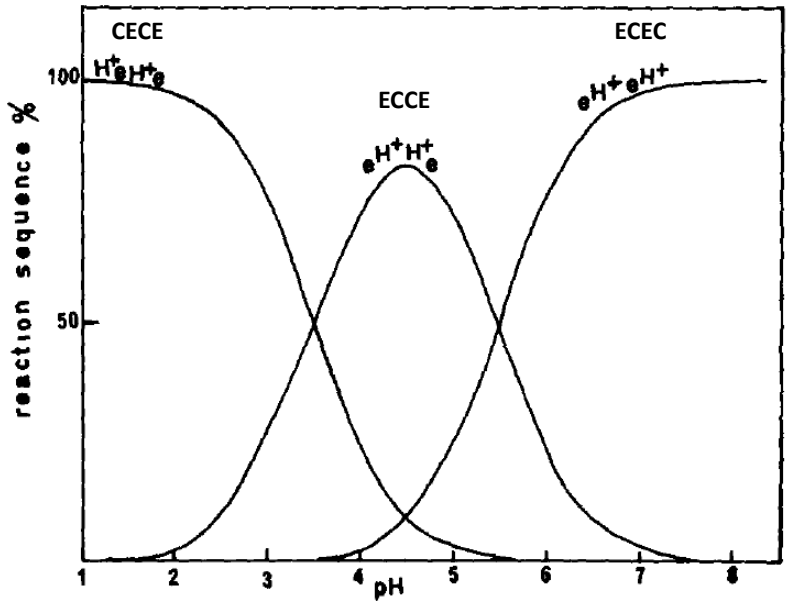

Figure 8.2. Possible reduction mechanisms for reduction of BQ in unbuffered aqueous solutions showing a pH dependency according to available protons. (From ref. [4])

buffered solutions between 0 and 10 in CV experiments did not affect the mechanism, but the half wave potentials were observed to be more positive the lower the pH, and the mechanism 2 e^- + 2 H^+. Between pH 10 and 12 the reaction mechanism was observed to be essentially 2 e^- + H^+, and at pH beyond 12 simply 2 e^-, although the decomposition of BQ at pH values beyond 9 complicated the interpretation of the data.

Also the behaviour in unbuffered aqueous solutions was investigated for the BQ/HQ couple. It was pointed out that the reduction of BQ consumes protons, which elevates the pH value at the electrode surface beyond that of the bulk solution depending on the BQ concentration used. For example around neutral pH values a single reduction wave was observed (Figure 8.3), which could be attributed to two electron reduction process without involvement of protons, as the slope of the half wave potential vs. pH displayed a slope of zero at pH values higher than about 4. Lowering the pH towards values where the proton concentration approaches the bulk concentration of BQ (pH = 3), a second reduction step appeared at more positive potentials and was attributed to the formation of BQH_2. At pH

values where $[H^+] \approx [BQ]$ only this more positive reduction peak was observed, indicating that in the presence of abundant protons the behaviour is similar to buffered solutions.

Bailey *et. al.* did not suggest detailed mechanisms such as that of Laviron's in Figure 8.2 for the reduction of BQ, but since their work several authors have presented disagreeing interpretations for the mechanism in unbuffered solutions for the redox couple occurring at more negative potentials.

Shim *et. al.*[5] conducted spectroelectrochemical experiments on the BQ/HQ system for aqueous, buffered and unbuffered situations. Their EC results agreed with Bailey's, although it is worth noticing that a Pt WE was used for most of the work instead of Au, and thus the EC behaviour for well buffered and unbuffered, low pH situation showed different behaviour. For the unbuffered system the number of electrons transferred (n_{app}) around

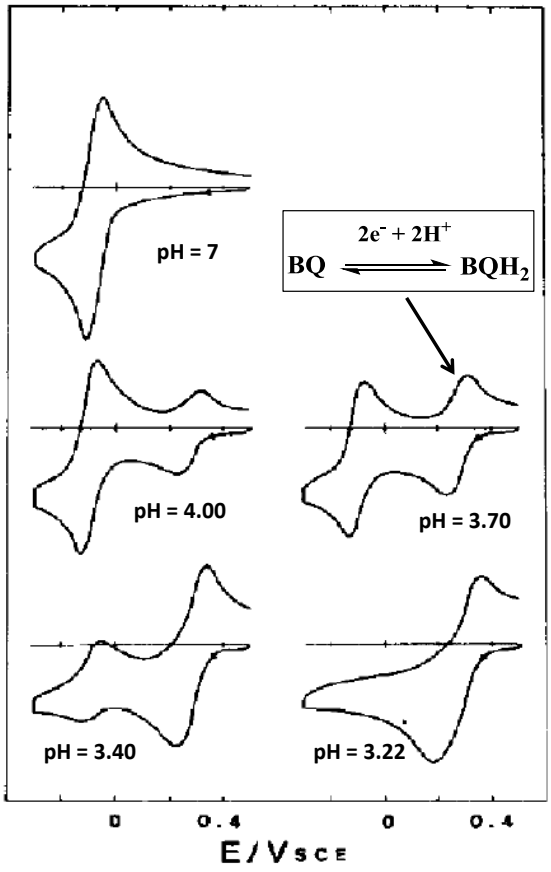

Figure 8.3. Reduction of BQ in unbuffered aqueous solutions. Decreasing pH distinguishes two different processes, one similar to buffered solutions and other requiring more negative potential (Modified from ref. [3])

neutral pH was determined to be 1.3 through chronoamperometric experiments, which led to the conclusion that, contrary to Bailey, only one electron transfer is involved in the reduction process. Combined with the observation that the half wave potential of the reduction process occurring at more negative potential (Figure 8.3) is essentially pH independent led to the conclusion that the reduction involves a fast electron transfer followed by a slow protonation process, indicating that the direct product of the electroreduction is the relatively stable anion radical ($BQ^{-\bullet}$).

UV-Vis and NIR spectroscopy revealed that for buffered solutions, irrespective of the pH value, only BQ and HQ species were present. This behaviour was consistent, whether BQ was reduced to HQ or HQ oxidized to BQ. In unbuffered solutions, at pH values above ca. 2.5, the data was interpreted to support a single electron reduction process, although the spectroscopic data did not reveal whether the major product was $BQ^{-\bullet}$ or the protonated $BQH^{\bullet}$ form. None the less, as pre protonation of the BQ species is not expected to occur at pH values above 2.5, the main reaction was concluded to be of the ECEC type giving a final product of BQH_2.

Tang *et. al.*[1] reported contradicting results to Shim *et. al.*, obtained through an EC-EPR and UV-Vis investigation of the unbuffered aqueous BQ system. First of all the number of transferred electrons in unbuffered solution at pH 7.73 was determined to be 2.09 by using a Pt rotating disc electrode and a Levich plot, in stark contrast to the value of 1.3 obtained by Shim *et. al.* at neutral pH. The half wave potential of the more negative reduction peak (as in Figure 8.3) was again observed to be independent of pH, leading to the conclusion that the reduction does not involve transfer of protons, but initially only two electrons yielding BQ^{2-} as the immediate product of the electroreduction.

The EC-EPR data recorded demonstrated a $BQ^{-\bullet}$ quintet spectrum with line intensities of 1:4:6:4:1 at pH 3.27, showing a hyperfine splitting constant of 2.39 Gauss in 0.5 M KCl,

close to the 2.368 Gauss reported earlier in alkaline ethanol solution.[6] The formation of a radical as a result of a two electron reduction was explained by comproportionation taking place after the initial two electron reduction. This observation was supported by EC-EPR, as the transient EPR SA was observed to increase after the potential was switched off at the WE.

None the less, as shown in Chapter 7 above for reduction of BQ in acetonitrile, an increase in the EPR SA for transient measurements can occur simply due to a change in the line width of the EPR spectrum even for a single electron reduction process. Similar behaviour was also observed for methyl viologen transients in Chapter 6. A true evidence of a comproportionationation reaction would be to record transients quantitatively, as was done in Chapter 6 relating the generated charge to the EPR SA. The transients recorded by Tang *et. al.* were also of low S:N, despite being recorded in extremely high [BQ], which means that any EPR signal will suffer severely from dimerization and spin-spin interactions. None the less, the reaction mechanism proposed still seems feasible (Scheme 8.2), although the EPR transient data does not strictly support it. The $BQ^{-\bullet}$ protonates in a rate determining step (rds), after which it decomposes to final products.

Shim *et. al.*[7] published an EPR investigation of their own a year after Tang *et. al.* The work performed did not assign the 2 electron reduction stoichiometry suggested by Tang *et.al.*,

$$BQ + 2e^- \rightleftharpoons BQ^{2-} \quad (1)$$

$$BQ + BQ^{2-} \rightleftharpoons 2\,BQ^{-\bullet} \quad (2)$$

$$BQ^{-\bullet} + H^+ \xrightarrow{(rds)} BQH^{\bullet} \quad (3)$$

$$BQH^{\bullet} \xrightarrow{(fast)} product \quad (4)$$

Scheme 8.2. Reduction mechanism for BQ in aqueous unbuffered solution at netral pH. The radical anion observed via EPR results from comproportionation of the dianion generated initially at the electrode surface. (From ref. [1])

but focused on the characterisation of the EPR spectrum of the reduction product. It was observed that the EPR spectrum of $BQ^{-\bullet}$ with the characteristic 1:4:6:4:1 line intensity ratio changed to 1:3:4:3:1 at pH 3.0. At pH 3.1 the initial 1:4:6:4:1 ratio turned to 1:3:4:3:1 if the spectrum was recorded 90 seconds after switching off the potential. The changing intensity ratio was concluded to be a result of protonation of the $BQ^{-\bullet}$ to a radical species $BQH^{\bullet}$, and the following pH dependent reaction mechanisms were proposed:

$$BQ + 2e^- + 2H^+ \rightleftharpoons BQH_2 \qquad \text{at pH < 3.0}$$

$$BQ + e^- \rightleftharpoons BQ^{-\bullet} + H^+ \rightleftharpoons BQH^{\bullet} \qquad \text{at 3.0 < pH < 3.1}$$

$$BQ + e^- \rightleftharpoons BQ^{-\bullet} \qquad \text{at pH > 3.1}$$

Scheme 8.3. The pH dependent reduction mechanism according to Shim *et. al.* A single electron reduction at neutral pH is proposed. (From ref. [7])

As with their first paper, the conclusions drawn were that the reduction of BQ at pH values above 3.0 is a single electron process (Scheme 8.3). None the less it could be argued that the results reported did not directly address the mechanism, as the radical $BQ^{-\bullet}$ could still originate from the first two steps in Scheme 8.2 at pH > 3.0, after which the protonation follows depending on the pH of the bulk solution.

The decay of $BQ^{-\bullet}$ at pH 3.1 and above was suggested to be a 1st order process from transient EPR data, where the radical anion oxidizes back to BQ. This observation was further supported by UV-Vis spectroscopy, where the absorption assigned to the BQ species first diminished during an applied potential and then returned back to pre-potential step value after switching off the potential, and no absorption associated to BQH_2 was observed. The problems related to transient methods in estimating kinetic parameters were discussed in a previous chapter, and thus the rate constants obtained should be approached with caution.

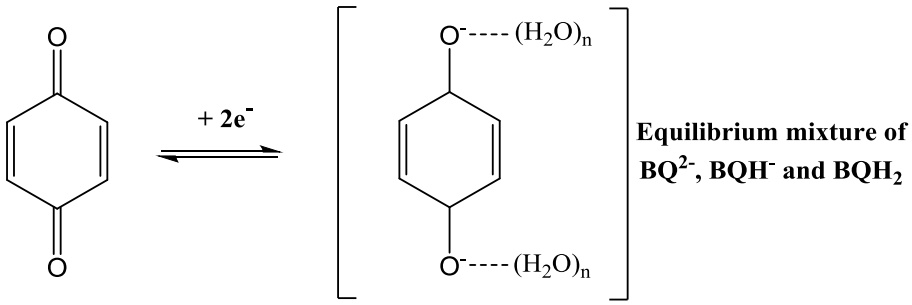

Scheme 8.4. Initial reduction mechanism in aqueous unbuffered solutions around neutral pH, where the two electron reduction product exists as a mixture of protonation states (From ref. [2])

Quang *et. al.*[2] published a comprehensive EC study for BQ and 2-anthraquinonesulfonate (AQS) in buffered and unbuffered aqueous media. AQS results were used to complement the BQ data, as it has been accepted that these quinones represent qualitatively similar results.[3] As with references above, it was concluded that the reduction of BQ in buffered solutions and when $[H^+]>[BQ]$ occurs via 2 e^-, 2 H^+ process to yield BQH_2. For the unbuffered solutions around neutral pH a two electron process was suggested as in Scheme 8.4.

The original two electron reduction product is stabilised by extensive hydrogen bonding, and the composition of the equilibrium mixture depends on the pH of the solution and quinone concentration. For example 1 mM BQ at pH 7, accounting for the pKa values given in Figure 8.1, BQ^{2-} exists as an equilibrium of protonation states, the principal species being protonated BQH^- (82.6 %) followed by BQ^{2-} (11.1 %) and BQH_2 (6.3 %). As the pH at the electrode surface can increase to 11 during electrolysis, initially a substantial BQ^{2-} can exist at the electrode surface before follow up reactions equilibrate the system. The mechanism agrees closely with Tang *et. al.* except for the formation of radical species.

Although the work clearly demonstrates that the redox chemistry changes fundamentally between unbuffered and buffered solutions keeping the pH the same, and that the hydrogen bonding is a missing link when explaining the redox chemistry in aqueous solutions, the work can be criticised on a few accounts. First of all the equilibrium mixture above does not include the $BQ^{-\bullet}$, although the spectroelectrochemistry papers discussed

above were referenced and comproportionation of BQ^{2-} stated as a source of the radical. Also, as stated in ref. 7, Shim *et. al.* observed $BQ^{-\bullet}$ to decay back to neutral BQ in unbuffered aqueous solution above pH 3.1, and that protonated form of the radical does not exist around neutral pH making Quang's BQH^- existing as a radical species an unexpected candidate as a source of EPR signal.

Finally in 2011 Klod *et. al.*[8] published results from *in situ* EC-EPR and EC-NMR work, essentially confirming the formation of BQH_2 at pH = 1 for unbuffered sample solution, in agreement with previous work. Interestingly at pH 7 a single electron reduction, accompanied by a proton transfer was proposed, where the neutral radical disproportionates to give BQ and BQH_2:

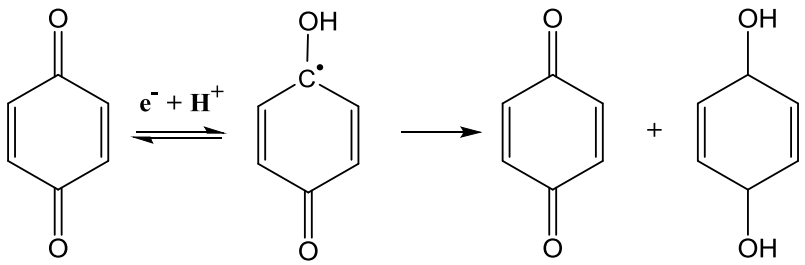

Scheme 8.5. BQ reduction mechanism in aqueous unbuffered solutions around neutral pH proposed via in situ EC-EPR and EC-NMR studies, where one electron and proton are transferred initially. (from ref. [8])

in stark contradiction with most of the observations above. Examination of the EPR data reported reveals that the experiments performed did not probe the actual mechanism of the reduction, but only detected the products of the electrode reaction. Also the NMR data was recorded over a time period of several hours, more likely revealing the products of the electrode reaction and not probing the actual mechanism of the electrode reaction.

8.2. Aims

As evident from the references above, the reduction mechanism is not fully understood or agreed upon for aqueous unbuffered solutions around neutral pH. Either one or two electrons are involved, and a radical species is clearly involved as evident from the EPR data. It should be noted that the results between different groups match at least qualitatively, and it is the interpretation that is not agreed upon.

If the process is initially a two electron transfer, then it is most likely that the radical species originates from a comproportionation reaction $[BQ^{2-}] + [BQ] \rightarrow 2\ [BQ^{-\bullet}]$. If this is the case the EPR signal of the $BQ^{-\bullet}$ should demonstrate a $[BQ]^2$ dependency, assuming that the relationship between [BQ] and $[BQ^{2-}]$ is linear, which can be confirmed or rejected by studying the EPR signal intensity as a function of [BQ]. This procedure would map the mechanism of radical formation directly, rather than simply record the spectrum of the resulting $BQ^{-\bullet}$.

It will also be of interest to apply quantitative EPR to this system to estimate the radical generation efficiency and to determine the fraction of the radical $BQ^{-\bullet}$ species out of the total charge generated to determine complementary data to the equilibrium mixture postulated by Guang *et. al.* Applying this procedure across a range of [BQ] and pH values should produce further insights to the electrochemistry of quinone species in aqueous unbuffered solutions.

8.3. Experimental

8.3.1. Materials

Materials used: 1,4-Benzoquinone (Fluka, certified purity 99.99 %), potassium chloride (BioXtra ≥99.0 %), potassium nitrate (ReagentPlus®, ≥99.0 %), HCl (30-35%, *Trace*SELECT® Ultra), HNO_3 (70%, ≥99.999% trace metals basis), KOH (*Trace*SELECT®) and 4-hydroxy-2,2,6,6-tetramethylpiperidin-1-oxyl (TEMPOL; Fluka, ≥98 %) were purchased from Sigma-Aldrich. All solutions were prepared in Milli-Q water (Millipore Corp.) (resistivity 18.2 MΩ cm, 25°C). All chemicals were used as received.

The WE were 50 µm diameter Pt micro-wires coated with a 7.5 µm layer of polyester (Goodfellow, ±10 % tolerance in conductor diameter) and chloridized Ag wire (125 µm in diameter) served as the RE. A coiled 250 µm diameter Pt wire acted as a CE.

8.3.2. Methods

The EC-EPR setup, including the electrode preparation has been described in Chapters 5 and 6 and the quantitative method in Chapter 7. The sample tube inner diameter throughout the experiments was 0.8 mm. The setup utilised allows the study of samples *in situ* within an inert atmosphere, making sure that the samples remained oxygen free. All of the EC and EC-EPR experiments were performed in Milli-Q water using 0.4 M KCl or KNO_3 as supporting electrolyte vs Ag|AgCl. pH values of samples were adjusted to pH 6.7 unless otherwise stated by adding small amounts (< 20 uL) of KOH, HCl or HNO_3 to 10 mL bulk solution containing a desired concentration of BQ.

Saturation curves for $BQ^{-\bullet}$ and TEMPOL were constructed in aqueous samples containing 0.4 M KCl. For $BQ^{-\bullet}$ the saturation was measured for the centre line, as it has been

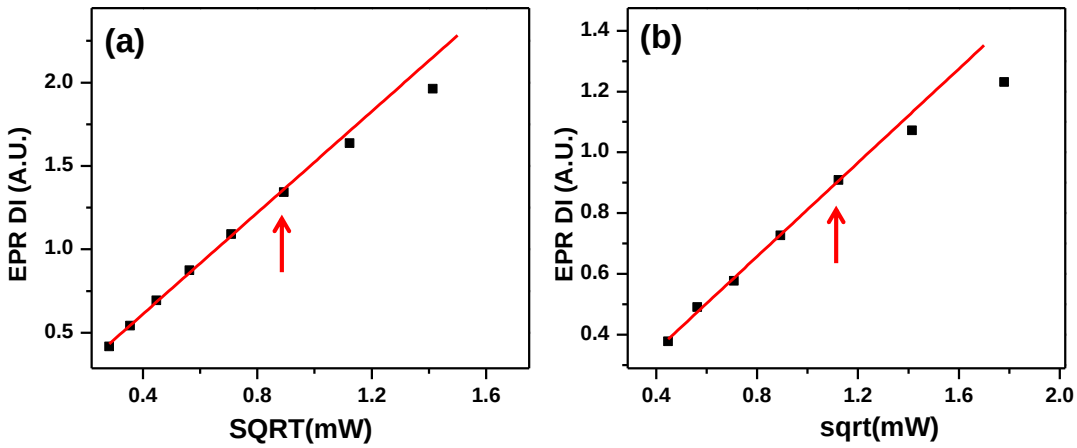

Figure 8.4. (a) Saturation curve for 100 µM TEMPOL, saturation observed to occur beyond power of 0.80 mW. (b) Saturation curve for 1.2 mM BQ, saturation observed beyond power of 1.26 mW. Spectrum recorded 10 seconds after 10 sec potential step to -0.3 V. Both (a) and (b) in aqueous solution with 0.4 M KCl. 0.50 mW was used for quantification and characterisation of BQ reduction products.

observed to be the most easily saturated.[9] Quantification was performed by double integrating the EPR spectra of $BQ^{-\bullet}$ and comparing to a calibration graph of TEMPOL.

An Arduino Uno microcontroller board was used to trigger the syringe pump, potentiostat and EPR spectrometer externally. The setup allowed the automation of the experimental procedures used below, and thus all of the data points reported represent an average value of five individual measurements, where fresh solution was infused to the cell between each repetition.

8.4. Results

8.4.1. Saturation study

Saturation curves for 100 µM TEMPOL and $BQ^{-\bullet}$ are shown in Figure 8.4, and the saturation was observed to occur at powers beyond 0.80 and 1.26 mW, respectively. Thus 0.5 mW power was used throughout the experiments. To obtain the saturation curve for $BQ^{-\bullet}$, a 10 second potential step at -0.3 V was applied to the WE in 1.2 mM BQ, and the EPR scan was

initiated 10 seconds after switching off the potential. Fresh solution was infused to the cell between measurements moving from one MW power to another.

8.4.2. BQ electrochemistry

CVs were recorded for 0.9 mM BQ solutions across varying pH values. As discussed in Section 8.1, at pH values approaching the bulk concentration of BQ, a second current peak at more positive potential has been observed, and this is confirmed in Figure 8.5a. At pH

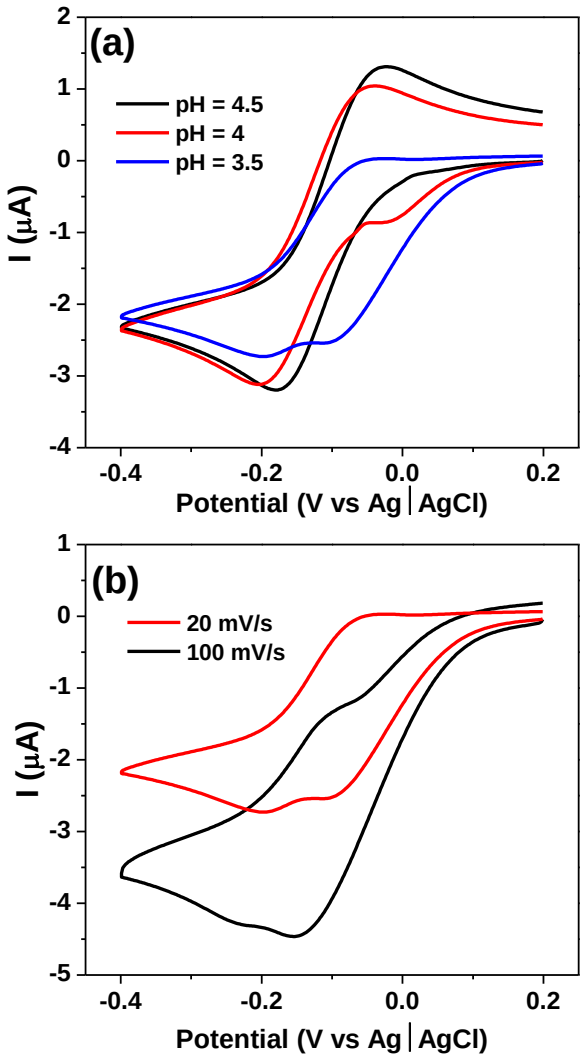

Figure 8.5. pH dependency of the reduction mechanism of BQ. (a) The appearance of a second reduction peak at more positive potential as pH is lowered. (b) The difference in relative peak currents at slow (20 mV/s) and fast (100 mV/s) scan rates for the more positive and negative reduction peaks. 0.9 mM BQ in 0.4 M KCl.

4.5 only the peak at -0.180 V was observed although when compared to CV at pH 5 (not shown), a small deviation from the baseline at 0.04 V was already observed. When the pH was decreased to 4.0 and 3.5, the appearance and increase of a second peak at more positive potential was evident. Figure 8.5b shows the behaviour at pH 3.5 for 20 and 100 mV/s scan rates. When scanning faster the peak at more positive potential shows larger magnitude, whereas with a slow scan the second peak seems to dominate**.**

Qualitatively this behaviour can be explained by the fact that during a slow scan the depletion of protons occurs to a larger extent at the electrode surface, thus increasing the magnitude of the more –ve peak. During a fast scan the more –ve peak potential is reached before an extensive depletion of protons has time to occur, and thus the peak at more +ve potential dominates. It is worth noticing that although qualitatively the result is similar to that in Figure 8.3, the mass transport at 50 µm diameter wire electrode is different and a Pt WE was used instead of Au, and thus the two peaks overlap to a greater extent.

8.4.3. pH dependency of radical generation efficiency

The pH dependency of the radical formation efficiency at the Pt WE was investigated during electrolysis of 0.9 mM BQ solution, and the results are displayed in Figure 8.6. Black squares show the amount of BQ^- expected to be generated, if every BQ molecule accepted one electron and the process was 100 % efficient, averaging 142 µM across the pH range investigated. If 2 electron reduction mechanism was assumed, the species generated at the electrode initially would be BQ^{2-} and the concentration ca. 70 µM.

The $BQ^{-\bullet}$ generation efficiency remains essentially the same from pH of 6.7 to 5.0, averaging 33 µM (black horizontal line). The y-error bars represent 1 standard deviation, where a calibration graph of TEMPOL was used to quantify the radical concentration, as

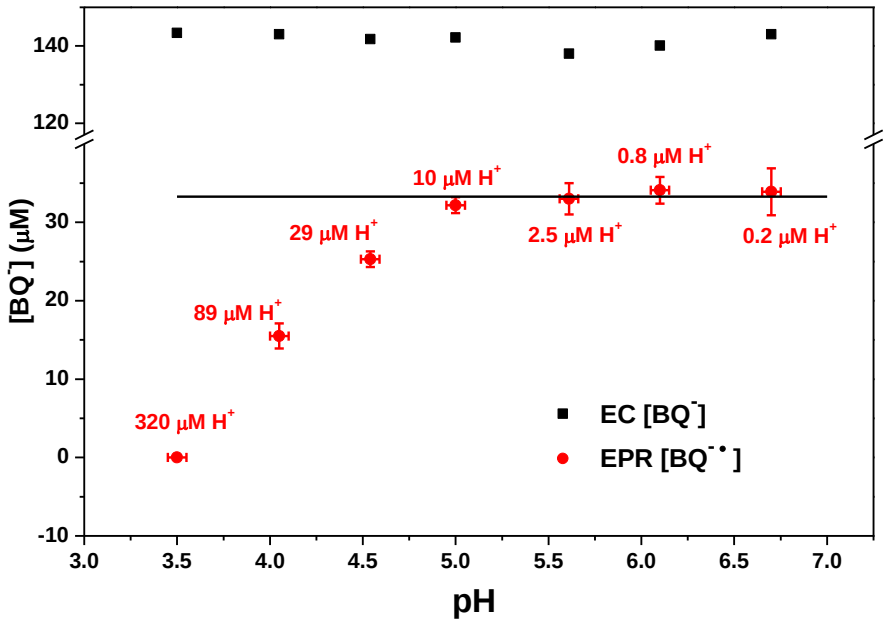

Figure 8.6. The pH dependency of radical generation efficiency in 0.9 mM BQ solution. Black squares represent the expected [BQ^-] assuming 100 % efficient one electron reduction process. 0.9 mM BQ in 0.4 M KCl.

explained in Chapter 7. The values associated to each EPR data point present [H^+] at that pH. The x-error bars have been included, as the bulk pH of the sample solution can be recorded before and after the EC-EPR experiments, and a typical pH drift of ±0.05 pH units has been observed in before and after measurements.

It is clear from the data that when decreasing the pH, as the [H^+] (29 μM) approaches [$BQ^{-\bullet}$] (33 μM) the generation efficiency drops noticeably, and at an order of magnitude excess of H^+ (pH = 3.5) the quantification of $BQ^{-\bullet}$ was not possible anymore. This does not mean that no radical was generated, as recording the EPR spectrum while applying a potential continuously did result in a faint signal. Only the quantification of the species was impossible due to the low concentrations of $BQ^{-\bullet}$ generated.

From Figure 8.6 it can be suggested that the drop in pH will not affect the charge generated (black squares), but the increasing magnitude of the more positive reduction wave in Figure 8.5 clearly shows that this process does not produce radical species.

8.4.4. Radical generation efficiency across [BQ]

After determining the pH dependence of the radical generation efficiency, a study across a concentration range was performed to investigate if the $[BQ]^2$ relation holds, as would be expected for a two electron reduction process generating radical species as a result of a comproportionation process. pH 6.7 was chosen for the study, as any small variations in pH will not interfere with the radical generation as discussed above.

Figure 8.7a shows $[BQ^{-\bullet}]$ against [BQ] aqueous solution at pH = 6.7, when 10 sec potential steps were applied to the WE, and the EPR spectrum recorded immediately after the potential switched off. Each data point is an average of 5 repetitions, where fresh solution was infused to the cell between potential steps. When fitted to linear and quadratic components, a strong quadratic relationship between [BQ] and $[BQ^{-\bullet}]$ was observed, although considerable linear component is also evident:

$$y = a[BQ] + b[BQ]^2 , \qquad (8.1)$$

where a = 12.7 ±3.7 and b = 26 ±2.4. This result strongly supports the notion of a two electron reduction mechanism, where a fast protonation reaction of BQ^{2-} to BQH^- is responsible for the linear component of the relationship and radical is generated via $[BQ^{2-}]$ + [BQ] → 2 $[BQ^{-\bullet}]$.

When compared to the expected $[BQ^-]$ based on the charge generated (Figure 8.7b, black squares), it is obvious that the comproportionation is far from 100 % and thus the $BQ^{-\bullet}$ is not a major product of the electrode reaction. The BQ^- concentration in the Figure 8.7 b apply to both electrode mechanisms, either direct one electron reduction or two electron reduction, where the BQ^{2-} comproportionates to BQ^- with 100 % efficiency.

Figure 8.7c shows the radical generation efficiency vs [BQ], where the concentration of [$BQ^{-\bullet}$] determined via EPR has been divided by the [BQ^{-}] determined via charge generated at the WE. The Figure shows that the radical generation efficiency increases with increasing [BQ], which can be explained by the fact that at higher [BQ] the pH at the electrode surface increases as more protons are consumed during the reduction of BQ. The depletion of

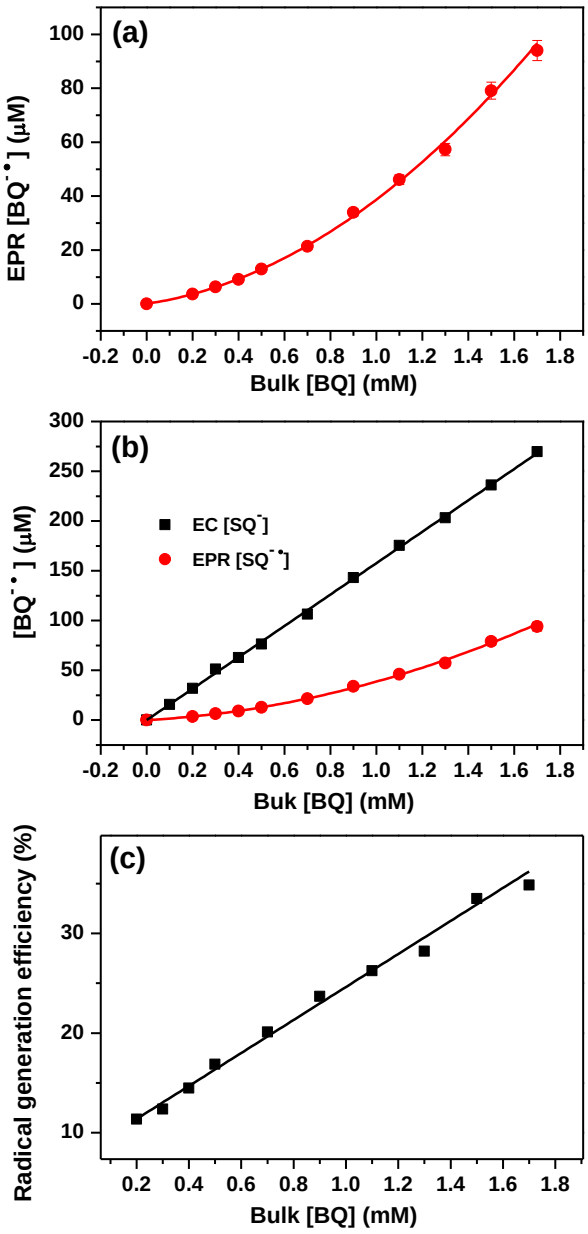

Figure 8.7. (a) [$BQ^{-\bullet}$] generated vs bulk [BQ] (mM) showing a quadratic relationship with a large linear component. (b) Comparison of the amount of radical generated (red circles) vs. that expected from EC data (black squares) for 100 % efficient process. (c) the radical generation efficiency, i.e. [$BQ^{-\bullet}$] detected by EPR divided by the [BQ^{-}] expected from EC results. 0.4 M KCl. All measurements at pH = 6.7

protons at the electrode surface then leaves more time for the BQ^{2-} to diffuse to the bulk solution and go through comproportionation. It is therefore suggested that at 1 mM [BQ], typical for EC and EC-EPR studies, the radical generation in aqueous unbuffered solutions at pH 6.7 in 0.4 M KCl is about 25 % efficient.

8.4.5. Decay kinetics

The lifetime of $BQ^{-\bullet}$ has been observed to follow first order decay kinetics in aqueous unbuffered solutions. Tang *et. al.* determined the half-life ($t_{1/2}$) through a UV-Vis flow through device and reported a value of 38.5 sec for solution of 5 mM BQ + 0.5 M KCl at pH 6.75.[1] Shim *et. al.* in their EPR studies recorded the mean lifetime across pH values for a solution of 1 mM BQ + 0.1 M KCl. The decay kinetics were again observed to be first order, 27.1 sec at pH 3.00, 37.5 sec for pH 3.05 and 59.2 sec at pH 4.00.[7] Furthermore, through UV-Vis Shim *et. al.* observed that the decay of $BQ^{-\bullet}$ was to BQ, as the absorption band at 245 nm returned to its original value after switching off the potential. No rate constant for this process was reported, but from the graph it seems that the original concentration is attained within 10 seconds at pH 3.1.[7]

When the kinetic measurements were performed it was observed that the decay, although showing 1st order characteristics, had a sizeable offset related to it. This is demonstrated in Figure 8.8a for 0.7 mM BQ solution, where the decay of the $BQ^{-\bullet}$ centre line DI is plotted against time and fitted with 1st order exponential decay. The red lines represent 95 % prediction bands obtained through regression analysis. The signal intensity drops only by ca. 25 % between 0 and 60 seconds, indicating that there is a second factor at play and the behaviour of $BQ^{-\bullet}$ decay cannot be explained by 1st order decay alone. The half-life ($t_{1/2}$) predicted from the exponential fit was 15.4 seconds, with an offset of 7.2. When ln(DI) was

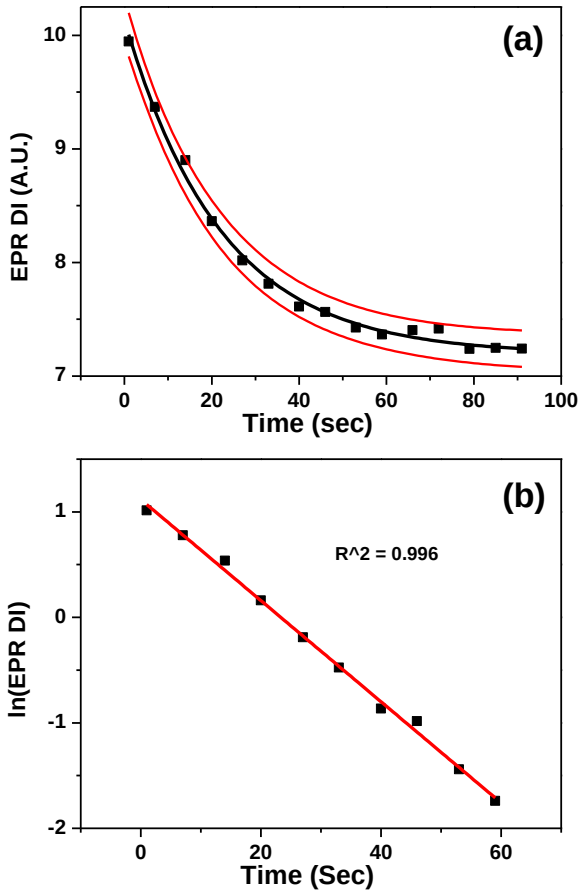

Figure 8.8. (a) Decay behaviour of 0.7 mM BQ solution fitted with first order exponential decay, where the red lines show 95 % prediction bands through regression analysis. (b) ln(EPR DI) from (a) vs time confirming a linear dependency with –ve slope, confirming 1st order decay process with half-life of 14.5 seconds. 0.4 M KCl.

plotted against time after subtracting the offset (Figure 8.8b), a straight line was obtained with gradient of -0.0479 s^{-1}, suggesting a $t_{1/2}$ of 14.5 seconds.

The offset was evident in all of the measurements across the concentration range studied, and increased roughly proportionally to the radical generation efficiency. This is shown in Figure 8.9, where the offset is plotted against [BQ] and compared to the radical generation efficiency, normalised to BQ concentration of 0.7 mM. The offset and [$BQ^{-\bullet}$] increase proportionally with an increase in [BQ]. This cannot be explained by a second order process, as in this case the increasing amount of radical species at times around 80 seconds would lead to the offset decreasing relative to the radical generation efficiency.

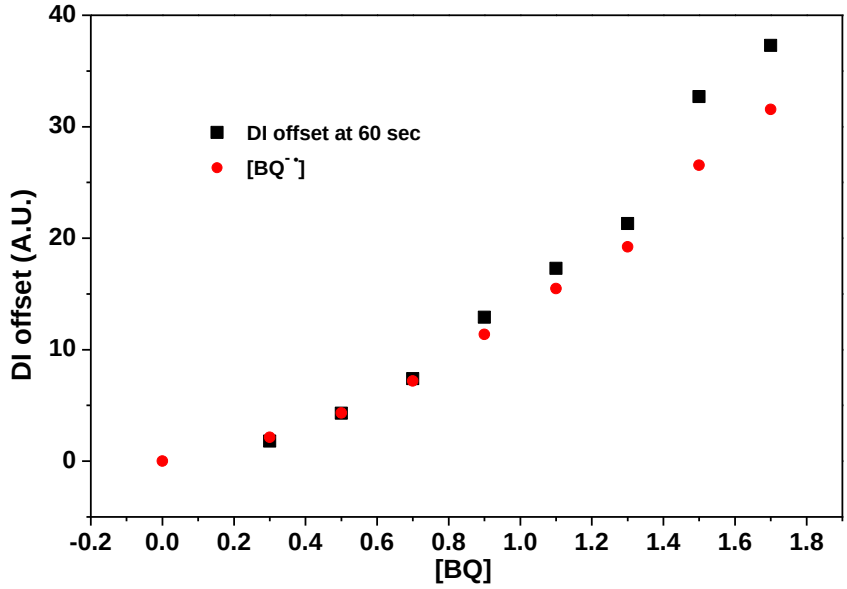

Figure 8.9. The offset evident in 1st order decay for $SQ^{-\bullet}$ relative to the $[BQ^{-\bullet}]$ vs [BQ] (mM) showing that the two quantities are closely related. 0.4 M KCl.

The decay of $BQ^{-\bullet}$ was not due to residual O_2 present in the sample, as was suggested in Chapter 7 in acetonitrile. This was confirmed by averaging 10 independent transients at 0.1 mM BQ, where the WE was stepped to -0.4 V for 10 seconds, as shown in Figure 8.10. The $[BQ^{-\bullet}]$ was estimated to be ca. 2 µM from Figure 8.7a, and thus any residual O_2, if capable

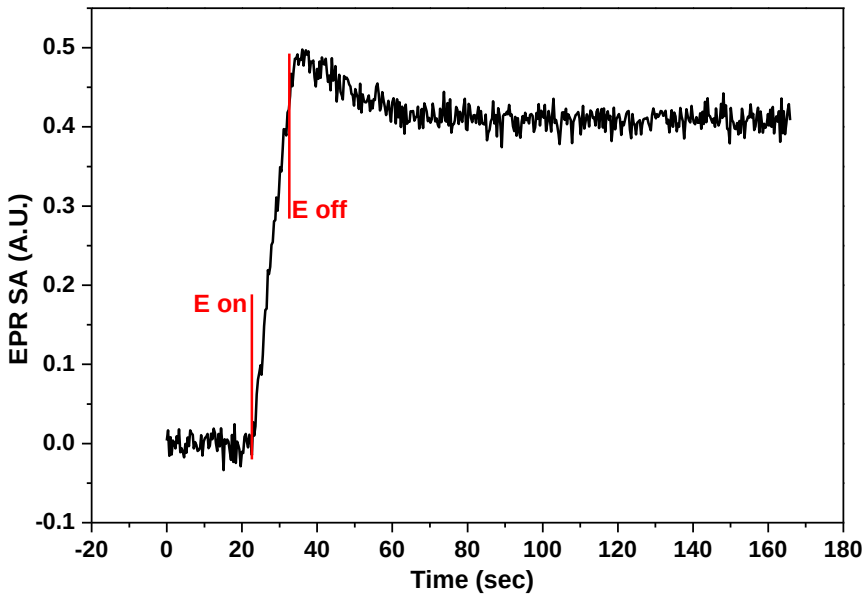

Figure 8.10. An average of 10 transient measurements at 0.1 mM BQ solution in 0.4 M KCl, pH 7. Estimated $BQ^{-\bullet}$ was 2 µM.

of re-oxidising $BQ^{-\bullet}$ back to BQ would affect the signal recorded. Instead of diminishing the EPR signal, the transient remains essentially stable for two minutes after switching off the potential, showing that $BQ^{-\bullet}$ is in fact stable around neutral pH even in minute concentrations.

The results of $t_{1/2}$ against concentration range studied are shown in Figure 8.11a at pH 6.7. The results were obtained by recording the entire EPR spectrum of $BQ^{-\bullet}$ consecutively over time after switching off the potential and following the DI of the centre line. This was necessary for 0.3 and 0.5 mM BQ samples, as the fast decay and inherently low $[BQ^{-\bullet}]$ prevented the reliable integration of the entire spectrum. Each data point represents an

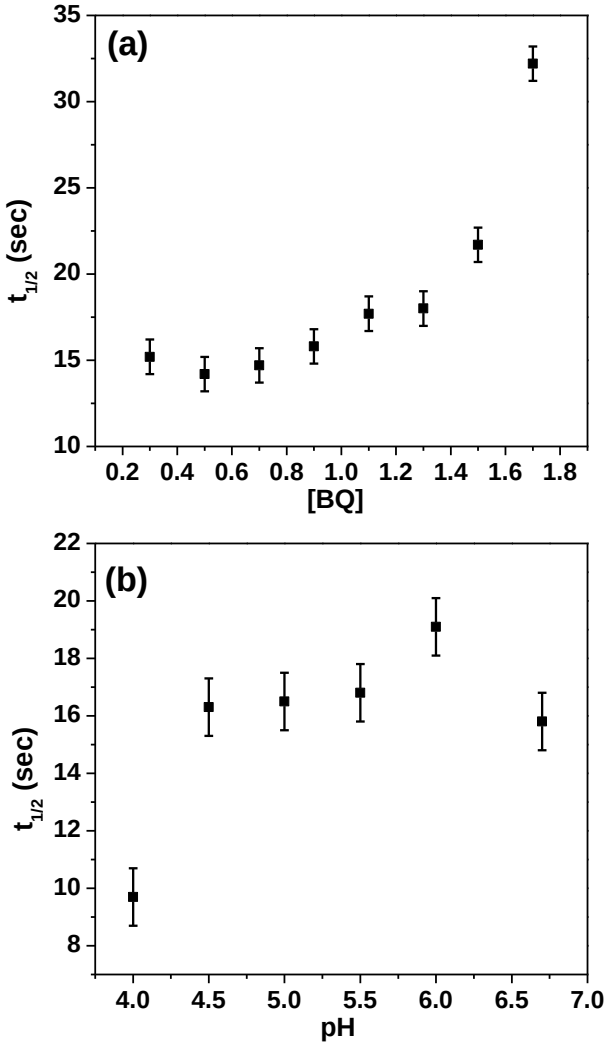

Figure 8.11. (a) $t_{1/2}$ vs [BQ] showing the gradually increasing half-life as the bulk concentration and thus $[BQ^{-\bullet}]$ increases. (b) $t_{1/2}$ vs pH of bulk solution, 0.9 mM BQ. Both (a) and (b) in 0.4 M KCl.

average of 5 repetitions. The values were obtained by plotting ln(EPR DI) vs time to determine the rate constant and then converting it to $t_{1/2}$.

At low [BQ] the decay showed faster characteristics than at higher [BQ], averaging $t_{1/2}$ = 15.0 seconds between 0.3 and 0.9 mM BQ, increased then to ca. 22 seconds by the time a bulk concentration of 1.5 mM was reached and then jumped to 32 seconds at [BQ] = 1.7 mM. It is worth noticing that this increase in $t_{1/2}$ explains the small deviation between DI offset and normalised $BQ^{-\bullet}$ generation efficiency evident in Figure 8.9, as the slower decay increases the amount of offset relative to [$BQ^{-\bullet}$] generated.

The $t_{1/2}$ increases significantly moving from 1.5 mM BQ to 1.7 mM BQ, which could indicate for example formation of monomer-dimer equilibrium, where the presence of dimer affects the decay rate due to less available $BQ^{-\bullet}$ present in the solution. This notion is supported for example by the observed radical generation efficiency, which was only ca. 1 % larger for 1.7 mM than for 1.5 mM solution (Figure 8.7c).

Figure 8.11b shows the $t_{1/2}$ as a function of pH for 0.9 mM BQ solution. Qualitatively the behaviour follows that of radical generation shown in Figure 8.6, dropping significantly at pH below 4.5. Interestingly a solution of pH 4.5 has ca. 30 µM H^+ present, which is also the [$BQ^{-\bullet}$] for 0.9 mM solution, as evident from Figure 8.6 and Figure 8.7a. Therefore both the $t_{1/2}$ and [$BQ^{-\bullet}$] are affected below pH values where the H^+ concentration equals and exceeds the concentration of radical species.

pH 4 where the drop in $t_{1/2}$ is observed is also just below the pKa value for $BQ^{-\bullet}$ (Figure 8.1), which further supports the protonation of the radical species being the source for diminished $t_{1/2}$. None the less, although a clear pH dependency is evident, a simple protonation would yield a neutral $BQH^{\bullet}$ which would still be detectable with EPR. If the accelerated decay of $BQ^{-\bullet}$ was a radical reaction due to an abstraction of proton from water

for example, this observation could suggest the presence of hydroxyl radical in the samples, although a short lifetime of this species would not allow the direct visualisation of its presence. In this case the pH dependency would have to explained by a catalytic nature of H^+ in the radical reaction.

8.4.6. Comparison of results

Result reported here are at odds with those of *Shim et al.*, where the shortest $t_{1/2}$ was 27.1 sec for pH 3. It seems unlikely that the pH of an unbuffered BQ solution can be controlled accurately enough to distinguish between pH values of 3.00 and 3.05, as it is not possible to monitor pH of the bulk sample solution inside the EC-EPR cell. Also the group used transient measurements to estimate the radical lifetimes, which can be questioned as discussed in Chapter 7. Therefore it is possible that the results reported by *Shim et. al.* overestimate the $t_{1/2}$, which has been proven to occur if the line width of the EPR spectrum changes after switching of the potential.

The $t_{1/2}$ of 38.5 sec reported by *Tang et. al*. for 5 mM BQ solution through UV-Vis is plausible, although the study reported here did not reach such a high concentration. For 1.7 mM BQ solution the $t_{1/2}$ was measured to be 32.2 seconds, suggesting that 38.5 sec by Tang *et. al*. is possible, as the result were obtained in a flow through device where the forced convection dilutes the generated radical and therefore the behaviour does not have to be comparable to a stationary solution shown in Figure 8.11a.

Fukuzumi *et. al.*[10] have investigated the lifetime of $BQ^{-\bullet}$ in neutral aqueous solutions obtained through oxidation of hydroquinone with manganese dioxide. The results suggested that the first order decay for semiquinone radical is 9.5×10^{-5} s^{-1}, suggesting a half-life of ca 2 hours. This value has been questioned by other authors,[11] but in the light of

the results reported here it would seem possible that the offset observed represents a second process taking place inside the EC-EPR cell with very long $t_{1/2}$, and therefore on the time scale of EPR measurements looks like an offset in the fitted data.

8.4.7. Spin trapping in BQ solutions

The observed decrease in $t_{1/2}$ at pH = 4 (Figure 8.11b) and the contemplation about a possible radical mechanism being responsible for the increased decay rate suggested that spin trapping could be used to acquire more information of the processes occurring in the BQ system.

Nitrone spin trap DMPO up to 28 mM was added to the solutions of 0.9 mM BQ in 0.4 M KCl and the pH adjusted to 6.7. Potential steps up to 15 sec did not yield any detectable spin adducts present in the sample. When 5.5 mM DMPO was added to 0.9 mM BQ in 0.4 M KNO_3 as a supporting electrolyte (pH = 6.7), the spectrum in Figure 8.12 was recorded. The four EPR lines for the spin adduct are indicated by arrows, of which the third from the left is partially overlapped by the dominating $BQ^{-\bullet}$ signal.

The least squares fit determined for the three peaks resolvable indicate a 1:1.82:(1.82):1 peak-to-peak intensity ratio, and the apparent hyperfine constant separating the lines is 1.485 mT. This intensity ratio and hyperfine splitting has been attributed to hydroxile adduct DMPO-OH, where the a_N and a_H are 1.487 and 1.481 mT, respectively.[12] Other tabulated values for the aqueous DMPO-OH adduct typically range between 1.48 and 1.49 mT depending on the exact composition of the system under study.[13] Therefore the closely matching hyperfine couplings for the N and H nuclei introduce 1:2:2:1 intensity ratio, although due to low signal intensity and over modulation other oxygen centred radicals cannot be completely ruled out.[14] Interestingly no DMPO-OH adduct was observed either if

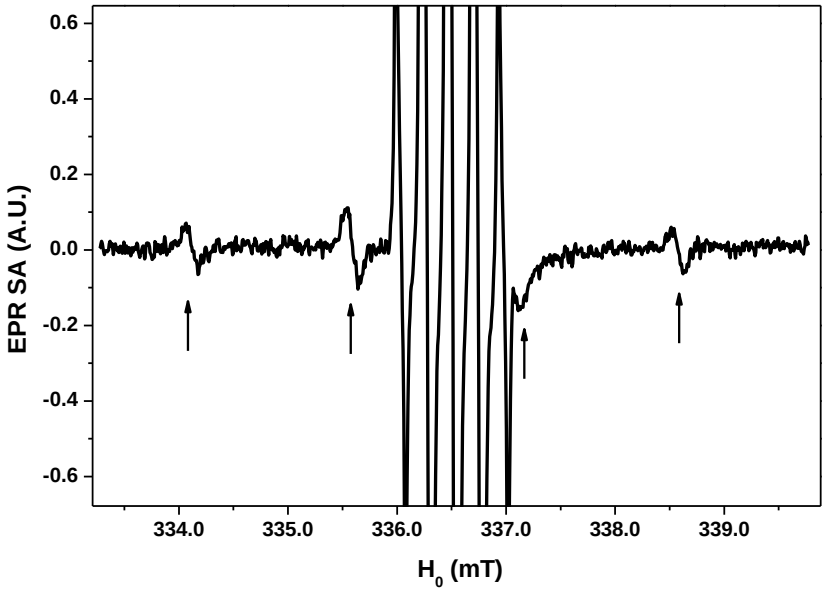

Figure 8.12. The spectrum of Spin adduct DMPO-OH in a solution of 0.9 mM BQ and 0.4 M KNO_3 acquired after 10 sec potential step to -0.4 V at pH 6.7.

0.05 M KCl was added to 0.35 M KNO_3 solution, indicating that the presence of KCl clearly changes the radical chemistry related to BQ.

The spectrum in Figure 8.12 is a result of averaging 10 scans after switching off the potential. The quantification of the adduct was performed based on the second peak from the left and scaling the DI obtained with the expected intensity ratio for the spectrum before comparing to the calibration graph. The resulting concentration was estimated to be ca. 2 μM, although due to the long acquisition time there is no way of estimating the effect of diffusion in the z-direction within the sample tube. Interestingly the adduct formation efficiency was not dependent of the length of the potential step, as 5, 10 and 15 second potential steps were employed and essentially the same result obtained every time. Also the adduct showed to be relatively stable, as consecutive spectral acquisitions 2 and 3 minutes after the initial one showed essentially the same concentration to be present in the sample.

Further work should be done by adjusting the pH of the sample to 4, where the rate of decay of $BQ^{-\bullet}$ was observed to increase (Figure 8.11b) using 0.4 M KNO_3 as a supporting

electrolyte. If the decay was indeed due to protonation via a radical mechanism, an increased amount of DMPO-OH adduct should be observed. Also further information could be obtained by conducting a spin trapping study across a [BQ].

8.5. Conclusions

The reduction of BQ in aqueous, unbuffered solutions show a complicated chemical behaviour. For the first time a method of quantitative EPR has been used to characterise the system across concentration and pH values under electrochemical excitation. It is evident that the reduction equilibrium cannot be characterised by principal species being protonated BQH^- (82.6 %) followed by BQ^{2-} (11.1 %) and BQH_2 (6.3 %) proposed by Quang *et. al.,*[2] as around 1 mM [BQ] the sample solution contains ca. 25% of the radical species $BQ^{-\bullet}$, as demonstrated by the results in Figure 8.7c.

None the less, a formation of BQ^{2-} as an initial intermediate of the electrode reaction is strongly supported by the quadratic relationship between [BQ] and $[BQ^{-\bullet}]$, where the radical species is formed via comproportionation. The main competing reaction is most likely the protonation of the dianion, as the radical generation efficiency increases with increasing [BQ], suggesting that the protonation reaction cannot keep up with the comproportionation as the pH is elevated during the reduction process for higher [BQ]. Protonation as a competing mechanism is also supported by the fact that the radical generation efficiency falls with the pH.

The spin trapping of the BQ system yields an interesting result, as the behaviour clearly changes when moving from KCl to KNO_3 as the supporting electrolyte. The difference is profound, as adding 1/20 KCl to the otherwise KNO_3 solution does not produce any adduct despite of the potential step length. It therefore seems that the BQ electrochemistry is

more versatile than suggested by the references in section 8.1, and thus reservations should be made as to whether the existing results in the literature can be generalised. Clearly there is more to benzoquinone chemistry than can be explained in the light of current knowledge.

References

1. Y. H. Tang, Y. R. Wu and Z. H. Wang, *J. Electrochem. Soc.*, 2001, **148**, E133-E138.
2. M. Quan, D. Sanchez, M. F. Wasylkiw and D. K. Smith, *J. Am. Chem. Soc.*, 2007, **129**, 12847-12856.
3. S. I. Bailey and I. M. Ritchie, *Electrochim. Acta*, 1985, **30**, 3-12.
4. E. Laviron, *J. Electroanal. Chem. Interfacial Electrochem.*, 1984, **164**, 213-227.
5. Y. B. Shim and S. M. Park, *J. Electroanal. Chem.*, 1997, **425**, 201-207.
6. J. E. Wertz and J. R. Bolton, *Electron Paramagnetic Resonance: Elemental Theory and Practical Applications*, 1972.
7. H. Park, M. S. Won, C. Cheong and Y. B. Shim, *Electroanal.*, 2002, **14**, 1501-1507.
8. S. Klod and L. Dunsch, *Magn. Reson. Chem.*, 2011, **49**, 725-729.
9. J. W. H. Schreurs, G. E. Blomgren and G. K. Fraenkel, *J. Chem. Phys.*, 1960, **32**, 1861-1869.
10. S.-i. Fukuzumi, Y. Ono and T. Keii, *Bull. Chem. Soc. Jpn*, 1973, **46**, 3353-3355.
11. C. H. Pyun and S. M. Park, *J. Electrochem. Soc.*, 1985, **132**, 2426-2428.
12. E. Finkelstein, G. M. Rosen and E. J. Rauckman, *Arch. Biochem. Biophys.*, 1980, **200**, 1-16.
13. G. R. Buettner, *Free Radic. Biol. Med.*, 1987, **3**, 259-303.
14. A. G. Krainev, T. D. Williams and D. J. Bigelow, *J. Magn. Res. Ser. B*, 1996, **111**, 272-280.

Overall conclusions

An electrochemical EPR cell has been designed for *in situ* EC-EPR experiments. Through the use of a loop gap resonator it has been possible to miniaturize the electrochemical cell and thus avoid issues with potential control related to traditional flat cell geometries. The EC and EPR performance of the cell can be optimised for any solvent system by adjusting the ID of the sample tube, and if necessary the micro wire WE can be replaced with a mesh, where preliminary tests in quiescent solutions showed that 20 times larger currents can be generated. Combining the mesh electrode with a solution flow to avoid the depletion of the electroactive species could improve the radical generation efficiency by up to two orders of magnitude, making the study of very short lived species possible.

The EPR sensitivity is good enough for routine study of most radical species, as complicated multiline spectra such as that for $MV^{-\bullet}$ can be detected in sub micro molar concentrations. Also for the first time the EC-EPR setup has been fully characterised for quantitative work, and the results between quantitative EPR and EC agreed within 3 % across the three fold concentration range studied. The results also suggest that quantification can be performed for micro molar concentrations in the case of simple EPR spectra such as $SQ^{-\bullet}$ with a single 5 second scan. If utilizing transient measurements, it is imperative that the time dependency of the line width is checked after switching off the potential, as the EPR signal amplitude is extremely sensitive towards the EPR line width.

The possibility of signal averaging should be utilised whenever possible, as the syringe pump/potentiostat/EPR interface can be externally triggered for automated data acquisition. The averaging should be used either to increase S:N of short lived species, or to increase the confidence of the reported values, as statistical treatment of the data becomes possible. In the future it is essential that the deoxygenation process for organic solvents is further studied and that the best method of keeping samples oxygen free while performing EC-EPR is determined. The easiest way to

do this would be to use the acetonitrile/ $SQ^{-\bullet}$ system from chapter 7. Also, as the data acquisition can be automated, it is essential in the future to develop more efficient data analysis tools within the group to get the maximum benefit from the system.

Good luck.